TAILORING SURFACE FORCES TO CONTROL THE FRICTIONAL PROPERTIES OF GRAPHENE

A Dissertation

by

MEAGAN B. ELINSKI

Submitted to the Office of Graduate and Professional Studies of
Texas A&M University
in partial fulfillment of the requirements for the degree of

DOCTOR OF PHILOSOPHY

Chair of Committee,	James Batteas
Committee Members,	Sarbajit Banerjee
	Matthew Sheldon
	Hong Liang
Head of Department,	Simon North

August 2018

Major Subject: Chemistry

ABSTRACT

A pressing financial and environmental challenge is the impact of friction and wear on energy usage, economic costs, and greenhouse gas (GHG) emissions. Globally nearly ¼ of the world's total energy is consumed at moving contacts, with 20% of that total used to overcome frictional forces. To combat the negative effects of friction and wear, thus mitigating economic spending on energy losses and reducing GHG emissions, new lubrication schemes need to be developed. Effective lubrication solutions will need to be compatible with a host of sliding conditions, including a diverse range of surface chemistries and structural features. One highly adaptable material capable of meeting this challenge is graphene, a two-dimensional sheet of carbon atoms with excellent electronic, optical, and thermal properties. Graphene additionally exhibits exceptional friction reducing and wear-resistant properties, although it is difficult to implement as a practical lubricant because its mechanical behavior strongly depends on its interactions with the top and bottom contacts within an interface.

To effectively capitalize on the lubricating potential of graphene, a thorough investigation into the tribological responses of graphene in controlled sliding contacts is required. Towards this goal, this dissertation includes research into graphene that is in sliding contact with molecularly modified interfaces, dynamically oscillating on rough surfaces, and covalently immobilized to the supporting substrate. Adhesion and friction measurements on graphene with molecularly functionalized atomic force microscopy (AFM) tips demonstrated how both chemical functionality and shear strain can be used to

tune the tribological response of the graphene-molecule sliding interface. Dynamic measurements of graphene on rough surfaces were exploited to examine the relationship between energy dissipation and friction at different frequencies. Pinning graphene to the supporting surface further showed how the physical properties of graphene can be manipulated at interfaces. By understanding how tailored adhesion, modulated out-of-plane forces, and localized pinning concertedly impact the tribological performance of graphene, the development of targeted lubricant technologies can take advantage of graphene's sensitivity to different sliding conditions. Designer boundary lubrication schemes incorporating graphene can then play a central role in overcoming the challenges associated with energy losses at tribological contacts.

ACKNOWLEDGEMENTS

A huge thank you goes to my committee chair, Dr. Batteas, for his guidance in research and constant advocacy on my behalf for my professional development. I would also like to thank my committee members, Dr. Sheldon, Dr. Banerjee, and Dr. Liang for their positive support and encouragement throughout my time at Texas A&M.

I am also extremely grateful for the friendship, personal support, and healthy discussions of science from my past and current labmates. Especially: Jessica Spear, who mentored and trained me during my first few years in the Batteas group; Brad Ewers, Stephanie Skiles, and Carrie Carpenter who also helped encourage me in the beginning of my graduate career; Cody Chalker, who has been my lab buddy through every aspect of the graduate program; Alison Pawlicki, Zhuotong Liu, and Maelani Negrito, who were unceasingly supportive as my fellow "Batteam Sisters;" Abhishek Parija, Nate Hawthorne, Fanglue Wu, and Quentarius Moore for their friendship and support; and Benjamin Menard, Meridith Buzbee, Abby Starck, Morgan Grandon, and Thomas Reyes for being amazing mentees.

Finally, I cannot express enough thanks to my parents and family for their constant curiosity in my research, confidence in my efforts, and love.

CONTRIBUTORS AND FUNDING SOURCES

Contributors

This work was supervised by a dissertation committee consisting of Professors James Batteas and Sarbajit Banerjee, jointly appointed in the Departments of Chemistry and Materials Science and Engineering, Professor Matthew Sheldon of the Department of Chemistry, and Professor Hong Liang of the Department of Mechanical Engineering.

The included experimental data for Chapter I was provided by Jessica Spear (Figures 1.15, 1.16, 1.17, and Table 1.1) and Zhuotong Liu (Figures 1.19, 1.20, and Table 1.2) of the Department of Chemistry, and was subsequently published with their co-authorship in 2017. The thermal gravimetric analysis in Chapter III was conducted by Benjamin Menard of the Department of Chemistry and supporting adhesion measurements for Chapter III were conducted in part by Zhuotong Liu. Their contributions were also published with their co-authorship in 2017. In Chapter V, the fabrication of the patterned graphene/pore structures, contact mode imaging, and preliminary friction force measurements were kindly done by Maelani Negrito of the Department of Chemistry (Figures 5.2 and 5.4). She will largely continue this work in new and exciting directions as part of her own research efforts.

All other work conducted for the dissertation was completed by myself independently.

Funding Sources

Graduate study was supported by a Texas A&M Graduate Merit Fellowship (2013) from Texas A&M University and the U.S. Senator Phil Gramm Doctoral Fellowship (2017) from Texas A&M University. Additional financial support was provided by the National Science Foundation under grant CMMI-1436192 to JDB.

TABLE OF CONTENTS

Page

LIST OF FIGURES

Page

LIST OF TABLES

Page

CHAPTER I

INTRODUCTION AND LITERATURE REVIEW: 2D OR NOT 2D? THE IMPACT OF NANOSCALE ROUGHNESS AND SUBSTRATE INTERACTIONS ON THE TRIBOLOGICAL PROPERTIES OF GRAPHENE AND MOS_2[1]

1.1 2D or not 2D?

Over fifty years ago the Jost Report called attention to tribological impacts on the economy.[1] Today the need to minimize material damage, improve the efficiencies of processes incorporating moving component, and combat economic losses and greenhouse gas emissions remains universal.[2] A recent call for a modern-day Jost Report highlighted the substantial amount of energy lost to friction and wear.[3] For example, it is estimated that almost 11% of the energy used by the transportation, industrial, and utilities sectors can be saved by developments in tribology.[4] Further, with 66% of the energy in electricity generation lost to conversion inefficiencies, there is significant room for improvement in energy conservation.[5] As the field of tribology has advanced, it has evolved to target multi-length scale problems ranging from lubrication challenges in large-scale industrial sliding interfaces to understanding the atomic origins of friction and stick-slip behavior. Focusing on the nanoscale regime of tribology is an advantageous means of investigating and controlling friction and adhesion due to the prevalence of nanoscopic surface roughness across a variety of interfaces.[6] At contacting nanoscopic asperities the high pressures and

[1] Reprinted with permission for minor editing from Elinski, M. B.; Liu, Z.; Spear, J. C.; Batteas, J. D. *J. Phys. D: Appl. Phys.*, **2017**, *50*, 103003. Copyright 2017 IOP Publishing.

shear forces enhance the ill effects associated with two surfaces in sliding contact, such as wear.[7, 8] It is because of these pressures and forces that, for systems or environments where solid boundary lubricants are required, the interface is challenging to lubricate. Previous efforts to lubricate nanoscopically rough interfaces have included diamond-like carbon (DLC) coatings,[9] implementing self-assembled monolayers (SAMs) to modify chemical interactions,[10] ionic liquids,[11] particles,[12] and many other materials and coatings. A promising boundary lubricant would be both structurally compatible with nanoscopic surface roughness and able to withstand stresses at contacting nanoscopic asperities.

Two-dimensional (2D) materials, such as graphene and molybdenum disulfide (MoS_2), have the potential to meet the stringent demands for functioning as solid boundary lubricants. A single sheet of graphene (single-layer graphene, or 1LG) is atomically thin, consisting of a hexagonal arrangement of sp^2-hybridized carbon (Figure 1.1a).[13]

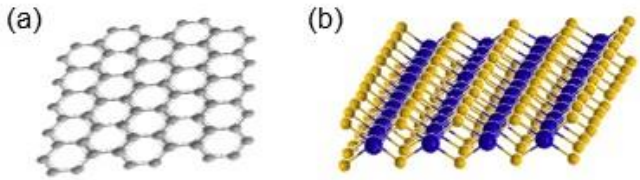

Figure 1. 1. (a) Schematic of the atomic structure of 1LG (gray = carbon). (b) Schematic of the atomic structure of 1LM (blue = Mo, orange = S).

Single-layer MoS_2 (1LM) is three atoms thick with one layer of molybdenum atoms sandwiched between two layers of sulfur atoms joined by covalent bonds (Figure 1.1b),[14] and with van der Waals forces holding multiple layers of either graphene or MoS_2 together.

Graphene has been shown to have high mechanical strength and macroscale wear durability,[15, 16] while both graphene and MoS_2 are capable of reducing friction forces.[17, 18] There is still a need to better predict and selectively tune the frictional responses of 2D materials, especially on realistic nanoscopically rough surfaces. The tribological responses of 1LG and 1LM are highly complex despite the simplifying aspect of consisting of only a single sheet. Their mechanical properties depend on the interaction strength of the 2D material with the supporting substrate, the morphology of the underlying substrate,[19, 20] chemical modification of the 2D material,[21-23] and the environment.[16, 24-28] The mechanisms governing the frictional response of the sliding interface can become even more complex when considering composite boundary lubricant systems.[24] Recent reviews have further discussed graphene and 2D materials as lubricants, but have not yet specifically concentrated on the complex relationship between nanoscale roughness and substrate interactions.[29-32]

In this introductory chapter the frictional properties of graphene and MoS_2 on nanoscopically rough surfaces using atomic force microscopy (AFM) are explored, as the AFM probe has been shown to mimic a single nanoscaled asperity contact.[33] First, the body of work surrounding AFM/FFM (friction force microscopy) studies of graphene on surfaces with roughness ranging from the atomic scale to the nanoscale (~30 nm RMS) will be examined. Specific consideration is given to both the morphology and the nanomechanical behavior of graphene on these surfaces and the influence of modulating substrate interactions on the resulting frictional properties.[34] Then, as a comparison, these studies are extended to that of MoS_2 on rough surfaces.

1.2 Factors Influencing the Frictional Response of Graphene

AFM/FMM studies of 2D materials offer a unique method to explore their nanotribological properties.[33, 35] Additional details of the basic principles for AFM/FMM, as well as other AFM methods (adhesion measurements, force modulation microscopy, and scattering-type scanning nearfield optical microscopy) are included in Chapter II. The AFM probe models single-asperity contacts, and based on the chosen experimental design the set-up allows for environmental control as well as manipulation of both the bottom contact (i.e. supporting substrate morphology and surface chemistry) and the top contact (i.e. AFM probe size and chemistry). In FFM measurements of graphene precise placement of the AFM probe allows for direct comparison of single-layer graphene (1LG), bilayer graphene (2LG), few layer graphene (FLG), and bulk graphite (similarly, 1LM, 2LM, FLM, and bulk MoS_2). For FFM measurements of graphene on surfaces with atomic scale roughness the sliding interface is generally between the AFM probe tip and top side of the graphene sheet. Here the measured frictional response has been found to largely depend on the mechanical out-of-plane deformation of the graphene sheet, seen as an increase in the friction force with decreasing number of graphene layers, with the highest friction being observed on single layers (Figure 1.2d).[36-39] The correlation between layer thickness and frictional response is shown in Figure 1.2, where the thinner layers in the AFM topography image (Figure 1.2a) correlate to higher friction forces (Figure 1.2b).

This work by Lee *et al*[39] suggests that the dependence of the frictional force on the number of layers is a universal property of 2D materials (graphene, MoS_2, niobium diselenide, and hexagonal boron nitride) and arises from the increased susceptibility of

thinner layers to deform out-of-plane in front of the sliding AFM probe.[39] This "puckering effect" (Figure 1.2c) increases the tip-graphene contact area, in turn increasing the observed friction force.

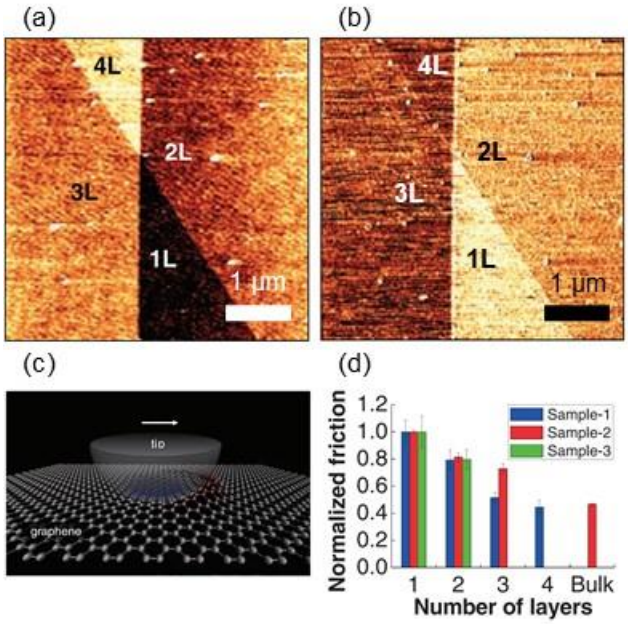

Figure 1. 2. (a) AFM topography image showing height contrast between different graphene layers labeled as 1-4 layers (L). (b) Corresponding FFM image to the topography image in (a), where the brighter contrast indicates higher friction force. (a) and (b) Show the correlation between layer thickness and friction force, where thinner layers have a higher friction force. This effect is shown as a bar plot in (d), with the raw friction signal normalized to single layer graphene for three samples. The proposed cause of the layer dependence is that thinner layers deform more easily out-of-plane, creating a "pucker" in front of the sliding AFM tip, as shown in (c). Adapted with permission from Lee *et al*.[39] Copyright 2010 by AAAS.

It also reflects the dynamic behavior of graphene, as the sheet bends in reaction to the sliding contact. More detailed investigations (discussed in the following paragraphs) of the out-of-plane deformation that dominates the measured frictional response of

graphene have elucidated that it depends strongly on the relative strength of the interactions between graphene and the bottom and top contacts.

Shortly after Lee *et al*[39] proposed the puckering effect as the mechanism behind the layer-dependent frictional response of graphene, Choi *et al*[40] reported the observation of frictional domains in 1LG. For a single layer of graphene supported on nominally flat SiO_2, no major topographical variations were observed, yet distinct regions of varying frictional forces were seen in the simultaneously collected friction force images. It was proposed that the domains arose from ripple distortions which led to anisotropic puckering of graphene, and that the ripple structure was ultimately a result of inhomogeneous interactions of graphene with the supporting SiO_2 substrate. This could be mitigated by increasing the applied load, such that the larger resulting contact area decreased the contribution of ripple deformations to the measure friction. More recently, Gallagher *et al*[41] proposed that the anisotropic frictional domains of 1LG instead arose from self-assembled environmental adsorbates. The direction of the resultant stripe-superlattice pattern could be switched based on the scan direction and applied load of the AFM probe, as shown in Figure 1.3a. Altering the self-assembled strip orientation changed the measured friction force. Figure 1.3b shows how different friction force contrasts were obtained on the regions of stripe orientations in the insets.

The influence of the supporting substrate was investigated by Cho *et al*.[19] Comparing graphene on SiO_2 vs on atomically smooth surfaces (hexagonal boron nitride, mica, and bulk-like graphene) demonstrated that the frictional response correlated to the graphene-substrate adhesion and substrate morphology. Here it was shown that the layer-

dependent response could be suppressed as the graphene-substrate interaction strength was increased, which occurred for graphene transferred to the atomically smooth surfaces where high contact intimacy was achieved (Figures 1.4a,b). For graphene folded from SiO_2 onto bulk-like graphene, a higher friction force was preserved as the "memory" of the corrugations induced from the initial transfer to SiO_2 remained, even on the atomically smooth bulk-like graphene (Figures 1.4c,d).

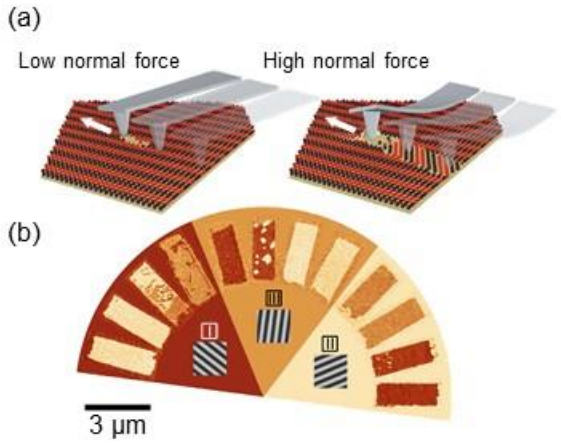

Figure 1. 3. (a) Schematic of how the stripe-superlattice of self-assembled adsorbates can be manipulated with the AFM probe. (b) Three friction regions with different orientations of stripe patterns, labeled in the insets as I-III. Within each section is various alterations of friction force based on changing the stripe direction. Adapted with permission from Gallagher *et al*.[41] Copyright 2016 by Macmillan Publishers Limited.

Further exploring the competition between graphene-substrate vs graphene-tip interactions, studies by Egberts *et al*[42] and Liu *et al*[43] addressed how build-up of the graphene pucker altered the mechanical responses. In the study by Egberts *et al*[42] the

frictional force of graphene on copper depended on whether or not contact was broken between the AFM probe and graphene during sliding.

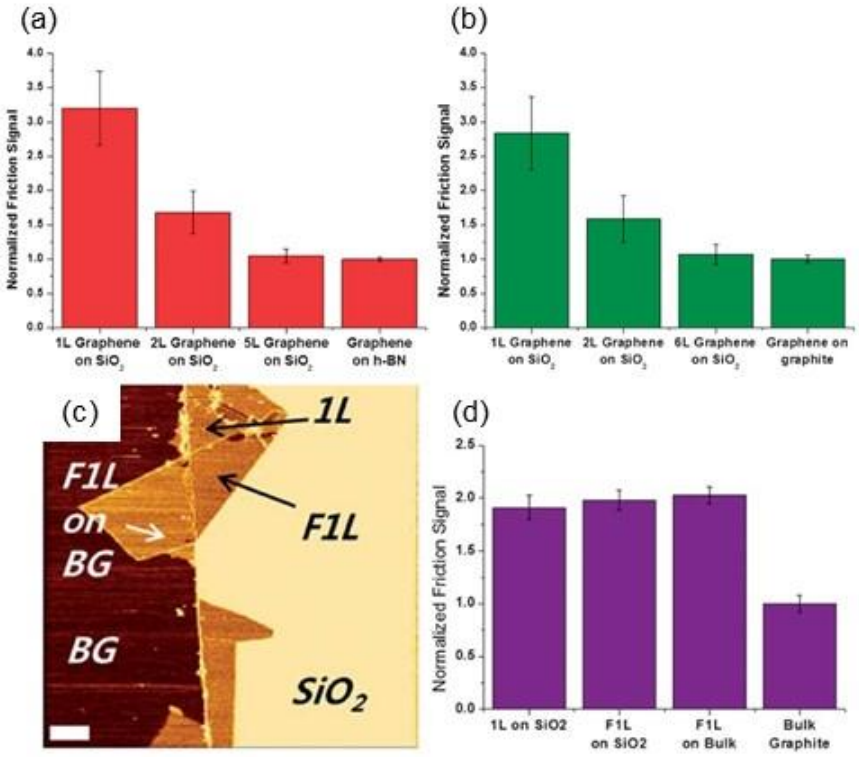

Figure 1. 4. The bar plots in (a) and (b) show the friction signals of different layer thicknesses of graphene on SiO_2 normalized to single layer graphene (1L) on hexagonal boron nitride (hBN) and 1L graphene on graphite, respectively. The data shows 1L graphene on the two atomically smooth surfaces (hBN and graphite) has an almost equal friction force to bulk-like graphene (5L on SiO_2), suggesting the puckering mechanism is suppressed when the 1L graphene is more strongly adhered to the atomically smooth surfaces. The FFM image (scale bar: 1 μm) in (c) shows 1L graphene folded (F) onto itself and onto bulk-like graphene (BG). In both (c) and the corresponding bar plot in (d), the high friction force of the 1L originally deposited on SiO_2 is retained as the "memory" of the SiO_2 surface morphology. Adapted with permission from Cho *et al.*[19] Copyright 2013 by RSC Publishing.

Large hysteresis was seen in friction vs load measurements when the probe/graphene contact remained intact throughout the measurement, seen in Figure 1.5a as a largely increased friction force for the unloading curve over the loading curve. This degree of hysteresis was not observed on the bare copper surface or on graphene when the probe/graphene contact was disrupted by scanning over the edge of the graphene flake (Figure 1.5b).

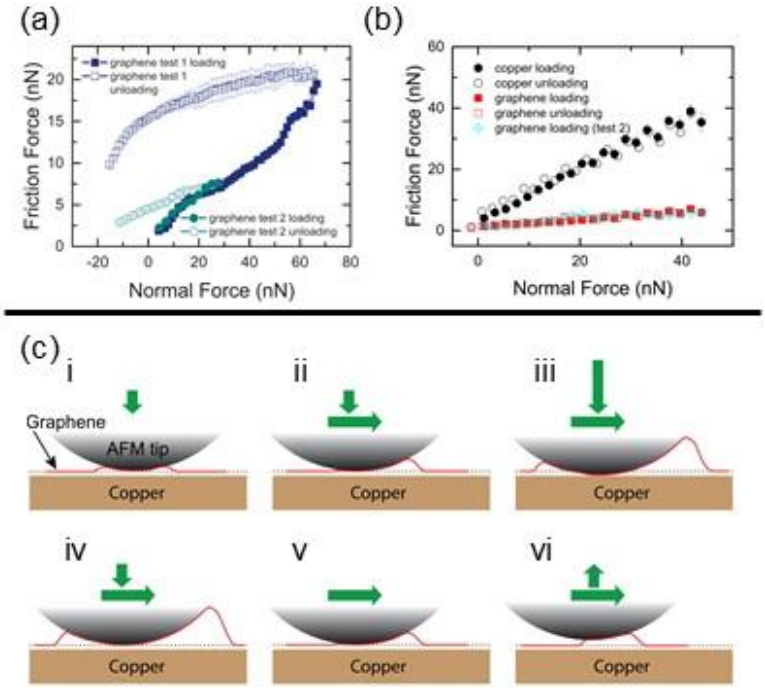

Figure 1. 5. The friction vs load plots in (a) and (b) show the loading and unloading cycles for graphene on copper and, additionally in (b), the exposed copper surface. In (a), extensive hysteresis is observed as the tip does not break contact with the graphene sheet at any point during the loading/unloading cycle. In (b), no hysteresis is observed for the exposed copper surface, or for graphene in the case where tip/graphene contact is broken by sliding over the edge of the graphene sheet. The series of schematics in (c) show the proposed mechanism for the increase in graphene puckering as the load is increased (i-iii), and the subsequent slower decrease in graphene puckering as the load is decreased (iv-vi). Adapted with permission from Egberts *et al*.[42] Copyright 2014 by ACS Publishing.

The proposed mechanism, shown sequentially in Figure 1.5c, centered around the idea that the size of the pucker first grew under increasing applied load (schemes i-iii in Figure 1.5c), then shrunk at a slower rate under decreasing applied load (schemes iv-vi in Figure 1.5c). The extensive puckering indicated that graphene-copper adhesive forces were relatively weak and affirmed that graphene-substrate interaction strengths substantially influence the frictional response of the top sliding contact.

In a similar argument, when the graphene-tip contact area was increased by build-up of the graphene pucker from initial sliding (pre-sliding) of the AFM probe, Liu *et al*[43] observed a 12-17% increase in the first pull-off force. Subsequent pull-off forces returned to the constant value measured when there was no pre-sliding of the AFM probe. The initial enhancement in pull-off force was not seen for direct pull-off force measurements, where the tip was retracted from the surface with no pre-sliding. This phenomenon was supported by finite element modeling (FEM) comparing direct pull-off measurements with pre-sliding pull-off measurements for graphene-tip interaction ratios of 1.2 vs 2.0. Only in the case of increased graphene-tip adhesion (interaction ratio of 2.0) was there an enhanced pull-off force observed with pre-sliding due to a larger pucker of the top layer of graphene.

Increased tip-graphene adhesion was also shown by Deng *et al*[44] to impact puckering of surface graphite layers. Under decreasing load, as the AFM tip was retracted while scanning, a negative coefficient of friction (COF) (Figure 1.6a) was measured when the adhesion between the AFM tip and surface was enhanced relative to the exfoliation energy between graphite layers. Shown schematically in Figure 1.6b, the topmost layers

of graphite conformed to the tip and remained attached during retraction. The local layer delamination caused the surface layer(s) to behave increasingly like 1LG as the applied load was decreased, which increased the graphene pucker around the AFM tip and resulted in a higher friction force for decreasing loads.

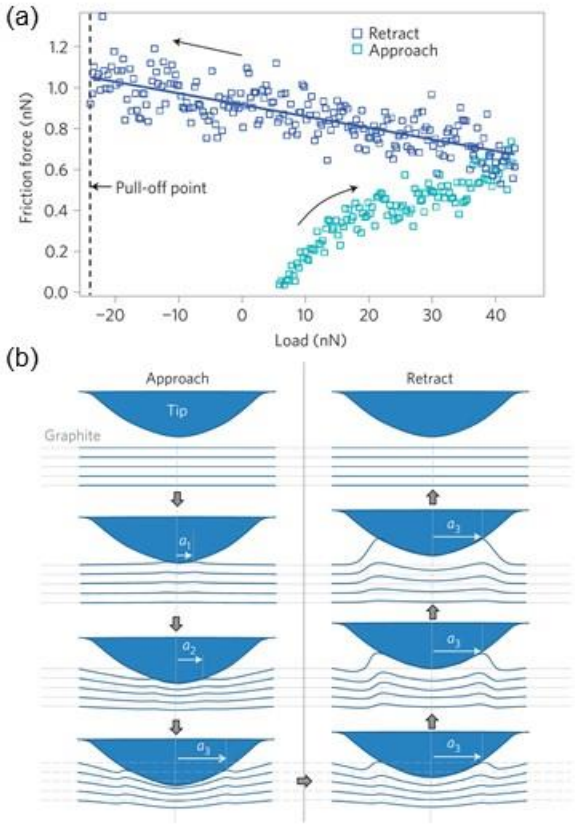

Figure 1. 6. (a) Friction vs load curve showing a negative coefficient of friction during tip retraction on graphite. (b) Schematic of local layer delamination during retraction of the AFM tip. Adapted with permission from Deng *et al.*[44] Copyright 2012 by Macmillan Publishers Limited.

It is helpful to compare the mechanisms of the frictional behavior of graphene observed by Egberts *et al*[42] (Figure 1.5) to that observed by Deng *et al*[44] (Figure 1.6). Both studies saw increased graphene puckering for decreasing load. In Figure 1.5 however, 1LG was delaminated from copper, while in Figure 1.6 the ratio of tip-graphene adhesion to the exfoliation energy of graphite was large enough to delaminate the top graphene layers. These differences were enough to shift the frictional response of graphene from a case of large hysteresis to one of a negative friction coefficient.

These studies emphasize how the competing interactions between an atomically thin 2D material and the supporting substrate vs the top nanoscale contact impact the material's nanotribological behavior. Other studies have compared graphene on SiO_2 with suspended graphene[45] and graphene on Ni(111)[46] to further investigate how graphene-tip adhesion can depend on subsurface interactions and to explore causes for differences in shear stress. In the work by Deng *et al*[45] SiO_2 supported graphene layers (1LG, 2LG, and FLG) were compared to suspended graphene layers. Analyzing the friction vs load response of supported graphene layers against bare SiO_2 (Figure 1.7a), the shear strength of the AFM probe on SiO_2 was 1-2 orders of magnitude greater than on the supported 1LG (1250 ± 200 MPa and 23.6 ± 2.3 MPa for bare SiO_2 and the supported 1LG, respectively). Additionally, the supported graphene layers and suspended graphene layers had dramatically different nanotribological properties, attributed to the higher flexibility of the suspended layers. In particular, for pull-off force measurements no layer-dependence was observed for the supported graphene, but for the suspended graphene the pull-off force increased as the number of layers increased. This trend was concluded to be a combined

result of graphene elasticity and the van der Waals forces between the tip and any subsurface material (additional graphene layers in the suspended region). As thicker layers have a higher stiffness, they exhibited a reduced downward curvature at pull-off as the AFM tip lifted the membrane, which allowed for more of the suspended graphene layers to interact more closely with the tip and increased the pull-off force.

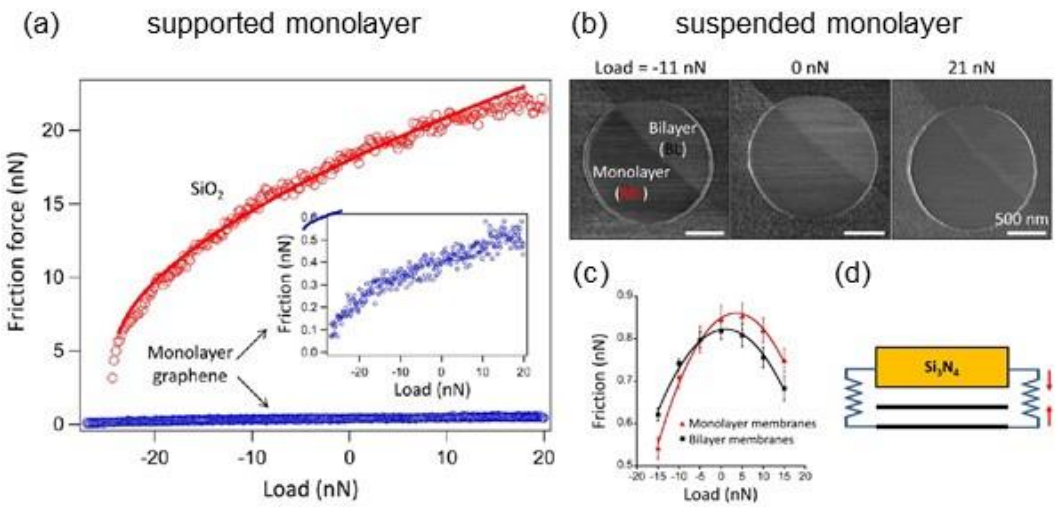

Figure 1. 7. Comparing supported vs suspended monolayer graphene, the friction vs load curves in (a) for bare SiO_2 and monolayer graphene supported on SiO_2 were fit with the DMT-JKR transition model to calculate the shear strength of each. The inset of (a) is a magnification of the monolayer graphene curve. The FFM images in (b) show the changes in friction contrast for suspended monolayer vs bilayer graphene under negative load, no load, and positive load. The friction vs load curves for the suspended graphene layers in (c) show the switch in layer dependence based on load, and emphasize the difference in nanomechanical behavior compared to supported graphene in (a). The schematic in (d) shows the compressive model proposed for attraction between the Si_3N_4 AFM tip and subsurface graphene layers. Adapted with permission from Deng *et al*.[45] Copyright 2013 by ACS Publishing.

Further, for thicker layers, additional attractive interactions between the tip and subsurface graphene layers permitted the tip to exert a greater force on the suspended graphene layers. An increased compressive contact (Figure 1.7d) corresponded to increased compression of the top graphene layer against the tip and enhanced the tip-sample adhesion. Frictional properties of the suspended graphene layers were similarly seen to depend on the deformation of graphene and tip-subsurface material van der Waals forces. This was manifested in the suspended graphene layers as a reversal in the typical layer-dependence of the friction force. At low or negative loads, there was an increase in friction force with added layer thickness, in contrast to the decrease in friction force with added layer thickness observed in supported graphene. This can be seen in the friction images of the suspended graphene layers comparing 1LG and 2LG in Figure 1.7b at low load, no load, and positive load. Figure 1.7c further displays how the layer dependence of the friction force switched under different load regimes. The authors argued that despite any rippling that could have occurred in the membranes (normally characteristic of the puckering effect and typical increase in friction force for thinner layers), without the supporting substrate the reduced contact pressure at low/negative loads was the dominating factor in the friction response. Then at high positive loads, where the layer dependence was reversed, the thinner membranes had larger deflections, thus greater conformation to the tip (increased tip-sample contact area) and subsurface layer contributions were decreased relative to the tip-membrane contact pressure.

It should be noted that, with respect to tip-subsurface interactions, separate work by Tsoi *et al*[47] found that a single layer of graphene completely screened the van der Waals

forces of the SiO_2 substrate (shown schematically in Figures 1.8a,b). Examining the snap-in region of force-distance curves (Figure 1.8c) revealed that the interaction between the tip and sample was weakest for 1LG on SiO_2 and increased with added layers. The interaction with bulk graphite (HOPG) was notably the strongest, with detected forces at a tip-sample separation of 15 nm, while 1LG on SiO_2 did not detect any forces until the tip had approached to within 7 nm of the surface.

The data shown in Figure 1.8c was fit using assumptions within a standard dielectric continuum model and adopted the Derjaguin approximation for a van der Waals interaction between a sphere and a half space (the sample surface).

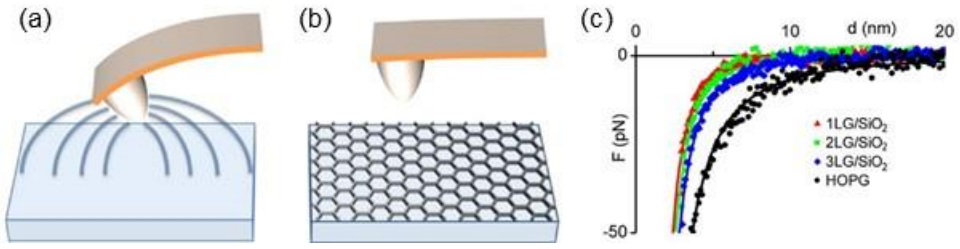

Figure 1. 8. The schematics in (a) and (b) show the van der Waals interaction between the AFM probe and SiO_2 surface in (a) and their effective screening by graphene in (b). The snap-in region of force-distance curves for 1-3 layer graphene and bulk graphite (HOPG) are shown in (c). An outward shift in the curves shows the interaction strength between the tip and surface increasing with increasing number of graphene layers, as tip-sample interactions are felt at longer distances from the surface. Adapted with permission from Tsoi *et al*.[47] Copyright 2014 by ACS Publishing.

From this, the Hamaker constants for each layer thickness were calculated, yielding a negligibly small value for the SiO_2 contribution. Based on this work, it is likely that the differences observed by Deng *et al*[45] between supported and suspended graphene are

dominated by the variations in stiffness of the different layers (and resulting changes in contact pressures), rather than attractive forces between the tip and subsurface material.

Alternative to comparing SiO_2 supported graphene with suspended graphene, Paolicelli *et al*[46] compared SiO_2 supported graphene with graphene on Ni(111) and demonstrated that graphene on SiO_2 had a shear strength four times larger than graphene on Ni(111). The reduction of shear strength for the graphene-Ni(111) system was reasoned to be a result of both decreased roughness (30% lower roughness than graphene on SiO_2) and the commensurate interface produced from graphene growing in registry with Ni(111). This prevented significant puckering of the graphene, leading to an overall more rigid surface under sliding contact. Further influence of the supporting substrate on the frictional response of graphene was more recently demonstrated by Tripathi *et al*[48] for FLG over polycrystalline Ni. The COF of FLG at interfacial grain boundaries was lower than on the grain regions, found to be due to accumulated carbon layers and increased roughness through texturing of carbon pillars/spikes.

The selected nanotribological studies of graphene discussed so far begin to detail how the supporting substrate and competing interactions between the bottom and top contacts play vital roles in the behavior of graphene as a solid lubricant. While they predominantly focused on nominally flat surfaces, it is clear that small changes in surface morphology can have dramatic impacts on the mechanical responses of graphene in sliding contact. This implies that studies focused on investigating 2D materials on nanoscopically rough surfaces are warranted to understand the interplay of interactions that govern the frictional behavior of 2D materials on more realistic interfaces. Understanding their

behavior will be critical for establishing means to develop tailored lubrication schemes based on 2D materials such as graphene. The following section is devoted to addressing some of the studies that have begun to explore graphene on rough interfaces.

1.3 Graphene and Substrate Morphology – A Rough World

To study the nanomechanical properties of 2D materials on nanoscopically rough surfaces, a system that was developed to mimic asperity-asperity contacts[49] was employed (Figure 1.9).

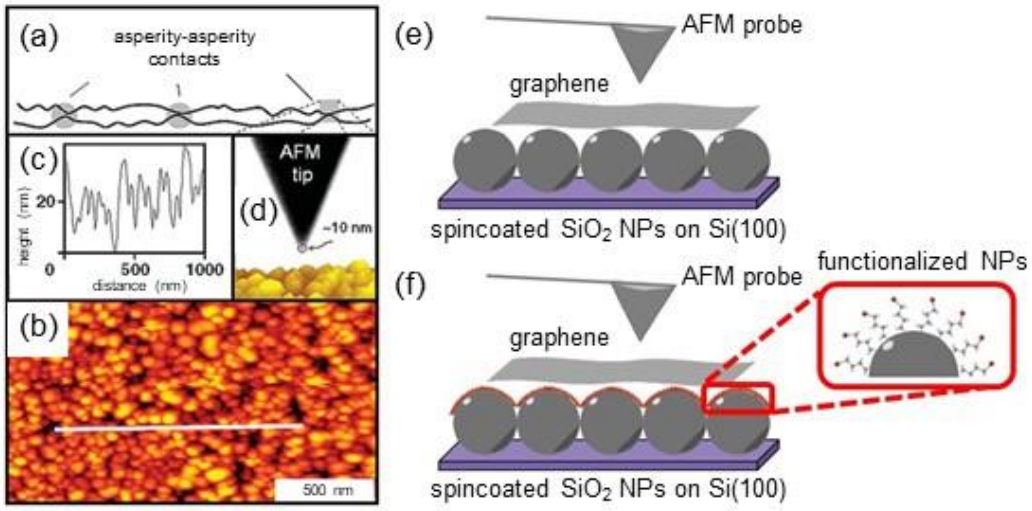

Figure 1. 9. An overview schematic showing the use of nanoparticles and AFM probe to mimic nanoscopic asperity-asperity contacts. (a) Shows the "true" contact area of a nanoscopically rough interface. (b) The AFM topography image in (b) and corresponding cross section in (c) shows a film of silica nanoparticles used to model nanoscopic surface roughness. (d) Side view of the asperity-asperity interaction between an AFM tip with ~10 nm radius of curvature and the nanoparticle film. Adapted with permission from Xu *et al*.[49] Copyright 2008 by Wiley Periodicals, Inc. This system is employed to examine how nanoscopic roughness impacts the properties of 2D materials, shown schematically in (e). The schematic in (f) shows how the system can be further tailored by surface functionalization with self-assembled monolayers to explore the impact of substrate interactions on the properties of 2D materials.

The reduced "true" contact area of nanoscopically rough surfaces (Figure 1.9a) was modeled by a spincoated film of silica nanoparticles (root-mean-square (RMS) roughness of ~25 nm), shown in Figure 1.9b and the corresponding cross section in Figure 1.9c. Figure 1.9d provides a side-view of the tip-sample asperity-asperity contact, where a scanning electron microscopy image (SEM) shows the tip (~10 nm radius of curvature) compared to the nanoparticle (NP) film. Figures 1.9e and 1.9f demonstrate how graphene introduced to the system allowed for the study of its properties in nanoscaled asperity-asperity contacts. Figure 1.9f shows how the system was chemically modified via surface functionalization to explore the influence of substrate interactions, as in the previous study by Spear *et al*.[34]

The morphology adapted by graphene on rough surfaces was predicted by Li *et al*[50] and Wagner *et al*[51] to depend on a balance between elastic strain in the graphene lattice and the strength of the graphene-substrate interaction. Li *et al*[50] examined the morphology of graphene on herringbone and checkerboard surface corrugations with various substrate wavelength/amplitude ratios (on the order of 4-100 nm). The conformity of graphene, as seen in the insets in Figure 1.10a, was defined as the ratio of the graphene sheet amplitude (A_g) to surface amplitude (A_s). An A_g/A_s ratio of 1 described a conformed state, and A_g/A_s approached 0 for a non-conformed state. Plotting A_g/A_s as a function of D/ε (where D was the bending rigidity of graphene and ε was the graphene-substrate bonding energy) showed a sharp transition between the conformed/non-conformed states of graphene as D/ε increased, explained as a "snap-through" instability. The snap-through event was also sensitive to the defined substrate geometry. For example, for the checkerboard substrate

shown in Figure 1.10a, the snap-through instability increased as the surface wavelength increased. The model here, though, may not be realistic as it does not consider different bond strengths between graphene and the substrate at the apex of the surface features vs the suspended regions.

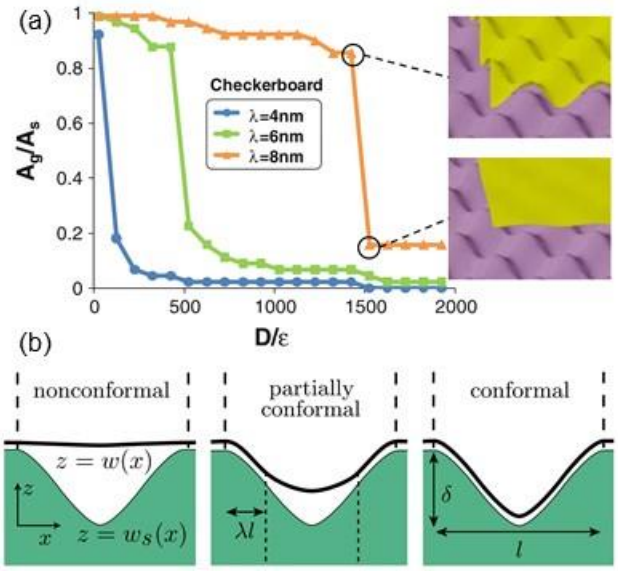

Figure 1. 10. Theoretical predictions of graphene morphology. In (a), a snap-through instability of graphene is observed on a checkerboard patterned surface. The conformity of graphene is represented by plotting A_g/A_s vs D/ε (where A_g and A_s are the amplitudes of the graphene sheet and surface, respectively, D is the bending rigidity of graphene, and ε is the bonding energy). For A_g/A_s near 1, the graphene sheet is completely conformed, which increases as D/ε decreases. A sharp "snap-through" is observed, where the graphene sheet transitions to a state of non-conformity. Adapted with permission from Li *et al*.[50] Copyright 2010 by Springer Open. In (b) an intermediate state between non-conformal and conformal states of graphene is shown as the partially conformed state of few layer graphene. The transition between non-conformal and conformal states was shown to be either a snap-through event or a smooth transition through a partially conformal state before snap-through based on the substrate morphology. Adapted with permission from Wagner *et al*.[51] Copyright 2012 by AIP Publishing.

Wagner *et al*[51] later expanded the predicted morphology of FLG on rough substrates to include an intermediate partially conformed state of graphene (middle panel of Figure 1.10b), similarly dependent on the balance of elastic strain and strength of substrate interaction, as well as being sensitive to substrate geometry. Based on defined surface wavelengths and amplitude (l and δ in Figure 1.10b, respectively), different transitions between the three states were observed. A discontinuous snap-through between conformed/non-conformed states occurred when the curvature of the substrate peaks was too great for the bending energy penalty to be overcome (graphene remained non-conformal) until the adhesion energy was large enough (graphene suddenly transitioned to a conformed state). For different substrate geometries two other transitions were observed, one where the graphene sheet partially conformed before undergoing a snap-through discontinuity, and another where the snap-through event was completely replaced by a smooth transition from non-conformed to conformed states.

Experimental cases of both a snap-through instability and states of partially conformed graphene have been observed. Scharfenberg *et al*[52] reported that FLG underwent a distinct snap-through transition on a grooved Pd/Au substrate (peak-to-peak separation of 1.5 μm and amplitude of ~100 nm). Thicker layers of FLG had a higher bending rigidity, thus the layer thickness tuned the strain energy. The FLG had a critical number of layers (~60 layers) where a sharp transition occurred from a conformed state (<60 layers) to a non-conformed state (>60 layers). The authors did note however, the existence of a narrow region of partial conformity for thicknesses between ~50-60 layers.

A more equilibrated state of partial conformity was observed by Spear *et al*[34] for graphene deposited on a film of 20 nm silica nanoparticles (Figure 1.11). The 20 nm NP film yielded a rough surface with largely equal sized nanoasperities with a peak-to-peak separation of ~20 nm and a RMS roughness of ~9 nm. In the AFM topography image in Figure 1.11a, the NP morphology was still visible under the graphene sheet due to its flexible nature. The corresponding cross section in Figure 1.11b shows the transition from bare NPs to graphene over the NPs by the dashed line. The decreased amplitude of graphene over the NPs indicated the graphene was partially conformed. As the thickness of graphene was increased (Figure 1.11c) the conformity gradually decreased, due to increasing bending stiffness.

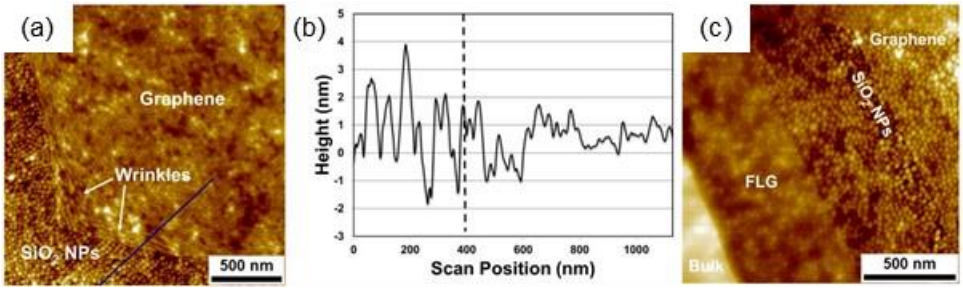

Figure 1. 11. AFM topography images show the morphology of graphene on a film of 20 nm silica nanoparticles. In (a) and the corresponding cross section in (b), the partial conformity of 1LG is observed, with wrinkles observed at the edge of the sheet. In (c), the conformity of the graphene is seen to decrease with increasing layer thickness, due to increasing bending stiffness. Adapted with permission from Spear *et al*.[34] Copyright 2015 by RSC Publishing.

The conformed state of graphene has also been observed to depend on the size of graphene flake (Figure 1.12). In the same system (graphene on 20 nm silica NP films), smaller

graphene flakes approximately 200-500 nm in lateral dimension exhibited pinning to the NPs and wrinkling.

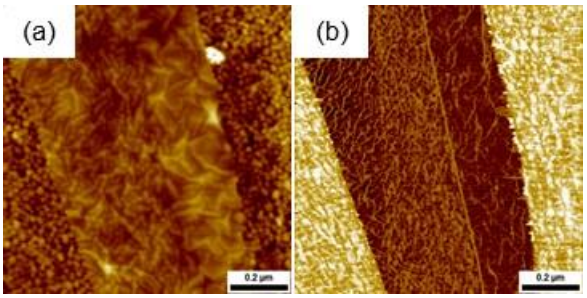

Figure 1. 12. (a) AFM topography image and corresponding FFM image (b) of graphene on 20 nm silica NPs, showing wrinkling for sheet sizes ~200-500 nm across.

Understanding the morphology of graphene on rough substrates can provide insight into the nanotribological responses of graphene under sliding contact. In the work by Spear *et al*,[34] this was manifested in friction force measurements on graphene on a 20 nm NP substrate using a sharp AFM probe (tip radius of curvature, R_{tip}: 32 nm). Given the partially conformed state of graphene, the AFM probe was able to travel smoothly over the graphene/NP surface, which effectively eliminated the layer dependence (or puckering effect) of the frictional response. This effect was seen in the FFM image (Figure 1.13b) where there was no observable contrast in friction between 1LG and 2LG (the corresponding AFM topography image is shown in Figure 1.13a). The friction data was normalized to bulk graphite (plotted in Figure 1.13c) to further illustrate the lack of layer dependence of the frictional response for the sharp probe case (within the error bars). The results were contrasted to using a blunt probe (R_{tip}: 132 nm), where the layer dependence

was recovered (Figure 1.13c) due to the increasing contact area increasing the interaction between the graphene and the top sliding contact.

These results have recently been supported by simulations from Ye *et al*[53] that sought atomistic insights into the underlying mechanisms of friction on graphene regarding roughness. Two opposite layer-dependent trends were observed, based on the relative tip apex size. Together, the experimental findings and simulations emphasize that surface roughness is not the only parameter affecting the layer-dependent frictional behavior of graphene. Consideration also needs to be given to the correlation length (average spacing of topographical features) and the radius of curvature of the sliding tip.

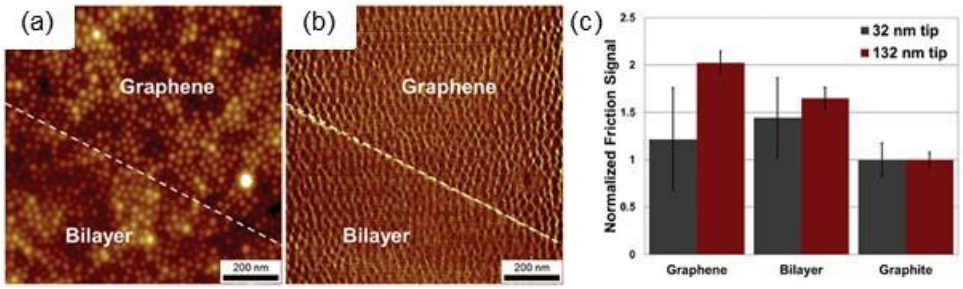

Figure 1. 13. AFM topography image (a) and corresponding FFM image (b) showing no layer dependence of the friction force. The bar plot in (c) shows the normalized friction signal (to bulk graphite) for 1LG and 2LG for sharp (32 nm radius of curvature) and blunt (132 nm radius of curvature) AFM probes. The sharp probe, which corresponds to the images in (a) and (b), shows no layer dependence outside of the error bars. The blunt probe shows the typical layer dependence, with friction force increasing for thinner layers of graphene. Reprinted with permission from Spear *et al*.[34] Copyright 2015 by RSC Publishing.

There are also implications of the behavior of graphene on rough surfaces for the work by Berman *et al*[24] shown in Figure 1.14. In a mixture of graphene patches and

nanodiamonds (Figure 1.14a), graphene nanoscrolls were found to form around the nanodiamonds under sliding contact, achieving superlubricity with a COF as low as 0.004 (Figure 1.14b).

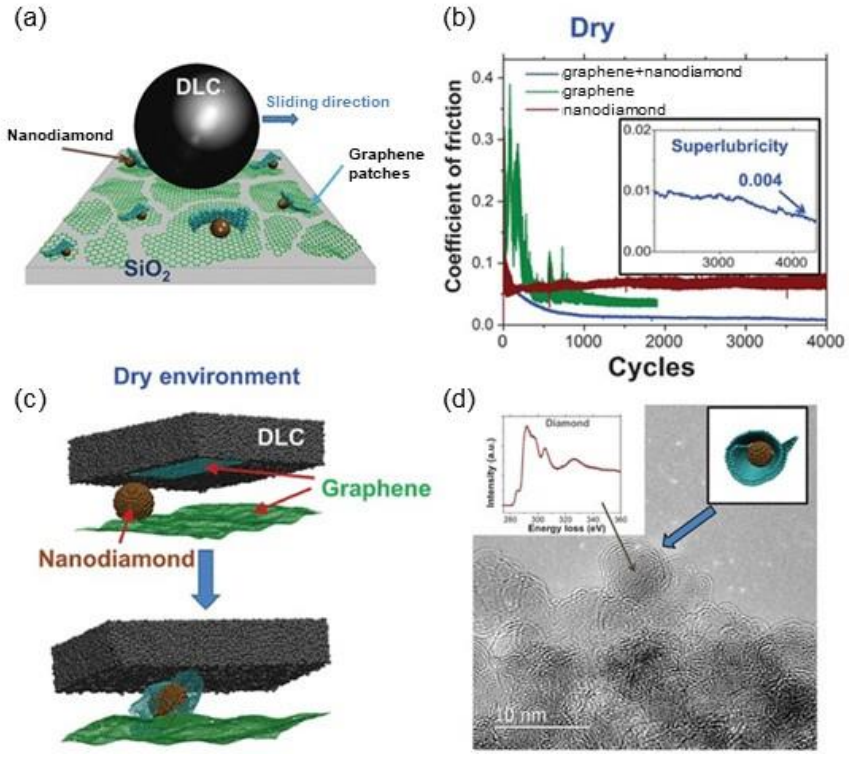

Figure 1. 14. Superlubricity was achieved for graphene nanoscrolls formed around nanodiamonds. The schematic in (a) represents the overall system, with a mixture of graphene patches and nanodiamonds at the sliding interface. The graphs in (b) demonstrate how the coefficient of friction decreased to a state of superlubricity as the graphene nanoscrolls formed during sliding. The coefficient of friction did not dramatically decrease for either graphene or nanodiamonds alone. Further, the scroll formation exhibited an environmental dependence. The nanoscrolls only formed in a dry environment, shown in the MD simulation in (c). (d) Shows a TEM image of the scrolls with the inset showing the electron energy-loss spectrum for diamond at the center of the scrolls. Adapted with permission from Berman *et al.*[24] Copyright 2015 by AAAS.

The superlubricity was unique to the graphene/nanodiamond composite interface, as neither graphene nor the nanodiamonds alone exhibited a dramatically reduced COF (Figure 1.14b). The nanoscrolls, modeled by MD (molecular dynamics) simulations (Figure 1.14c) and visible in transmission electron microscopy (TEM) (Figure 1.14d), only formed under a dry environment. The sensitivity to the environment dictated whether the graphene sheets remained adhered to the SiO_2 substrate or delaminated and scrolled around the nanoscopic diamonds, showcasing how the dynamic behavior of graphene critically depends on a competition between strain and adhesive energies. Chapter IV further explores the dynamic behavior of graphene, using equal deflection imaging to visualize the out-of-plane deformations and force modulation microscopy to examine how out-of-plane interlayer coupling impacts the frictional response of graphene, and how this is ultimately impacted by surface roughness.

To develop a more detailed understanding of how changes in substrate roughness shift the balance of lattice strain and graphene-substrate adhesion energy, the system of graphene on 20 nm silica NPs was expanded to explore varying sizes of NPs (85 nm, 50 nm, 20 nm, 12 nm, and 6 nm). AFM topography images of each are shown in Figure 1.15, including a reference of graphene on nominally flat SiO_2. Figure 1.16 shows the corresponding RMS roughness values of the bare substrates and 1LG regions for a 500 nm^2 area. For each, graphene reduced the measured RMS compared to the exposed substrates. Comparing across NP sizes, the roughness of graphene decreased with decreasing NP size, seen in the cross sections in the inset of Figure 1.16. The roughness trends further reflected the degree of conformity of graphene to the NPs.

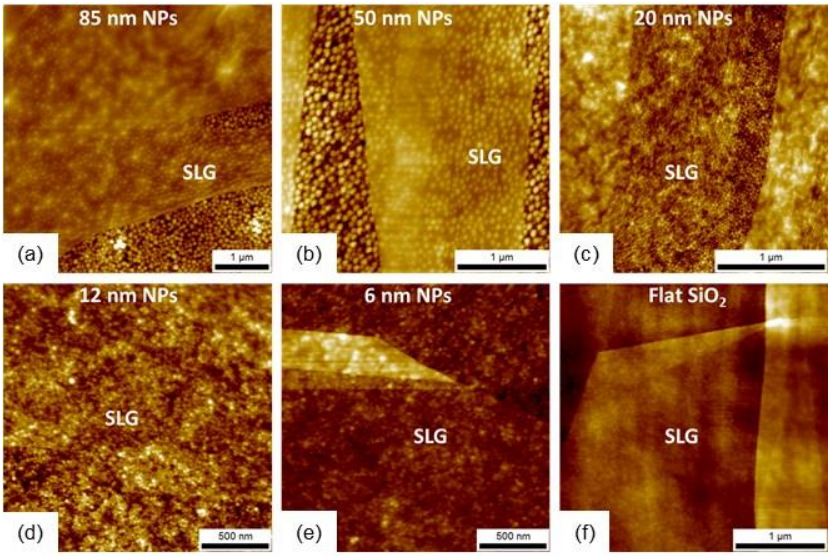

Figure 1. 15. AFM topography images for graphene on substrates with controlled roughness. Images (a)-(e) show the conformity of graphene increases as the NP size decreases. (f) Shows the control sample of graphene deposited on nominally flat SiO_2.

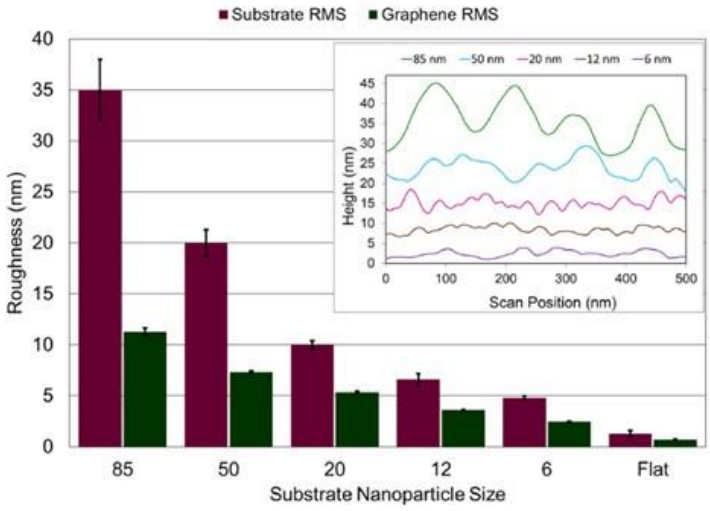

Figure 1. 16. Root-mean-square (RMS) roughness values for the bare surfaces and graphene on each respective shown in Figure 1.15. The inset shows representative cross sections of graphene on each surface, demonstrating the controlled decrease in roughness by varying nanoparticle size.

Graphene was the least conformed for the 85 nm NPs, with more pronounced suspended regions of graphene between the apex of the NPs. As the roughness decreased (smaller NP size), the conformity of graphene increased due to the closer spacing of the NPs and smaller heights. However, this increase in graphene conformity to the NPs was at the expense of lattice strain. As graphene more tightly conformed to nanoscopic asperities, the radial strain induced in the graphene sheet by the NPs increased.

The extent of strain in the lattice was monitored via Raman microspectroscopy by examining the two characteristic Raman mods of graphene, the *G* peak (Figure 1.17a) and *2D* peak (Figure 1.17b).[54] A summary of the spectral data is shown in Table 1.1, compared to data from Zabel *et al*[54] for unstrained and undoped graphene. Examining the data in Table 1.1, as the conformity of graphene to the NPs increased (smaller NP size), the *G* and *2D* peak shift (ΔG and $\Delta 2D$) increased, indicating increased lattice strain.[55-57]

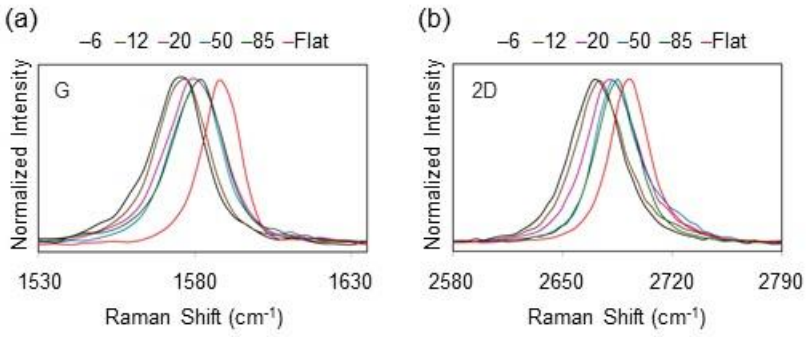

Figure 1. 17. Normalized Raman spectra showing the shifts in the *G* (a) and *2D* (b) peaks for graphene on surfaces with controlled roughness. Both Raman modes shift to lower wavenumbers with increasing strain as graphene-substrate conformity increases.

The 1LG was strained up to 0.15% for the 6 nm NP substrate, calculated from a *2D* shift of 21 cm^{-1}, based on the work by Zabel *et al*[54] that showed a *2D* shift of 140 cm-1 per 1% of biaxial strain.

Table 1. 1. Summary of Raman spectra of graphene on various rough substrates. The *2D* and *G* peak positions, calculated from a Lorentzian fit, and their shifts from unstrained/undoped graphene.[54] The full width at half max values for the *2D* ($\boldsymbol{\Gamma_{2D}}$) and *G* ($\boldsymbol{\Gamma_{G}}$) peaks are also listed, along with the peak intensity ratio (I_{2D}/I_G).

Sample	*2D* (cm^{-1})	*G* (cm^{-1})	Δ*2D*	Δ*G*	$\boldsymbol{\Gamma_{2D}}$	$\boldsymbol{\Gamma_{G}}$	I_{2D}/I_G
Unstrained/Undoped	2692	1582	-	-	-	-	-
Flat	2693	1588	+1	+6	31	14.7	1.75
85 nm NPs	2685	1581	-7	-1	34	19.7	3.3
50 nm NPs	2685	1580	-7	-2	36	19.8	2.2
20 nm NPs	2682	1580	-10	-2	41	22.0	2.4
12 nm NPs	2674	1576	-18	-6	39	20.0	2.2
6 nm NPs	2671	1575	-21	-7	40	20.3	2.7

The degree of conformity of graphene was also reflected in the *2D*/*G* peak intensity ratio, which was shown by Das *et al*[58] to provide insight on chemical doping from the supporting substrate. A lower ratio (for example ~1.8 for graphene on nominally flat SiO_2) indicated higher chemical doping, consistent with graphene having more intimate contact with the substrate. A higher ratio (for example ~3.3 for graphene on the 85 nm NPs) indicated less

chemical doping, largely arising from the suspended regions of the graphene, consistent with decreased conformity.

These results demonstrate how controlling primarily the substrate roughness can shift the balance of elastic strain energy in the graphene lattice and its adhesive interactions with the supporting substrate. As the morphology and nanomechanical behavior of graphene on nanoscopically rough surfaces is regulated by lattice strain and the strength of the graphene-substrate interactions, tuning the substrate chemistry offers another avenue for manipulating the nanotribological properties of graphene.

1.4 Graphene and Substrate Interactions – A Balancing Act

One versatile way to control substrate chemistry is through the use of SAMs. The covalent linkage of silanes to silica surfaces provides a strong attachment for the molecules to the substrate with the terminal tail groups modulating the exposed surface chemistry through a choice of different functional groups.[59] SAMs have been explored as boundary lubricants, but have been found to have reduced performance on surfaces with nanoscopic roughness due to incomplete film formation and the inability to prevent direct substrate-substrate contact.[10, 49, 60-62] These shortcomings combined with the high pressures and shear forces at asperity-asperity contacts lead to their degradation and poor performance in wear tests. Despite their low mechanical stability, SAMs still have many uses in engineering surface properties.[59, 63]

Here, composite interfaces were created by functionalizing flat SiO_2 and spincoated 20 nm silica NP substrates with octadecyltrichlorosilane (OTS) to render a hydrophobic surface.[34] AFM topography images of the rough graphene-OTS and flat

graphene-OTS surfaces are shown in Figures 1.18a and 1.18c, respectively. Figures 1.18b and 1.18d show the corresponding FFM images of each. Figure 1.18e compares the normalized friction force signals using a sharp probe for graphene on 20 nm silica NPs (as discussed in the previous section) to graphene on 20 nm OTS functionalized NPs. While the graphene-silica NP surfaces showed no layer dependence, the graphene-OTS NP composites showed both a layer dependence and an enhanced friction force. The proposed mechanisms is that the combined graphene-OTS surface is mechanically compressed, as OTS is more compliant than the supporting silica NPs. Compression of the composite structure would produce a similar effect of increasing contact area by out-of-plane deformation for thinner graphene layers. Chapter III explores in more detail molecular compression at sliding interfaces and the subsequent impact on shear strain using functionalized AFM tips. Comparing a series of molecules with varying tip-graphene interaction strengths and chain lengths, the OTS functionalized tip did exhibit the highest tip-graphene shear strain, even over a phenyl terminated molecule with a higher interaction strength with graphene.[64]

Figures 1.18f and 1.18g compare the normalized frictional response of the graphene-OTS NP and flat composites, respectively, along with the normalized roughness (normalized to bulk graphite for both friction and roughness measurements). Like the graphene-OTS NP composites, the graphene-OTS flat composites showed a layer dependent frictional response (seen in the bar plots and the contrast between graphene layers in the FFM images).

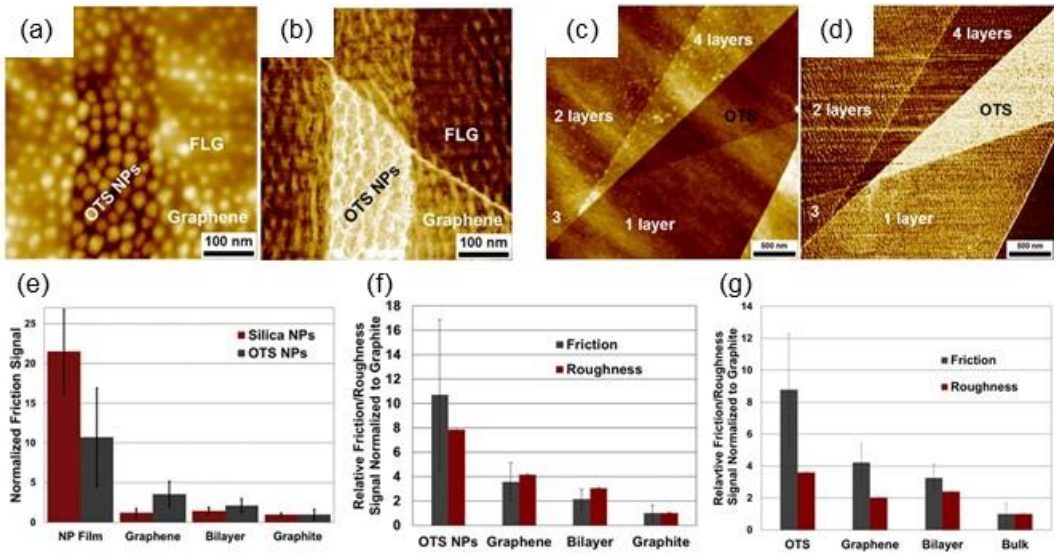

Figure 1. 18. Frictional properties of graphene-OTS composite surfaces. AFM topography (a) and FFM (b) images of graphene on OTS functionalized 20 nm silica NPs are compared to AFM topography (c) and FFM (d) images of graphene on OTS functionalized flat SiO_2. In both composite interfaces, graphene exhibits a layer dependent frictional response. For the NP roughened sample, the bar graph in (e) contrasts the frictional response of graphene on silica particles to graphene on OTS particles. With a sharp AFM probe, the layer dependence of the frictional response of graphene is suppressed for the silica particles (as discussed with Figure 1.13), but the frictional response of graphene on OTS particles has a clear layer dependence. The bar graphs in (f) and (g) compare the NP vs flat graphene-OTS composites. The normalized frictional response of each system is plotted vs the roughness. Adapted with permission from Spear *et al*.[34] Copyright 2015 RSC Publishing.

Comparing the roughness of the flat and NP graphene-OTS composites, 1LG and 2LG on flat OTS had a surface roughness approximately twice that of graphite, and exposed flat OTS had a surface roughness approximately 3.5 times that of graphite. The similar roughness values for 1LG and 2LG on flat OTS contrasted with the OTS NP composite, where the roughness increased as the layer thickness of graphene decreased. This was caused by the conformity of graphene decreasing as the layer thickness increased (due to

increased bending stiffness), so that thicker layers effectively "smoothed out" the underlying NP roughness.

Based on these results, more needs to be considered in using SAMs to control the graphene-substrate interface than pure adhesive interactions alone. Creating a composite graphene/SAM interface introduces the mechanical properties of the molecules, acting as "molecular springs," as an additional variable in modulating substrate interactions.[61] Further, both nanoscopic roughness and substrate interactions greatly influence the nanomechanical behavior of graphene. Consistent with related work in the field,[19, 39, 42, 43, 45, 46] there are competing factors that govern the frictional response of the 2D material, including the bending energy and strain in the graphene sheet, substrate morphology, surface chemistry, and the overall interaction with the AFM probe.

1.5 Comparison between MoS_2 and Graphene

Another variable in the boundary lubrication scheme to be considered is the 2D material itself. Different 2D materials, such as MoS_2, have different chemical structures, leading to different out-of-plane bending moduli, tolerances for lattice strain, and different chemical interactions, all of which are expected to influence their nanotribological properties. One example of the contrasting properties between graphene and MoS_2 is that while graphene is highly conducting,[65] MoS_2 is a semiconductor with an indirect band gap.[66] Mak *et al*[66] however, has shown that MoS_2 transitioned to a direct band gap when exfoliated to 1LM, making 1LM a promising material in optoelectronic applications.[66, 67] Beyond electronic properties, MoS_2 has also been used in lubrication schemes, such as MoS_2 nanoparticles as oil additives.[68] As a boundary lubricant, MoS_2 displayed a similar

layer-dependence as graphene, where 1LM had a higher friction force in nanotribological studies than 2LM, and the friction force continued to decrease with increasing number of layers.[39]

To compare the influences of substrate morphology and substrate interactions on the structure and mechanical behavior of MoS_2 with graphene, a set of experiments were carried out on MoS_2 on 20 nm silica NPs, similar to the graphene studies by Spear *et al*.[34] 1LM partially conformed to the NPs, as seen in the AFM topography image in Figure 1.19a and corresponding cross section in Figure 1.19b. The level of conformity also decreased as the layer thickness increased (Figures 1.19a,b), similar to what was seen for graphene.[34] This bending of the MoS_2 lattice is expected to induce biaxial strain and tune the band gap of 1LM, as has recently been shown by Li *et al*[20] through scanning Raman and photoluminescence spectroscopy (discussed in more detail in the outlook section). The behavior of 1LM was also examined under increasing load (Figures 1.19c-e). Despite a more rigid bonding network for 1LM[69-71] compared to 1LG[15, 72] (the bending stiffness of 1LM is approximately seven times higher than 1LG, as summarized by Jiang[73]), the 1LM membrane stretched downward between the NPs ~2-3 nm, similar to what Spear *et al*[34] has shown for graphene.

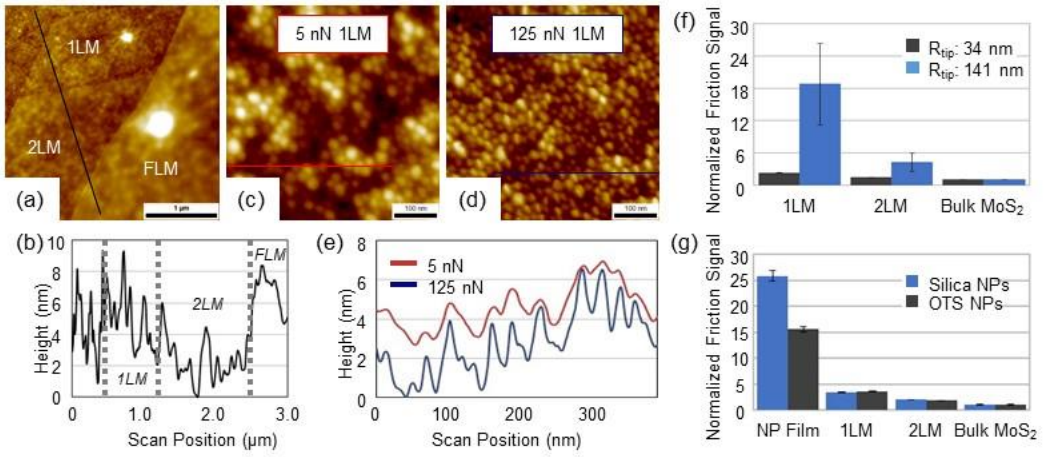

Figure 1. 19. Morphology and mechanical behavior of MoS_2 on 20 nm NPs. (a) 1LM, 2LM, and FLM on 20 nm NPs. The corresponding cross section in (b) shows the 1LM is partially conformed and that the level of conformity decreases as the layer thickness increases, similar to the behavior of graphene. (c) and (d) Show 1LM at 5 nN vs 125 nN applied loads, respectively. In the overlaid cross sections comparing the two loads (e), the 1LM is seen to stretch under higher loading. Note that, as with graphene, this stretching is reversible indicating no damage to the 2D material occurred. To assess the frictional response of MoS_2 on rough surfaces under varying conditions, FFM measurements were carried out at an applied load of 5 nN (normalized to bulk MoS_2) on unfunctionalized NPs with sharp vs blunt tips (f), and carried out on hydrophilic vs hydrophobic (OTS) NPs (g). On the unfunctionalized NPs in (f), the layer-dependent frictional response of MoS_2 does not appear to depend on probe size. 1LM has a higher frictional response than 2LM using either a sharp or blunt probe. However, the difference in the frictional response between 1LM and 2LM is enhanced in the blunt probe case. (g) For both the unfunctionalized and functionalized NP samples, 1LM has a higher frictional response than 2LM, but the layer-dependence appear slightly enhanced in the functionalized NP sample.

Atomic scale images (Figure 1.20) taken on bulk MoS_2, 1LM on top of the 20 nm NPs, and on 1LM suspended between the 20 nm NPs provided further evidence of lattice strain via elongation of the S-S distance. Table 1.2 summarizes the S-S distances.

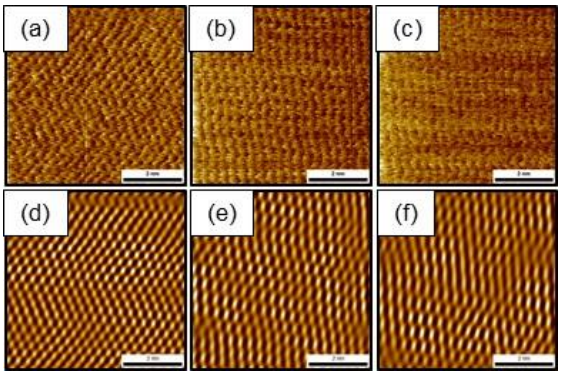

Figure 1. 20. Atomic scale imaging of MoS2 on a 20 nm NP surface. The FFM images show the S-S distances of bulk-like MoS2 (3.18 Å) (a), 1LM suspended between the NPs (3.33 Å) (b), and 1LM on top of the apex of the NPs (3.24 Å) (c). The images in (d)-(f) are the corresponding fast Fourier transform (FFT) images.

Table 1. 2. S-S distances measured from atomic scale imaging of MoS_2 on 20 nm silica NPs.

	Average surface S-S distance (Å)
Bulk MoS2	3.18
On top of NPs	3.24
Between NPs	3.33

This distance for bulk MoS_2 was in close agreement with the value of 3.12 Å calculated from local spin density approximation (LSDA).[74] Due to the higher flexibility of 1LM, the S-S distance was elongated as it was bent over the apex of the NPs, and further deformed between the NPs as the lattice was depressed by the AFM tip. The elongated values,

relative to the bulk, indicated lattice distortions of ~1.9% for 1LM on top of the NPs and ~4.7% for 1LM in between the NPs.

The frictional properties of MoS_2 on the 20 nm NPs were also investigate to evaluate the behavior under sliding asperity-asperity contacts (Figure 1.19f,g). 1LM, 2LM, and bulk MoS_2 on 20 nm silica NP films were measured with sharp vs blunt AFM probes to compare the effects of relative contact size and then measured on bare silica NPs vs OTS functionalized NPs (with a sharp AFM probe) to compare the effects of substrate interactions. The normalized results (to bulk MoS_2) are shown in Figures 1.19f and 1.19g. Note that due to the differences in normalization (normalizing to bulk graphite vs bulk MoS_2), the friction results for MoS_2 cannot be quantitatively compared to the graphene results by Spear *et al*.[34] However, the normalized data can still be used for the purpose of evaluating the relative layer-dependence of each 2D material.

For the frictional response of MoS_2 using different probe sizes (Figure 1.19f), the layer-dependence was present regardless of tip size, unlike with graphene.[34] More specifically, the magnitude of the friction force (F_f) measured with a sharp probe showed that the F_f of 1LM > 2LM but the F_f of 1LG ≈ 2LG. In the work by Spear *et al*[34] the authors noted that 2LG had a higher roughness than 1LG that could have caused the F_f of 2LG to be greater than 1LG (Figure 1.13c), although the difference was within the error bars. This could suggest, however, that for 2LG the top layer was delaminated from the bottom layer as the AFM probe scanned the surface, which could have raised the F_f for 2LG and eliminated the layer-dependence for graphene on the NPs. Then, as 2LM is stiffer than 2LG,[69, 75] this effect did not occur for 2LM and the layer-dependence was retained.

Investigating the influence of substrate interactions, the frictional response of MoS_2 was compared on silica NPs vs OTS functionalized NPs (Figure 1.19g), again as in the studies on graphene.[34] Despite the different chemical interactions for MoS_2 vs graphene on the OTS functionalized NPs, MoS_2 showed a similar enhancement in the layer-dependent frictional response as graphene (Figures 1.18e and 1.19g). This suggests that, consistent with the graphene-OTS composites and the shear strain results in Chapter III,[64] the behavior stems from the lubricating and compliant properties of the OTS film.

1.6 Outlook

Through recent nanotribological studies and the work on nanoscopically rough surfaces discussed here, a picture is beginning to develop for how the frictional responses of graphene and MoS_2 depend on numerous factors. In particular, nanoscopic roughness and 2D material/substrate interactions for both the bottom and top contacts exert a large influence over the observed nanotribological properties of the sliding interface. The balance of these competing parameters merges the effects of chemistry and nanomechanics, which begins to establish the level of molecular scale control of friction that can be achieved. Comparing different 2D materials, such as graphene and MoS_2, helps explore what role the 2D boundary lubricant itself plays in the sliding contact, and what materials might offer a viable route to large-scale production. The ability to modulate the layer-dependence of 2D materials would allow for the design of a lubrication scheme where thinner materials could be used (ie: the single-layer counterparts to FLG or MoS_2) without seeing a rise in the friction force under sliding contact.

Ongoing work in our lab is focused on a systematic investigation of how different non-covalent/covalent interactions between various 2D nanomaterials, the supporting substrate, and the top sliding contact impacts their nanotribological properties on rough surfaces (Chapters III and V). Other future directions for work with 2D materials as solid lubricants include the use of hexagonal boron nitride (hBN) and MXenes as friction modifiers, such that the different chemical interactions, mechanical strengths, and electronic properties that come with a diverse set of 2D materials can be tailored to meet different lubrication demands. The use of nanoparticle surfaces for studies of the influence of controlled roughness can also serve as a platform for a host of other studies. For example, the ability to control nanoscopic roughness and systematically tune the degree of graphene conformity provides a method to explore the dynamic interactions of graphene with the top sliding contact (Chapter IV). Bending 2D materials over surfaces with nanoscopic curvature can also be used to modulate the electronic properties or chemical reactivity of these materials as a function of bond strain.[20, 76-80]

To understand how strain alters the chemical reactivity of graphene, it is important to first understand how strain is spatially distributed across the bond lattice. Work by Beams *et al*[76] measured local strain in graphene suspended over a 5 nm NP (Figure 1.21a) using tip-enhanced Raman spectroscopy (TERS). In this case, the radial static strain field induced by the particle was spatially resolved and showed a gradient in strain over the NP monitored by shifts in the *G* and *2D* peaks. Figure 1.21b shows the AFM topography cross section of graphene over the NP and Figure 1.21c shows the spatially resolved *2D* peak

position (labeled *G'*) and measured strain. A maximum strain of 0.37% in the graphene lattice occurred at the apex of the NP.

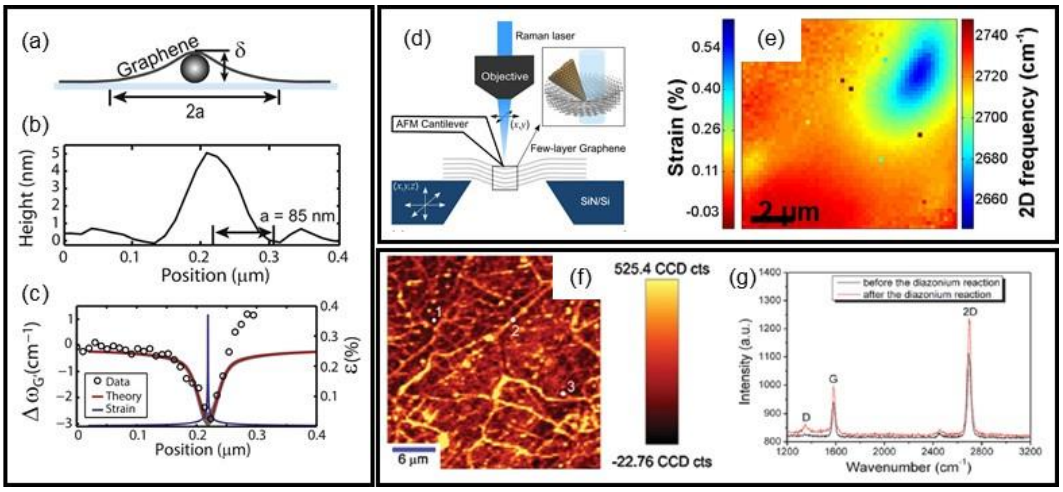

Figure 1. 21. Localized strain and reactivity of graphene. Graphene suspended over a NP is shown schematically in (a). A cross section from an AFM topography scan in (b) shows that the maximum amount of strain corresponds to the top of the NP. The spatially resolved strain is shown in (c), based on the plotted shifts in the *2D* Raman peak (labeled as *G'*). Adapted with permission from Beams *et al*.[76] Copyright 2015 by IOP Publishing. A schematic of the setup for monitoring strain in FLG by Raman spectroscopy during AFM indentation is shown in (d). A Raman map of the area around the point of indentation (e) at an applied load of 6300 nN shows that the shift in the *2D* peak and corresponding strain distribution is localized to under the AFM tip. Adapted with permission from Elibol *et al*.[77] Copyright 2016 by Macmillan Publishers Limited. The Raman map in (f) shows the intensity variation of the *D* peak of graphene deposited over 50 nm silica NPs on a Si substrate after chemical treatment. The Raman single spectra in (g) correspond to location 3 in the Raman map, showing an enhancement in the *D* peak after chemical treatment at a location of increased strain induced by the high curvature of the wrinkles. Adapted with permission from Wu *et al*.[78] Copyright 2013 by RSC Publishing.

About a year later, Elibol *et al*[77] used AFM to indent suspended FLG and monitored localized strain via laterally resolved Raman spectroscopy measurements (Figure 1.21d). Raman maps of the *G* and *2D* vibrational modes were generated for systematically varied

applied loads by the AFM tip. Figure 1.21e shows the map of the *2D* peak with an indented load of 6300 nN. Colored scale bars show both the frequency shit and measured strain (based on the frequency shifts). The greatest frequency shift, which corresponded to the region of highest strain, was localized under the AFM tip. The strain induced by indentation increased as the applied load increased, and was also reversible (the Raman signature reverted to the initial peak frequencies upon removal of the AFM tip).

Localized strain induced by the mechanical deformation of graphene was shown by Wu *et al*[78] to lead to selective spatial functionalization. CVD graphene that was deposited on a Si substrate decorated with 50 nm SiO_2 NPs showed increased wrinkles. Curvature-induced enhancement of the chemical reactivity of graphene was observed by monitoring the *D* peak intensity, which in the study indicated covalent attachment of aryl radicals generated from 4-nitrophenyl diazonium tetrafluoroborate. The Raman map in Figure 1.21f shows the *D* peak intensity after chemical treatment. The greatest intensity followed along the wrinkles in the sheet. Raman single spectra taken before and after the reaction (at location 3 in the map in Figure 1.21f) show the enhanced *D* peak after the addition of the nitrophenyl (Figure 1.21g).

Strain induced by nanoscopic surface features has also been shown to modify the properties of MoS_2. As mentioned in the previous section comparing MoS_2 with graphene, Li *et al*[20] demonstrated tuning the band gap of 1LM by inducing biaxial strain through the 1LM bending over silicon nanocones. An AFM topography image of the textured 1LM is shown in Figure 1.22a and a schematic of the system is shown in Figure 1.22b. Scanning Raman spectroscopy was used to resolve the spatially varying strain distribution by shifts

in dominant MoS_2 peaks, the E^1_{2g} vibration mode at 385.6 cm^{-1} and A_{1g} vibration mode at 404.9 cm^{-1}.

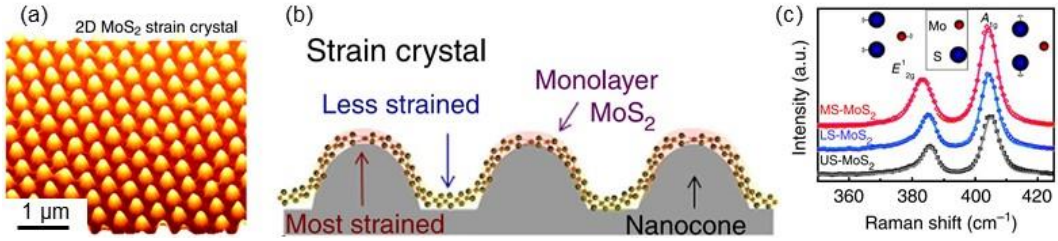

Figure 1. 22. Strain in nanotextured MoS_2. The AFM topography image (a) shows 1LM deposited over silicon nanocones. The 1LM was most strained at the top of the nanocones, as labeled in (b), and less strained between the nanocones. Strain in the lattice was monitored by Raman spectroscopy, shown in (c). The most strained MoS_2 (MS-MoS_2) shows the largest shifts of the $\boldsymbol{E^1_{2g}}$ and $\boldsymbol{A_{1g}}$ vibrational modes. The less-strained MoS_2 (LS-MoS_2) shows a smaller spectral shift than the MS-MoS_2, but is still slightly shifted from unstrained MoS_2 (US-MoS_2) on flat SiO_2. Adapted with permission from Li *et al*.[20] Copyright 2015 by Macmillan Publishers Limited.

The most strained (MS-MoS_2), seen as the greatest peak shift in Figure 1.22c, was on the tips of the nanocones as labeled in Figure 1.22b. Less strained MoS_2 (LS-MoS_2), relative to unstrained MoS_2 (US-MoS_2) deposited on flat SiO_2, was positioned between the nanocones (Figures 1.22b,c). It was estimated from the magnitudes of the peak shifts that the biaxial tensile strains were ~0.23% for LS-MoS_2 and ~0.57% for MS-MoS_2. The implications of tuning the strain in MoS_2 are extensive, as strain in the lattice plays an important role in tuning its electronic properties.[67, 81] Beyond the nanotextured surfaces, Li *et al*[20] also studied MoS_2 as a catalyst in the hydrogen evolution reaction (HER) as a function of strain.[80] While strain alone slightly increased the HER activity of MoS_2, the

introduction of sulfur vacancies created new catalytic sites in the basal plane, and the subsequent combination of sulfur vacancies and lattice strain fine-tuned the catalytic activity.

These studies show that beyond impacting nanotribological properties, nanoscopic surface roughness and locally induced strain plays a larger role in the broader electronic and chemical applications of 2D materials. There remains much to be explored given the complex relationships between substrate morphology, 2D material structure, strain vs adhesion energies, and their combined impact on interfacial properties.

1.7 Conclusions – 2D or not 2D?

2D materials are promising candidates for boundary lubricants in diverse settings. Graphene has been studied on a variety of supporting substrates, ranging from atomically smooth to nanoscopically rough surfaces. Different phenomena have been observed during load studies with and without breaking contact with the graphene sheet, comparing supported graphene to suspended graphene, examining vdW screening, and studying tribological properties under humid vs dry conditions. These studies have demonstrated and emphasized the impact of out-of-plane deformation on the frictional response of 1LG. The surface bound morphology of graphene depends on a balance of elastic strain energy and bonding energy between graphene and the supporting substrate, and in sliding contacts the relative interactions between the sliding surfaces can shift that balance. Here the impacts of strain and adhesive energies can be tuned by using SAMs to control graphene-substrate interactions. Comparing graphene with MoS_2 on nanoscopically rough surfaces and chemically functionalized substrates has shown that MoS_2 has largely similar

nanomechanical behavior as graphene. The only case where a difference was observed between graphene and MoS_2 was when the materials were deposited on 20 nm silica NP films and measured with a sharp AFM probe. Graphene did not exhibit a layer dependence while MoS_2 did, most likely due to MoS_2 having a higher bending stiffness.

Building from these studies, this dissertation further explores the frictional properties of graphene in controlled sliding contacts that are molecularly modified and have tuned surface roughness. Chapter II provides an overview of the principles of the different AFM methods used. Chapter III explores the competition between tip-graphene adhesion and interfacial shear strain in adhesion and friction measurements with molecularly modified AFM tips. Then, focusing on the dynamic flexibility of graphene as a layered material, Chapter IV includes a detailed investigation of the out-of-plane motion and force modulated sliding responses of single and few layer graphene. Considering both aspects of the molecularly controlled frictional response of graphene (Chapter III) and the out-of-plane motion (Chapter IV), Chapter V aims to use patterned, functionalized surfaces to periodically immobilize graphene via covalent pinning. Since chemical functionalization of graphene will also alter its electronic properties, the modulated frictional response is compared with optoelectronic measurements from scattering-type scanning nearfield optical microscopy (s-SNOM).

As nanotribological studies of 2D materials progress, the core understanding of their behavior as boundary lubricants is centralized around the competing interactions of the bottom vs top contacts, which can be tuned based on both substrate roughness and surface chemistry. Systems of single layer materials on nanoscopic asperities are also

poised to play a role in understanding strain-driven spatially controlled chemical reactions on such materials. Future work should continue to explore the behavior of 2D materials on realistically rough surfaces and how controlling substrate interactions can modify their behavior, allowing for advanced designs/tailorable lubrication schemes.

CHAPTER II

ADVANCED ATOMIC FORCE MICROSCOPY METHODS

2.1 Basic Principles of Atomic Force Microscopy

Atomic force microscopy (AFM) is a scanning probe technique that implements a sharp probe to characterize a surface. In addition to collecting topographic images by raster scanning the surface of a sample, extensive characterization of tip-sample interactions can be achieved. It is a highly versatile technique, able to acquire topographic images and perform quantitative measurements of a wide variety of samples in many different environments. Samples can span conductive and non-conductive materials, hard elastic materials, and softer materials such as polymers and biological species. These samples can be characterized in environments including vacuum, dry nitrogen conditions, ambient air, or liquid. The basic scanning modes include contact mode, tapping mode, and non-contact mode, although the focus here will be on contact mode and tapping mode.[82-85] For more comprehensive and quantitative analyses, advanced AFM modes (discussed in the following sections) can be implemented, such as friction force microscopy (FFM), force-volume (FV) mapping, force modulation microscopy (FMM), and scattering-type scanning nearfield optical microscopy (s-SNOM).

In the basic operation of AFM, a sharpened probe is brought into physical contact with a surface (either constant or intermittent contact for contact or tapping mode, respectively) (Figure 2.1). The probe, or tip, is most commonly only a few tens of nanometers in radius, and extends downward from the end of a cantilever. To image the

sample, the probe is rastered over the surface via a piezoelectric scanner. Changes in the surface topography are monitored by tracking cantilever bending/twisting. This is done by reflecting a laser off the back of the cantilever to a four-quadrant photodetector. By comparing the cantilever responses to a set parameter (generating an error signal), a feedback loop adjusts the height of the piezo scanner as the surface is imaged. The output of the feedback loop is recorded at each pixel and compiled to generate a topography image of the surface. The set parameter for the feedback loop is defined according to the user and the AFM mode.[82-85]

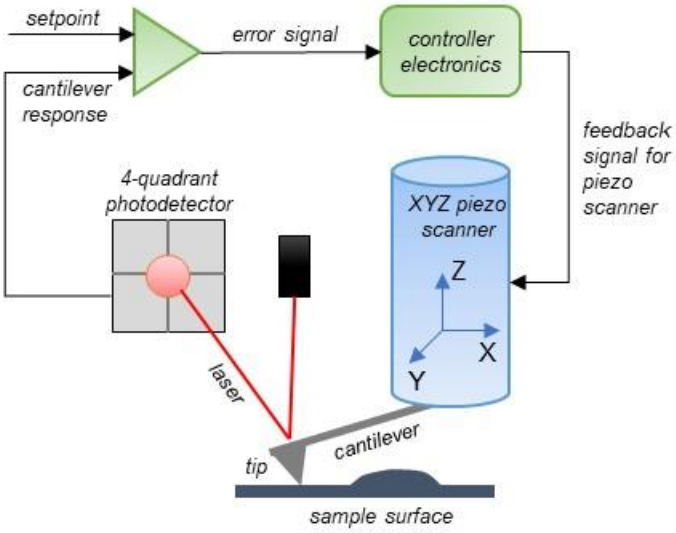

Figure 2. 1. Illustration of the AFM tip in contact with surface and the feedback loop that monitors cantilever deflection and controls the piezo scanner. Modified from the 5500 SPM User's Guide.[84]

The two most regularly used AFM modes are contact mode and tapping mode. In contact mode, the AFM tip is rastered across the sample in continuous physical contact.

The cantilever deflection as the tip bends in the vertical direction is monitored (Figure 2.2a), using the feedback loop to maintain a constant applied load (defined by the user as the setpoint).

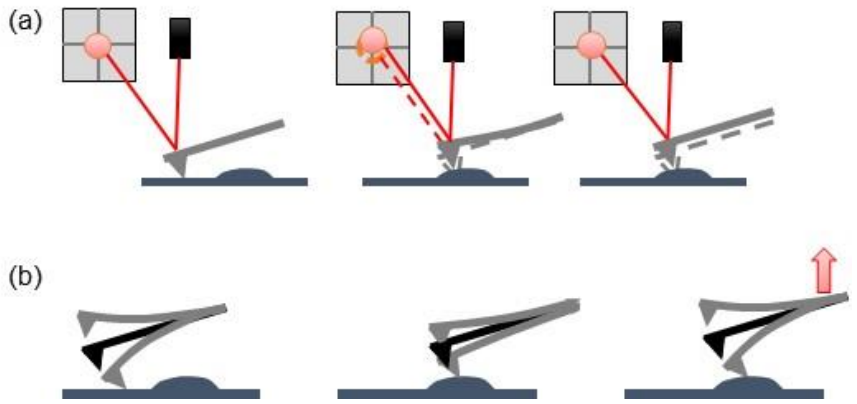

Figure 2. 2. (a) Schematic of the change in cantilever deflection, and subsequently scanner z-position, in response to surface topography features in contact mode. (b) Schematic of changes in cantilever oscillation amplitude in response to surface topography features, and subsequent change in scanner z-position, in tapping mode.

A less common form of contact mode is constant height imaging, where the gain for the feedback loop is set to zero, the scanner rasters at a constant height, and the error signal is recorded to generate a topographic-like image (though this is not direct topographic information). In tapping mode (also called intermittent contact mode, or AC mode for alternating contact), the probe/cantilever is driven to oscillate in a sinusoidal motion by a piezoelectric transducer that shakes the cantilever holder. As the tip interacts with the sample, the oscillation amplitude of the cantilever motion is dampened (Figure 2.2b). The

feedback loop is then used to maintain a constant oscillation amplitude, as defined by the user.[82-85]

Contact mode and tapping mode AFM are both employed for more advanced data acquisition techniques, in addition to other developed derivatives of AFM. In contact mode, torsional (lateral) twisting of the cantilever is induced in addition to vertical deflections. The lateral twisting is due to the frictional forces at the tip-sample contact opposing the forward sliding motion of the tip. This forms the basis of friction force microscopy (FFM, Section 2.2).[33, 35, 86, 87] In addition to FFM, the AFM can be used to acquire other mechanical data that is sensitive to chemical properties. Force-distance (FD) curves monitor the vertical cantilever deflection as the tip is approached towards, indented into, and retracted from the surface. The indentation into the surface can be used to calculate the Young's modulus of the sample, while the pull-off force can be a measure of various tip-sample interactions (van der Waals forces, electrostatic forces, capillary forces, hydrogen bonding, or covalent bonding). Further, force-volume (FV) mapping (Section 2.3) acquires a series of FD curves in a grid-like fashion at a specified pixel density to spatially map and quantify surface variations in the tip-sample interactions.[88, 89]

Hybrid contact-tapping modes have also been developed, such as force modulation microscopy (FMM) and scattering-type scanning nearfield optical microscopy (s-SNOM). In FMM (Section 2.4), the cantilever is driven to vertically oscillate as in tapping mode while maintaining continuous contact at a defined load as in contact mode.[84, 90] In s-SNOM (Section 2.5), the diffraction limit of optical microscopy is overcome to access insight into

chemical and physical phenomena at the high spatial resolution routinely provided in scanning probe techniques.[91, 92]

2.2 Friction Force Microscopy

2.2.1 Overview of Friction Force Microscopy. When operating an atomic force microscope in contact mode, friction force microscopy (FFM) images are routinely simultaneously recorded by monitoring the lateral deflections of the cantilever.[33, 35, 86, 87] Recording this torsional twisting in both the scan trace and retrace directions across a single line produces a friction loop. Typically, the average friction force value for an interface is reported as TMR/2, where TMR is the trace value (positive signal) minus the retrace value (negative signal).[93] Moreover, recording the lateral signal over the entire scan yields trace and retrace friction images that are inverses of each other, as the signal changes to opposite directions for the opposing sliding directions (Figure 2.3). This data can be used to both qualitatively and quantitatively (through cantilever calibration) compare and measure specific sample regions of nonhomogeneous surfaces or assess the frictional properties of different samples.[33, 35, 86, 87]

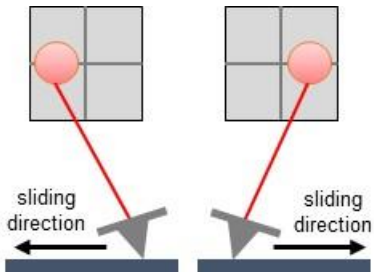

Figure 2. 3. Schematic of the lateral twisting of the cantilever and the inverse photodetector response for opposing sliding directions, that arises from the trace and retrace movement during raster scanning.

The forces and energy dissipation for two surfaces in sliding contact are highly complex and depend on the structure, chemistry, elastic properties of the surfaces, on the chemical environment used to take the measurements, and on the sliding history of the interface.[33] Due to this complexity FFM is a useful route to gaining fundamental insights into mechanical interactions, largely because an AFM tip can represent a single sliding asperity allowing for investigations of well-defined systems.[33] In this manner, FFM has been implemented for diverse studies such as monitoring wear,[94] observing the growth of tribofilms,[95] and elucidating relationships between friction, adhesion, and shear.[33, 35, 86, 87] Moreover, as discussed in Chapter I, there is a wide breadth of FFM studies focused solely on the nanotribological properties of 2D materials. A critical challenge in being able to draw meaningful comparisons between separate studies, however, is quantitative calibration of the measured lateral forces, discussed in the following section.

2.2.2 Lateral Force Calibration. To calibrate the lateral forces measured in FFM, both the lateral detector sensitivity and the torsional spring constant of the cantilever must be known. Many methods[96-108] have been developed to achieve this and several reviews have been written comparing and contrasting the different options.[109-113] Munz *et al*[110] classified a number of the methods based on how torsional deformation is induced in the cantilever. The five major groups identified directly applied a force off the long axis of the cantilever, loaded the tip-substrate contact in the lateral direction, loaded a known compliant structure, scanned across a surface with a wedge geometry, or excited the torsional cantilever resonance. Each method derives equations to ultimately obtain a conversion factor (to calibrate from the photodetector signal in V to a force value in N).

More importantly, each method has its own set of assumptions, advantages, and disadvantages for the calibration procedure. For the work here, a corrected direct force balance method was used[100] due to the minimization of scanning, preserving the tip radius.

2.3 Force-Volume Mapping

2.3.1 Basics of Force-Distance Curves. Beyond the lateral tip-sample forces that are measured in friction force microscopy, other tip-sample interactions can be directly probed via force distance (FD) spectroscopy.[88, 89] To acquire an FD curve, the tip is approached toward and then retracted from the surface, measuring the vertical deflection of the cantilever as tip-sample contact is formed and then broken. During the approach curve, the tip is first out of contact and there is no measured cantilever deflection (the "non-contact region" in Figure 2.4). As the tip nears the surface, there is a "snap-in" event where the tip snaps into contact with the surface when the tip-sample attractive forces overcome the spring constant of the cantilever. Then, as the tip is "indented" and the applied load increases, the deflection rises. During the retract curve, as the tip is withdrawn from the surface hysteresis arises from adhesive forces, seen as the extended "contact region" in Figure 2.4. The tip continues to be withdrawn until it "snaps" out of contact. This pull-off force is a measure of total tip-sample adhesion, which can consist of capillary forces, van der Waals forces, electrostatic forces, hydrogen bonding, or covalent bonding.[88, 89]

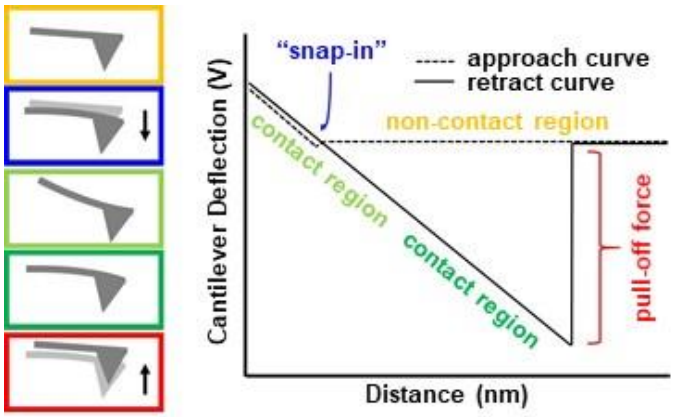

Figure 2. 4. Schematic of a force-distance (FD) curve. The motion of the cantilever is shown in the vertically stacked boxes, from top to bottom. Each box correlates to a defined region of the example FD curve.

By measuring the pull-off force, the total tip-sample adhesion is probed, offering insight into the strength of the interactions present at specific surface locations. These adhesion values can be evaluated in terms of total force (typically in nN) through proper calibration procedures, and further compared across diverse tips and samples via contact mechanics models.[88, 89] Calibration involves determining both the normal spring constant of the cantilever and the vertical sensitivity of the photodetector, analogous to calibration of lateral forces. Both values should be determined in situ. The spring constant can be determined through a variety of methods, such as the Sader method,[114] used here. The sensitivity of the photodetector is determined as the slope of the FD curve against an ideally hard surface.[115]

2.3.2 Applying Contact Mechanics Models. To quantitatively compare measured pull-off forces across different tip/sample systems, the adhesion values can be used to calculate the tip-sample work of adhesion, effectively "normalizing" the pull-off force

with respect to the tip radius of curvature (R_{tip}). Using a continuum description of nanometer sized contacts, there are three primary models. These are the Hertz model, the Derjaguin-Muller-Toporov (DMT) model, and Johnson-Kendall-Roberts (JKR) model.[88, 89, 116] For two spheres in contact, the Hertz model assumes the materials are homogeneous, isotropic, and linear elastic, with no adhesion, and that the contact radius is much less than the sphere radius.[117] The Hertz contact radius (a_{Hertz}) is defined in eq 2.1, as adapted to an AFM set-up where a tip with radius of curvature R_{tip} is in contact with a flat surface at an applied load, L.

$$a_{Hertz} = \left(\frac{LR_{tip}}{K}\right)^{1/3} \tag{2.1}$$

In eq 2.1, K is the reduced Young's modulus of the tip-sample contact (eq 2.2), with ν_1 and E_1 the Poisson ratio and Young's modulus of the tip, and ν_2 and E_2 are the Poisson ratio and Young's modulus of the surface.

$$K = \frac{4}{3}\left(\frac{1-\nu_1}{E_1} + \frac{1-\nu_2}{E_2}\right)^{-1} \tag{2.2}$$

The DMT contact model assumes the same deformed contact profile as in the Hertz model, while accounting for additional load from the adhesive forces.[118] Here, the attractive forces act as "dead weight" over the interaction range, and the contact area is zero at pull-off. This adhesion-modified contact radius, a_{DMT}, is defined in eq 2.3, with the DMT work of adhesion (w_{DMT}) defined in terms of the adhesive force (F_{adh}, or pull-off force) and tip radius (eq 2.4).

$$a_{DMT} = \left[\frac{R_{tip}}{K}\left(L + 2\pi w_{DMT} R_{tip}\right)\right]^{1/3} \tag{2.3}$$

$$w_{DMT} = \frac{F_{adh}}{2\pi R_{tip}} \quad (2.4)$$

The JKR contact model also accounts for adhesion, including terms for the adhesive forces between two elastic bodies and defining a finite contact area at zero applied load.[119] The contact radius (a_{JKR}) and work of adhesion (w_{JKR}) are defined in eq 2.5 and eq 2.6, respectively.

$$a_{JKR} = \left[\frac{R_{tip}}{K}\left(L + 3\pi w_{JKR} R_{tip} + \sqrt{6\pi w_{JKR} R_{tip} L + \left(3\pi w_{JKR} R_{tip}\right)^2}\right)\right]^{1/3} \quad (2.5)$$

$$w_{JKR} = \frac{2F_{adh}}{3\pi R_{tip}} \quad (2.6)$$

When there is measurable adhesion in AFM systems, the DMT and JKR contact mechanics models should be applied over the Hertz model. Though the DMT and JKR models seem at odds, they define the two limiting cases. The DMT model is applicable for weak, long-range (inside and outside the contact area) adhesion forces and ideally hard interfaces, while the JKR model is applicable for strong, short-range (inside the contact area) adhesion forces and soft materials.[116] In reality, most systems lie in an intermediate regime, and Tabor's parameter (μ_T) can be calculated as a non-dimensional physical parameter to quantify the DMT-JKR limits and intermediate cases. Tabor's transition parameter (eq 2.7) physically represents the ratio between the normal elastic deformation from adhesion and the spatial range of the adhesion forces.

$$\mu_T = \left(\frac{16 R_{tip} w^2}{9K^2 z_0^3}\right)^{1/3} \quad (2.7)$$

For evaluating which contact model to use, Maugis defined a transition parameter λ, where $\lambda = 1.1570\mu_T$. For $\lambda < 0.1$ the DMT model should be applied, for $\lambda > 5$ the JKR

model should be applied, and for $0.1 < \lambda < 5$, the contact behavior is in the transition regime. An experimental dilemma arises in evaluating the transition parameter because the work of adhesion (w) is not known without knowing μ_T, but μ_T is not known without knowing w and z_0. To reconcile this, upper and lower bounds can be checked as described by Grierson *et al*,[116] or the transition parameter can be explicitly solved for using the generalized transition equation defined in the COS method by Carpick *et al*.[120] Once a model has been chosen, then the work of adhesion (in J/m^2 or N/m) and contact areas can be used to more appropriately compare both AFM adhesion and friction measurements across different tip-sample systems. For example, as discussed in Chapter III, the contact area at pull-off can be used in combination with a known species density to calculate the tip-sample interaction energy in kcal/mol.[64] At no load, the JKR contact radius reduces to the critical radius (r_c) in eq 2.8. Then the contact area at pull-off, A_c, is calculated as $A_c = \pi r_c^2$.

$$r_c = \left(\frac{3\pi w_{JKR} R_{tip}^2}{2K}\right)^{1/3} \tag{2.8}$$

Multiplying the work of adhesion by A_c yields the tip-sample energy in Joules, while multiplying the species density (e.g. molecules/m^2) by A_c yields the number of interacting species (e.g. number of molecules). Then the J/molecule ratio can be converted to kcal/mol through unit conversion and Avogadro's number.

2.3.3 Extending FD Analysis in Force-Volume Mapping. The detailed analyses possible through FD curve measurements at single locations can be extended to spatially resolve tip-sample properties through force-volume (FV) mapping. In FV mapping, FD

curves are acquired in a grid-like fashion at a defined pixel density. In this manner, a full FD curve is collected at each pixel, shown schematically in Figure 2.5.[88, 89]

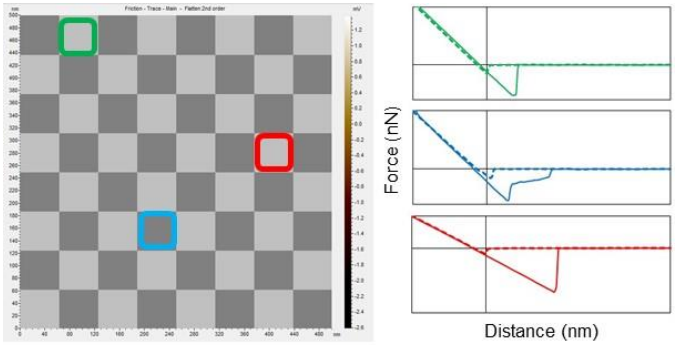

Figure 2. 5. Schematic of an 8 x 8 pixel FV map with example individual FD curves extracted from each point.

In defining the pixel density, it is important to consider the resolution in terms of total surface area being probed along with the tip-sample contact area. Other parameters that should either be held constant or varied in a controlled manner are the approach and retract rates, the maximum applied load, tip-sample dwell time, and the total vertical distance over which the FD curve is acquired.

Additional information that can be extracted from FD curves and further spatially resolved in FV maps include mechanical properties such as Young's modulus and the dissipated energy. The Young's modulus can be calculated by changes in the slope of the FD curve with respect to an ideally hard surface, and the dissipated energy can be calculated as the area between the approach and retract curves.[89, 115] The vertical

indentation of sample surfaces can also be visualized by extracting equal deflection images at specific loads, discussed further in Chapter IV.

2.4 Force Modulation Microscopy

2.4.1 Force Modulation Microscopy Operating Principles. In force modulation microscopy (FMM) either the cantilever or the sample is driven to vertically oscillate in a sinusoidal wavefunction with user defined drive frequency and drive amplitude (Figure 2.6a).[84, 90]

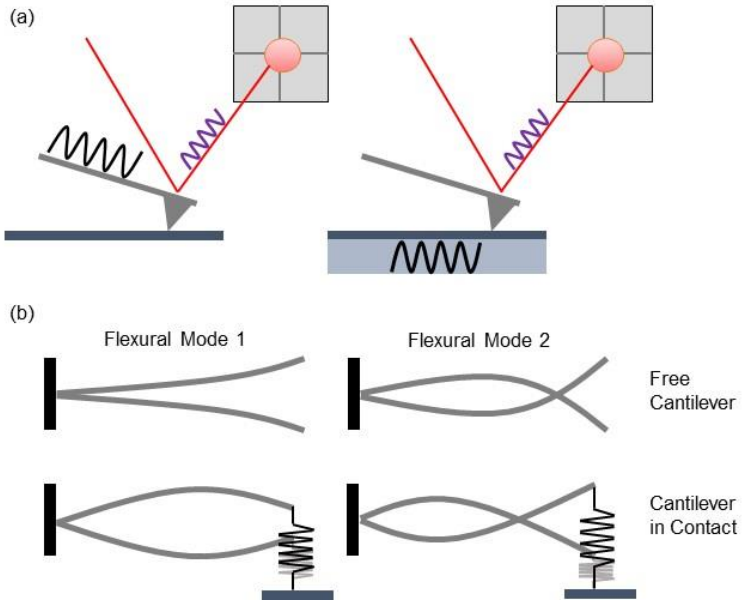

Figure 2. 6. (a) Illustration of FMM where either the base of the cantilever is driven to oscillate or the sample is driven to oscillate. In either scenario, the resulting amplitude of the tip-sample contact is monitored and any phase shift between drive signal and detected signal. (b) Examples of cantilever motion for the first two flexural vibrational modes for the freely oscillating cantilever and for the cantilever when it is coupled to the surface at the tip-sample contact.

FMM is operated in contact mode AFM, where the feedback loop maintains a constant applied load and the tip is in continuous contact with the sample. To achieve this, the drive amplitude is kept low, typically 1-50 nm, and the drive frequency (>10 kHz) is above the response of the feedback circuit (a few kHz) to minimize coupling with the electronics and allow for the topography and detected amplitude oscillations to be deconvoluted.[84, 90] The amplitude and phase response of the cantilever is extremely sensitive to the elasticity and viscoelasticity of the coupled tip-sample contact. Generally, for softer materials the amplitude is dampened, or lower, compared to harder materials.[84, 90] A derivative of FMM, contact resonance-AFM (CR-AFM), images at a frequency where the tip-sample contact is in resonance.[84, 121, 122] These contact resonances are identified through frequency spectra, where the amplitude response of the cantilever when the tip is contact with the sample is monitored over a range of drive frequencies. Multiple peaks are typically seen that correspond to the different flexural eigenmodes (Figure 2.6b),[123] and can be predicted for freely oscillating cantilevers using the Euler-Bernoulli beam model (eq 2.9).[123-125]

$$f_f = \frac{(x_n^o L)^2}{2\pi L^2}\sqrt{\frac{EI}{\rho A}} \tag{2.9}$$

In eq 2.9, f_f is the resonance frequency of the freely oscillating cantilever for eigenmode n. L is the length of the cantilever, E is the Young's modulus of the cantilever, ρ is the cantilever density, and A is the cross-sectional area (defined as the cantilever width, w, times the thickness, t), and I is the second moment of area (defined as $w*t^3/12$).

The corresponding root ($x_n^o L$) of the characteristic equation for free flexural vibration (eq 2.10) is 1.8751, 4.6941, and 7.8548 for n = 1, 2, and 3, respectively.

$$1 + \cos(x_n^o L)\cosh(x_n^o L) = 0 \tag{2.10}$$

It is useful to calculate the expected resonance frequencies for the first few flexural eigenmodes of a given cantilever in order to help identify the measured resonance peaks in moving forward with parameter optimization and data collection.[123-126]

2.4.2 FMM Parameter Optimization. For extracting quantitative information from FMM studies, such as the dynamic energy storage and loss moduli, the user defined parameters must be carefully optimized. The primary parameters are the chosen cantilever, drive amplitude, drive frequency, and applied load.[90] While for a specific study a number of these parameters may be systematically varied (e.g. imaging at different applied loads or drive frequencies to observe changes in the amplitude and phase response) it is still critical to fully test each system. The best choice for cantilever resonance frequency (RF) and spring constant, tip radius, and cantilever/tip materials will vary based on the sample under study, and several options should be tested.[84] In testing each cantilever, the drive amplitude and frequency should be systematically varied. It is generally recommended in the literature that the drive amplitude should be set as low as possible to ensure linear tip-sample contact.[126] Note that this value will be different for each type of cantilever. Single point frequency spectra can be used to identify the optimal drive amplitude for both the free cantilever and when in contact with the sample surface. To make direct comparisons, which is necessary for storage and loss moduli calculations, the same drive amplitude should be used for both the free cantilever and when in contact.

An additional factor to keep in mind when determining the drive amplitude is the sampling depth, which is further dependent on the applied load. When imaging a film, the sharpest contrast is obtained when the drive amplitude is approximately 0.5-2 times the thickness of the film. Depending on the sample and goals of the study, however, it could be useful to examine the measured amplitude and phase contrasts for different applied loads or drive amplitudes, thus different sampling depths. There will also be shifts in the contact RF for different applied loads, adding to the breadth of data that can be examined.[90, 123-128]

2.4.3 Instrument Details for FMM in the Agilent 5500. As an example of this optimization process, this section discusses the FMM setup for an Agilent 5500 microscope.[84] To carry out FMM in the instrument, a BNC cable must be connected from the phase output of the MAC Mode controller to the Aux in of the AFM controller. A second BNC cable needs to connect the amplitude output of the MAC Mode controller to the Aux port on the Head Electronics Box. For imaging, additional channels must be opened to collect the phase signal via the MAC controller (CSAFM/Aux BNC channel) and the amplitude signal via the Head Electronics Box (Aux HEB channel). Operating the system in contact mode, the spectra window can be opened to control the drive signal for oscillating the piezo block on which the cantilever is mounted (the standard tapping mode nosecone). The drive amplitude is controlled by entering a percentage that outputs a drive reference signal proportional to the range of +/- 10 V AC. For example, a 1% drive value yields a drive amplitude of 100 mV. In the literature, the drive amplitude is occasionally reported in terms of distance (e.g. 5 nm), which is known when the tube piezo is driven to

oscillate, enabling a conversion of voltage to nm via the z-sensitivity. However, since in the Agilent 5500 the shaker piezo is controlling the oscillations, the sensitivity is not known. In cases such as this, previous studies either simply report the drive amplitude in voltage (and the resulting measured amplitude in voltage), or report no value.

In the spectra control window, the frequency range and number of data points for a frequency spectrum can also be controlled. For the Agilent 5500, the photodetector's output response with the gain switches off has a bandwidth limit of ~200 kHz at 10 V. Alternatively, with the gain switches on, the bandwidth limit is ~910 kHz at 10 V. For imaging, the specified frequency and drive amplitude (in %) are applied.

2.4.4 Energy Storage and Loss Moduli. For an optimized FMMM set-up, quantitative measurements can yield mechanical values such as the dynamic energy storage (E_{stor}) and dynamic energy loss moduli (E_{loss}). This is done through measuring the resonance frequencies (f) and quality factors (Q) at a specific eigenmode (n) of the freely oscillating cantilever (f_f and Q_f), the cantilever in contact with a reference material (f_r and Q_r), and in contact with the sample (f_s and Q_s).[123-126, 128] For example, considering the first flexural eigenmode (n = 1), the free space damping of the cantilever (χ) is described in eq 2.11. Using the Kelvin-Voigt contact modification, the cantilever dynamics for the n^{th} flexural eigenmode is described in eq 2.12 with a complex normalized wavenumber, λ_n.

$$\chi = \frac{2\pi f_f}{Q_f} \tag{2.11}$$

$$\lambda_n L = a_n + ib_n \tag{2.12}$$

In eq 2.12 L is the cantilever length, and a_n and b_n are defined in eq 2.13 and eq 2.14, respectively. Eq 2.13 and eq 2.14 are written to express the values for the 1st eigenmode when the cantilever is in contact with the reference material.[126, 128]

$$a_r = x_n^o L \sqrt{\frac{f_r}{f_f}} \tag{2.13}$$

$$b_r = a_r \left[\frac{(2\pi f_r - \chi Q_r)}{8\pi f_r Q_r}\right] \tag{2.14}$$

The corresponding root ($x_n^o L$) for n = 1 is 1.8751 (see eq 2.10). The solved values of a_r and b_r can be used to calculate the complex normalized wavenumber, re-written as:

$$\lambda_r = \frac{1}{L}(a_r + ib_r) \tag{2.15}$$

Then, λ_r can be used in eq 2.15 to determine the normalized tip-sample contact stiffness (α_r) and damping coefficient (β_r) for the reference material. L_1 is the position of the AFM tip along the cantilever's length L (with $L' = L - L_1$), and α_r and β_r are the real and imaginary parts of eq 2.16, respectively.[124-126, 128]

$$\alpha_r + i\beta_r(\lambda_r L_1)^2 = \frac{(2/3)(\lambda_r L_1)^3[1+\cos\lambda_r L\cosh\lambda_r L]}{\left[\begin{array}{l}((\sin\lambda_r L_1\cos\lambda_r L_1 - \sin\lambda_r L_1\cosh\lambda_r L_1)(1+\cos\lambda_r L'\cosh\lambda_r L'))+\\((1-\cos\lambda_r L_1\cosh\lambda_r L_1)(\sin\lambda_r L'\cosh\lambda_r L' - \cos\lambda_r L'\sinh\lambda_r L'))\end{array}\right]} \tag{2.16}$$

For the sample, α_s and β_s can be similarly determined by substituting f_s for f_r and Q_s for Q_r in equations 2.13-2.16. Solving for these values for both a known reference material and the sample of interest takes advantage of a calibration approach, where the reduced storage modulus (E_{stor}^R, eq 2.17) and reduced loss modulus (E_{loss}^R, eq 2.18) can be calculated based on the known properties of the reference material ($E_{stor,r}$ and $E_{loss,r}$).

$$E_{stor}^R = E_{stor,r}\left(\frac{\alpha_s}{\alpha_r}\right)^{3/2} \tag{2.17}$$

$$E_{loss}^{R} = E_{loss,r}\left(\frac{f_s\beta_s}{f_r\beta_r}\right)^{3/2} \quad (2.18)$$

Finally, the sample $E_{stor,s}$ and $E_{loss,s}$ can be extracted from the reduced complex modulus, using the known values for the tip and assuming that the Poisson ratio (ν) is similar for the reference material and sample (eq 2.19).[124-126, 128]

$$E_{stor}^{R} + iE_{loss}^{R} = \left[\frac{(1-\nu^2)}{E_{stor,s}+iE_{loss,s}} + \frac{\left(1-\nu_{tip}^2\right)}{E_{tip}}\right]^{-1} \quad (2.19)$$

A note that these calculations are limited to single point measurements on the Agilent 5500. To quantitatively map energy dissipation (E_{diss}), a separate instrument with specific electronics would need to be used to continuously track shifts in the contact resonance frequency during imaging.[122] In Chapter IV, however, E_{diss} calculations are applied to acquired FMM images based on the amplitude and phase outputs, similar to calculations done for tapping mode measurements.[129-132]

2.5 Scattering-Type Scanning Nearfield Optical Microscopy

2.5.1 Introduction to Scattering-Type Scanning Nearfield Optical Microscopy. One of the fundamental limits of most AFM modes is that they are largely chemically insensitive. While through careful sample or tip preparation and appropriate imaging conditions meaningful conclusions can still be drawn regarding varying chemical species and physical properties, there is still a lack of definitive spectroscopic characterization. Two techniques that are seeking to overcome this by introducing optical elements to nanoscale AFM measurements are AFM-infrared spectroscopy (AFM-IR)[133] and scattering-type scanning nearfield optical microscopy (s-SNOM).[91, 92] An additional benefit of s-SNOM is that it is capable of characterizing plasmons, or the collective

excitations of electrons in conductors. In graphene, surface-plasmon polaritons (SPPs) are electromagnetic waves trapped at the conductor-dieletric interface due to the collective surface excitations of carriers. Imaging the interference patterns of these waves in s-SNOM provides a wealth of information, as the interference pattern is impacted by variables such the geometric shape and morphology of the graphene sheet and the local carrier density.[134]

Photon confinement is achieved in a tip-based s-SNOM method by the incident light field becoming enhanced around the apex of a metalized tip, taking advantage of the nanoscale lateral resolution of AFM.[92] Localized light scattering occurs with the electric field lines predominantly oriented in the z-direction (perpendicular to the tip apex), regardless of propagation and polarization directs of the incident light. Importantly, because the spatial resolution is limited by only the radius of curvature of the tip, this is currently the only option for optical microscopy that enables nanometer confinement for the long wavelength mid-infrared illumination (e.g. 10 μm) used for chemical analyses. While AFM-IR enables similar nanometer resolution for IR analyses, the operating principle differs by that AFM-IR uses an AFM probe to locally detect the thermal expansion of a sample in response to far field IR illumination.[133]

2.5.2 Signal Detection in s-SNOM. The signal path in s-SNOM for the incident and detected electromagnetic field is shown in Figure 2.7. The incident field is focused to a metalized AFM probe. In the Materials Characterization Facility at Texas A&M University, the nanoIR2-s (Anasys Instruments)[135, 136] uses a 10.5 μm wavelength CO_2 laser and a platinum coated tip. When this farfield (E_b) signal reaches the tip apex, the

AFM tip confines the electromagnetic field, acting as a "new source" of light. This nearfield (E_{NF}) extends about one tip radius of curvature (R_{tip}) in all directions.[92] The detector then receives scattered light from both the farfield background (E_b) and the nearfield (E_{NF}). Note that the intensity of the background signal is proportional to the area illuminated and is much stronger than the nearfield signal, or $E_b >> E_{NF}$.

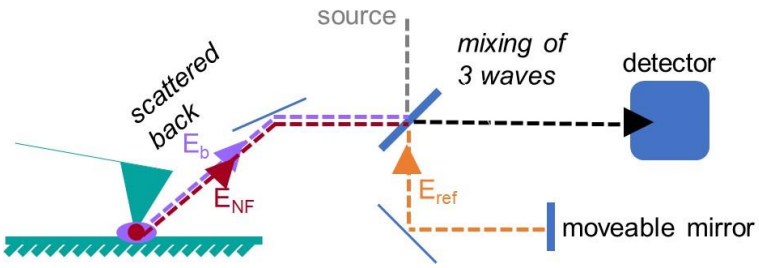

Figure 2. 7. Schematic of signal path for s-SNOM.

The use of lock-in amplifiers allows for the isolation of the weak, periodic nearfield signal over the strong, noisy background. To make this possible, signal modulation is implemented. Single modulation is achieved using tapping mode AFM to modulate E_{NF}.[137-139] The nanoIR2-s uses an additional modulation scheme to enable double modulation/demodulation for separating the nearfield signal from the scattered farfield. This second modulation generates a reference signal (E_{ref}) via a moveable mirror. The total signal intensity (I) is then proportional to the square of the sum of the amplitudes[140] from the combined electromagnetic waves of E_b, E_{NF}, and E_{ref} (eq 2.20):

$$I = \left(E_b + E_{NF} + E_{ref}\right)^2 \tag{2.20}$$

Which, squared, yields individual terms including:

$$I = E_b^2 + E_{NF}^2 + E_{ref}^2 + E_b E_{NF} + E_{ref} E_b + E_{NF} E_{ref} \ldots \quad (2.21)$$

The modulation is successful in separating E_b and E_{NF} primarily because the scattering of the farfield signal is elastic, while for the nearfield signal there is a non-linear increase in the signal amplitude at small tip-sample distances (on the order of the tip width, or twice R_{tip}).[92] This effect allows the alternating contact in tapping mode to induce higher harmonic modulations in the scattering signal. Therefore filtering at higher harmonics (n = 2 or 3 for nΩ, where Ω is the resonance frequency for tapping) produces an undisturbed nearfield image, recorded with full suppression of E_b. The final predominate signal is thus (eq 2.22):

$$I = E_{ref} E_{NF} \quad (2.22)$$

With all parameters of the reference signal known (amplitude, time, angular frequency, and phase), E_{NF} can be isolated.[92, 134-139, 141]

CHAPTER III

ADHESION AND FRICTION AT GRAPHENE/SELF-ASSEMBLED MONOLAYER INTERFACES INVESTIGATED BY ATOMIC FORCE MICROSCOPY[2]

3.1 Introduction

As a two-dimensional (2D) boundary lubricant, graphene has been shown to exhibit exceptional mechanical strength and friction reducing capabilities.[16, 24] A challenge in taking advantage of these promising properties is the difficulty associated with predictably controlling its frictional response, as when graphene is trapped between the nanoscaled asperity-asperity contacts that are ubiquitous in most machined interfaces. The resulting mechanical behavior depends very strongly on the competing chemical interactions at the contacting interfaces of the substrate[19, 39, 46] and top contact.[42-44] For example, in atomic force microscopy (AFM) measurements, where the tip models a single nanoscopic asperity,[33] Egberts *et al* demonstrated how hysteresis in the friction vs load response of graphene depended on maintaining continuous contact during scanning.[42] Liu *et al* further reported that variations in pull-off force measurements of graphene depended on presliding conditions.[43] The nanomechanical behavior of graphene in both of these studies was affected by variations in the contact area as the graphene "pucker" (out-of-plane deformation)[39] in front of the AFM probe changed with the amount of sliding and tip-graphene interaction strength. In another study by Deng *et al*, the tip-sample interaction

[2] Reprinted with permission from Elinski, M. B.; Menard, B. D.; Liu, Z.; Batteas, J. D. *J. Phys. Chem. C*, **2017**, *121*, 5635-5641. Copyright 2017 American Chemical Society.

strength was modified through the oxidation of graphite. This resulted in a negative coefficient of friction during the decreasing load portion of friction vs load measurements, due to the enhanced tip-sample adhesion locally delaminating the topmost layers of graphite.[44] Thus, precise control of the local adhesion is necessary for reliable friction response in graphene.

There has been significant prior work on the use of self-assembled monolayers (SAMs) to control the chemical composition, surface energies, and adhesion at interfaces. As such, one way to modulate the interactions between graphene and the sliding interfaces it contacts could be through the use of SAMs to tune the surface chemistry.[59] From a nanomechanics standpoint, however, this makes the frictional response dependent not only on the graphene/SAM adhesion, but also on factors such as the packing density and rigidity of the SAMs, as gauche defects and chain tilts induced during sliding are known to influence the shear strain and hence the resulting friction.[61] In fact, increased shear strain was seen in a previous study where graphene deposited on a SAM-modified rough silicon surface exhibited a pronounced layer-dependent frictional response due to the added compressibility of the underlying SAM.[34] Thus, synergistic effects can be seen which could provide additional routes to tuning surface friction using graphene/SAM (G-SAM) composite films. However, in order to implement SAMs as a means to modify the adhesive and frictional properties of graphene, there needs to be a detailed understanding of graphene-SAM interactions.

To investigate the G-SAM interface, the work here controlled the chemical interactions between the top sliding contact and graphene with a selection of SAM

functionalities.[142] AFM tips were functionalized with -NH_2, -CH_3, and -phenyl terminated silane based SAMs to explore hydrophilic, hydrophobic, and aromatic interactions with graphene. Thermal gravimetric analysis (TGA) was used to ascertain the molecular densities of the SAMs, and AFM pull-off force measurements with the functionalized probes were used to measure the graphene-molecule work of adhesion. Interaction energies were calculated from the measured work of adhesion values and the molecular packing densities. Corresponding FFM measurements were used to evaluate the impact of the different SAMs on the layer-dependent and load-dependent frictional responses of graphene. To assess competing contributions on the sliding G-SAM contact, the FFM results were analyzed with respect to a two-term friction law (eq 3.1) that combines Amonton's law and the single asperity friction law.[143]

$$F_f = \tau A + \mu L \tag{3.1}$$

In eq 3.1, Amonton's law describes the relationship where the friction force (F_f) is proportional to the applied load (L) by the coefficient of friction (COF, μ), and the single asperity friction law describes where the F_f is proportional to the shear strain (τ) and contact area (A).[33, 35] That is, Amonton's law describes load-dependent frictional behavior while the single asperity friction law describes adhesion-controlled friction. The summation in eq 3.1 accounts for their coexisting in nanotribological systems. Here, the frictional response was found to depend on a balance of G-SAM adhesion and shear strain.

3.2 Experimental Methods

3.2.1 Substrate and Graphene Preparation. In this study, the nanomechanical properties of graphene deposited on 90 nm thick thermal oxide surfaces of SiO_2/Si(100)

were investigated. Prior to thermal oxidation, score cut Si(100) wafers (Virginia Semiconductor) were cleaned with a base piranha solution of 4:1:1 (v/v/v) ratio of nanopore H_2O (18.2 MΩ cm, Barnstead), concentrated NH_4OH, and H_2O_2 (30%) at 85 °C for 20 min. The wafers were then rinsed with nanopore water and ethanol and dried with streaming N_2. The cleaned Si(100) wafers were thermally oxidized in a kiln at 1050 °C for 90 min to prepare the SiO_2/Si(100) thermal oxide films. The SiO_2/Si(100) surfaces were treated with UV/ozone to remove hydrocarbon contaminants before graphene transfer. Graphene samples were deposited through a water-soluble tape exfoliation method.[34] This is a modified Scotch tape method,[144] where regions of single and multilayer graphene are formed on the surface by re-exfoliating graphite that was transferred from bulk graphite (HOPG, K-Tek Nanotechnology) to the substrate via water-soluble tape (3M).

3.2.2 Self-Assembled Monolayer (SAM) Preparation. Silicon atomic force microscopy (AFM) tips (Mikromasch CSC37) were functionalized via self-assembly with silanes to investigate the molecular interactions between graphene and the top-contact of a sliding interface. The chemically modified AFM tips were prepared using each of the following molecules to represent hydrophilic, hydrophobic, and aromatic interactions, respectively: 3-aminopropyltriethoxysilane (APTES, Gelest), octadecyltrichlorosilane (OTS, Gelest), and phenethyltrichlorosilane (PETS, Sigma-Aldrich). The AFM tips were functionalized by first cleaning and hydroxylating the surface in base piranha solution (at room temperature for 1 min). The tips were then rinsed via immersion in water, ethanol, and toluene. Self-assembly was carried out by submerging the tips in 1 mM solutions (15

mL) of APTES, OTS, or PETS in toluene for 5 min. After functionalization the tips were again rinsed via immersion in fresh toluene and then ethanol.

Silicon nanoparticles (NPs) were also functionalized with each SAM to model the molecular coverage of the functionalized AFM tips. SiO_2 NPs (12 nm, Sigma-Aldrich) were prepared for functionalization by sonication in base piranha solution followed by centrifugation to recollect the NPs. The supernatant was removed, and the NPs were washed with water by repeating the sonication/centrifugation cycle, followed by subsequent washes of ethanol and toluene. The NPs were then dried under N_2 for 48 h. Once the NPs were dried they were functionalized with 1 mM solutions of APTES, OTS, or PETS in toluene (15 mg of NPs in 15 mL of solution), sonicated for 90 min, and allowed to react for 48 h. The functionalized NPs were then washed with sonication/centrifugation cycles of fresh toluene and then ethanol and again dried under N_2. Note that the longer reaction time in comparison to the AFM tips was chosen to account for the areal density of the surface sites on the AFM cantilever-tip assembly vs the total surface area of the NPs. To compare, the AFM tips were also functionalized for 48 h, and no difference in adhesion was observed from the tips functionalized for 5 min.

3.2.3 Fourier Transform Infrared (FTIR) Spectroscopy. Transmission FTIR spectroscopy was used to characterize the functionalized NPs, which again, we are using as an approach to evaluate the representative SAM order on the AFM tips.[62] Samples were prepared as a mixture of ~1 mg functionalized NPs in ~99 mg KBr powder. Spectra were collected with a Thermo Nicolet 6700 FTIR using a liquid-nitrogen-cooled detector (HgCdTe), averaging 256 scans with a 1 cm^{-1} resolution.

3.2.4 Thermal Gravimetric Analysis (TGA). TGA was used to calculate the molecular density of the SAMs on the functionalized NPs to model the coverage of the functionalized AFM tips (Metler-Toledo TGA/DSC 3+, at Veritas Testing and Consulting, LLC in Argyle, TX). To obtain an average monolayer density, three sets of functionalized NPs for each molecule were prepared. Samples were heated under a nitrogen environment with an initial 20 min isotherm at 100 °C to remove water. The temperature was increased 10 °C/min up to 850 °C, switching to an oxygen environment at 650 °C to ensure the complete removal of carbon.

3.2.5 Raman Microspectroscopy. Raman microspectroscopy was implemented to identify graphene layer thickness.[56] A WiTec Alpha 300R (Germany) confocal microscope was used with an Acton triple grating spectrometer interfaced with an Andor Peltier cooled (-65 °C) CCD detector. A 488 nm Ar ion laser was focused to a spot size of ~300 nm with a Nikon high numerical aperture objective (100x, 0.9 NA). The laser power used was <1.5 mW, and spectra were collected with a resolution of ~3 cm^{-1}.

3.2.6 Atomic Force Microscopy (AFM). Imaging, pull-off force measurements, and friction force measurements were taken in a dry nitrogen environment (relative humidity <0.1%) with an Agilent 5500. Data analysis was completed in the software program Scanning Probe Image Processing (SPIP). Silicon tips (Mikromasch CSC37) were used with normal spring constants of ca. 0.1-0.3 N/m and radii of ca. 10-20 nm (spring constants determined in situ by the Sader method,[114] and radii determined experimentally by the blind tip reconstruction feature of SPIP). For the friction force

measurements, the lateral force conversion was determined by the corrected direct force balance method.[100]

Tip-sample adhesion was calculated as the pull-off force from force-distance spectroscopy measurements. Force-distance (FD) curves were collected with a maximum applied load of 10 nN and an approach and retract rate of 1 μm/s. Force-volume mapping with a 16 x 16 point grid was used to collect FD curves over a 250 nm^2 area for each surface (single layer, bilayer, and bulk graphite). The force-volume mapping was done before and after the friction force measurements (total of 512 FD curves) to confirm that no changes to the tip occurred. Friction force vs load measurements were taken using a script to ramp the applied load during imaging. Over a 250 nm^2 area with a 256 pt/ln scan resolution the load was increased from 1 to 10 nN, with the tip being temporarily brought out of contact with the surface in between the loading and unloading cycle. Each loading and u n loading cycle was measured three times for each of the measured areas.

3.3 Results and Discussion

3.3.1 Self-Assembled Monolayers on Nanoscopically Curved Surfaces. To understand the adhesive and frictional responses of G-SAM interfaces, it is necessary to first fully characterize the SAMs on nanoscopically curved surfaces such as the AFM tips used in this study. Nanoscopic surface curvatures radially confine the SAMs, decreasing the packing density and quality of the film structure, ultimately impacting their tribological performance.[60-62] Examining film quality through FTIR spectroscopy and packing density through thermal analysis will help understand the interactions between the SAMs and graphene and ascertain SAM contributions to the observed nanomechanical

behavior. To model the SAMs on the AFM tips, silica nanoparticles were functionalized and subsequently characterized with FTIR spectroscopy and thermal gravimetric analysis (TGA). In the FTIR data shown in Figure 3.1, the asymmetric (~2920 cm^{-1}) and symmetric (~2850 cm^{-1}) CH_2 stretches of the alkyl chains were present for all three SAMs. Monitoring shifts in the CH_2 asymmetric stretch has been shown to indicate film order, with a frequency of ~2917 cm^{-1} for well-ordered films and a frequency of ~2924 cm^{-1} for disordered films.[62]

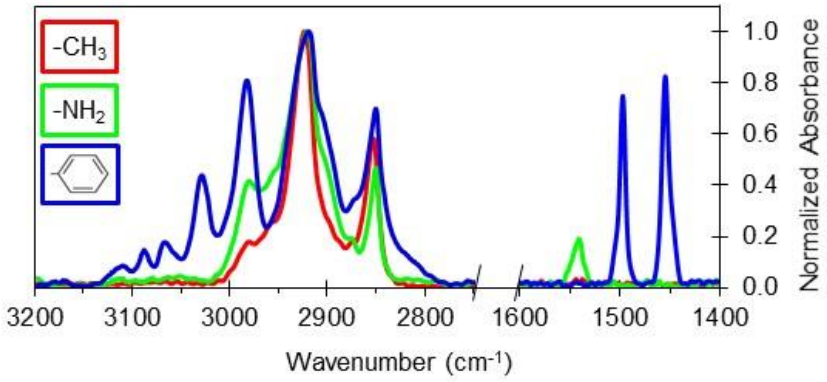

Figure 3. 1. FTIR spectra of the functionalized silica NPs, normalized to the asymmetric CH_2 stretch at ~2920 cm^{-1}.

In Figure 3.1, the spectra for APTES, OTS, and PETS have asymmetric stretch frequencies of ~2920 cm^{-1}, indicating moderately well-ordered films on the NPs. It is worth noting that for the shorter alkyl chain molecules (APTES and PETS) there is some peak broadening, which could indicate slightly ore disordered films. Additional characteristic peaks are the NH_2 scissor peak for the APTES SAM (~1540 cm^{-1}),[145] the

aromatic C-H stretches for the PETS SAM (~3026 cm^{-1}), and the double bond C=C stretches of the aromatic ring for the PETS SAM (~1490 cm^{-1}).[146]

The observed weight loss in TGA was used to calculate the molecular density on the silica surface.[60] Based on the surface silanol density (4-5 silanols/nm^2),[147] optimal alkylsilane packing on nominally flat surfaces is 4 molecules/nm^2, although typical packing densities have been observed at ~2-2.5 molecules/nm^2 and as low as 1.5 molecules/nm^2 for curved surfaces.[60] Here, assuming 4 OH groups/nm^2, the molecular packing densities for each SAM were determined to be 5.4 ± 0.5 molecules/nm^2 for APTES, 2.45 ± 0.04 molecules/nm^2 for OTS, and 2.4 ± 0.1 molecules/nm^2 for PETS. While the high coverage of the APTES is surprising at first, one must recall that it is possible for APTES to form bi- or multilayer structures, which would impact the estimated monolayer coverage.[148, 149] If, for instance, a bilayer is assumed to have formed the APTES molecular packing density would instead be 2.7 ± 0.5 molecules/nm^2, consistent with the measured monolayer coverages of the other silanes.

3.3.2 Graphene Characterization. The exfoliated graphene region shown in Figure 3.2 was examined through a combination of AFM and Raman microspectroscopy. Areas of single layer graphene (1LG), bilayer graphene (2LG), and few layer graphene (FLG) flakes on a nominally flat 90 nm SiO_2 substrate were located and characterized by optical microscopy (Figure 3.2a), Raman microspectroscopy (Figures 3.2b,d), and AFM (Figure 3.2c). A Raman map of the relative intensity of the characteristic *2D* and *G* peaks of graphene[56] (Figure 3.2b) shows the spatially resolved spectral identification of the graphene flakes seen in the AFM topography image (Figure 3.2c). Figure 3.2d shows the

corresponding single spectra data for the 1LG, 2LG, and FLG regions. Bulk graphite (HOPG) was imaged in a separate region on the same sample.

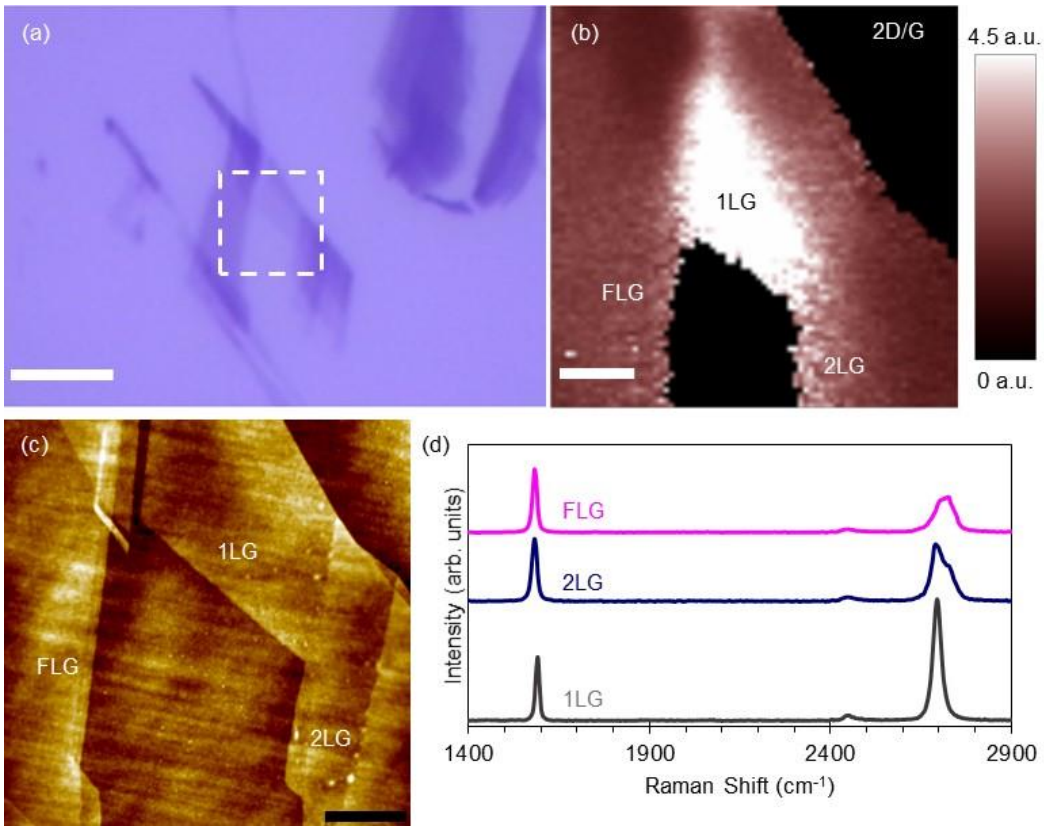

Figure 3. 2. (a) Optical microscopy image of the graphene region (scale bar = 5 μm). (b) Raman map (scale bar = 1 μm) of the white dashed region in (a), showing the *2D*/*G* intensity ratio with flakes labeled as 1LG for single layer graphene (white), 2LG for bilayer graphene (light maroon), and FLG for few layer graphene (maroon). (c) AFM contact mode topography image of the same region shown in (a) and (b), with the corresponding 1LG, 2LG, and FLG flakes labeled (scale bar = 1 μm). (d) Single Raman spectra taken at the labeled locations in (b).

3.3.3 Graphene-Molecule Interaction Strength. Quantitative insight into the parameters governing the frictional properties of the G-SAM composite interface requires

knowledge of the tip-sample adhesion. Here, chemical force spectroscopy was used to measure graphene-molecule adhesion. The measured adhesive forces (F_{adh}) and tip radii (R_{tip}) were used to calculate the graphene-molecule work of adhesion (w) (mJ/m^2, or mN/m). To compare using the Johnson-Kendall-Roberts (JKR)[119] vs the Derjaguin-Muller-Toporov (DMT)[118] contact mechanics models the transition parameter λ (eq 3.2) was calculated, related to the Tabor transition parameter (μ_T) by $\lambda = 1.157\ \mu_T$.[116]

$$\lambda = 1.157 \left(\frac{16R_{tip}w^2}{9K^2z_0^3}\right)^{1/3} \quad (3.2)$$

K is the reduced modulus of the contact, calculated using the Young's modulus (YM) and Poisson ratio (ν) of SiO_2 (YM: 73 GPa; ν: 0.17) and graphene (YM: 1 TPa; ν: 0.16).[15, 147] The equilibrium separation of the surfaces, z_0, is assumed to be 2 Å, which represents the van der Waals packing radii of most atoms and small molecules.[150] For $\lambda < 0.1$ the DMT model applies, for $\lambda > 5$ the JKR model applies, and for $0.1 < \lambda < 5$ the interfacial behavior is in the transition regime. The calculated values were 0.12, 0.20, 0.26, and 0.31 for the -OH, -NH_2, -CH_3, and -phenyl tips, respectively. While the transition parameters indicate the G-SAM interfaces fall in the DMT-JKR transition regime, the JKR model (eq 3.3) was chosen to account for compression of the SAMs within the contact, as the DMT model is really more applicable to ideally hard interfaces.[116]

$$w_{JKR} = \frac{2F_{adh}}{3\pi R_{tip}} \quad (3.3)$$

Representative histograms of work of adhesion values taken on 1LG are plotted in Figure 3.3a to examine the distribution in the different functional group-graphene interactions (work of adhesion values for 2LG and HOPG were within one standard

deviation of the 1LG values). The data for each tip functionality are fitted with a Gaussian distribution, with the fitted values reported in Figure 3.3a.

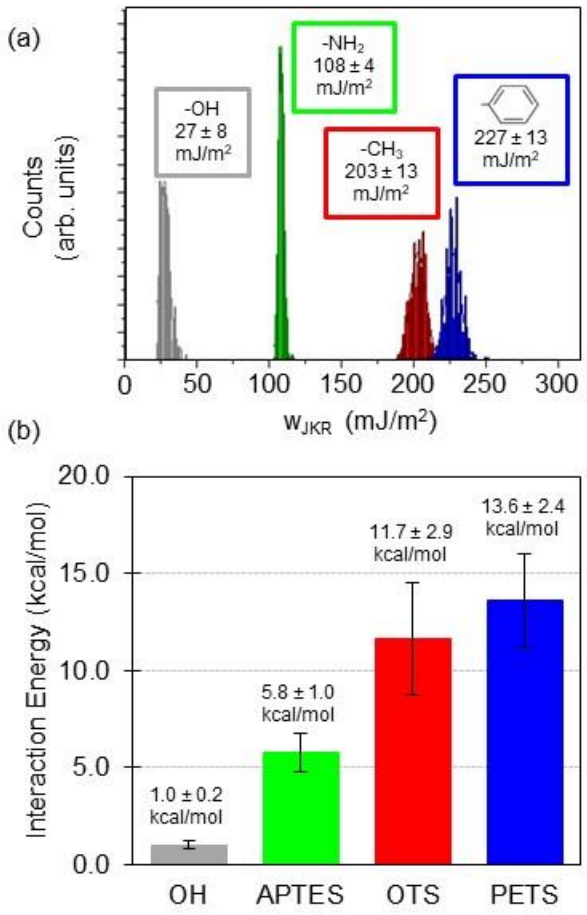

Figure 3. 3. (a) Representative histograms for each tip functionality showing the distributions in work of adhesion values for 1LG using the JKR model. Results of the Gaussian fit for each functional group are shown. (b) Corresponding interaction energies for each functional group with 1LG, calculated from the work of adhesion data in (a) and the molecular densities obtained from TGA.

Other studies with unfunctionalized AFM tips looking at pull-off forces of 1LG have reported work of adhesion values ranging from 7 to 340 mJ/m^2.[40, 43, 45, 47] The broad

range of the reported literature values is likely due to variations in experimental conditions (i.e., differences in tip material, or vacuum vs nitrogen environments) and methods of analysis (i.e., contact mechanics theories). A separate study using an OTS functionalized AFM tip found the tip-graphene work of adhesion to be ~7-10 mJ/m^2, although the experimental conditions (epitaxial graphene in a liquid environment) are not directly comparable to the work here.[151] Other measurements of graphene-substrate adhesion have been summarized by Bunch and Dunn[152] and range from 100 to 450 mJ/m^2 depending on the measurement method employed, as well as sample preparation and the extent of hydroxylation of the SiO_2 surface.[153-155] The -OH tip/1LG work of adhesion value measured under the experimental conditions here (27 ± 8 mJ/m^2) lies toward the lower end of the literature range and serves as an internal reference for the functionalized AFM tips.

To further compare interaction energies, the molecular densities obtained from the TGA measurements were used in conjunction with the work of adhesion data to calculate the interaction energies in kcal/mol (E_{JKR}) for each graphene-molecule pair (Figure 3.3b) For the -phenyl/1LG interaction energy, previous experimental work with benzene/graphite[156] and previous computational work for benzene/graphene[157] both found an interaction energy of 13.6 kcal/ mol, which is consistent with the energy (E_{JKR}) value calculated here.

The graphene-molecule interaction energies have the same relative order as the work of adhesion data, where the hydrophobic and aromatic functional groups have the strongest interactions with graphene. In order of increasing interaction strength with 1LG,

the functional group trend is -OH < -NH_2 < -CH_3 < -phenyl. This trend can be explained by the different intermolecular interactions, specifically van der Waals (vdW) forces and pi-pi interactions. For vdW forces, there are three components contributing to the total vdW interaction; these are the Keesom-orientation, Debye-induction, and London-dispersion. The dominant contribution is generally from dispersion forces, or induced-dipole forces. The data here reflect that the interaction energies increase for functional groups with decreased dipole moments and increased polarizabilities, or in other words they have stronger contributions from dispersion forces (high polarizability and weak dipole moment).[150] Other intermolecular interactions to consider are hydrogen-bonding, electrostatic, and pi-pi interactions. It is not expected that hydrogen-bonding is occurring in the case of the -OH or -NH_2 functionalized tips because the graphene sheet will prevent direct interactions with the underlying SiO_2 surface. It is also not expected that electrostatic interactions are influencing the adhesion measurements for the -OH and -NH_2 functionalized tips because different charge states would be manifested as additional distributions in the work of adhesion histograms.[158] In the case of the -phenyl tip, however, it is assumed that pi-interactions are responsible for further increasing tip-graphene interaction strength.

3.3.4 Frictional Properties of the Graphene-SAM Sliding Interface. Friction force (F_f) measurements were performed using the same functionalized AFM tips as in the adhesion studies to assess the impact of tailoring graphene-substrate interaction strength on the frictional response of the G-SAM sliding interface. Figure 3.4 shows the representative friction force (F_f) for each AFM tip/graphene layer combination at a

constant applied load of 5 nN. The F_f values are additionally normalized by the individual tip radius of curvature (R_{tip}).

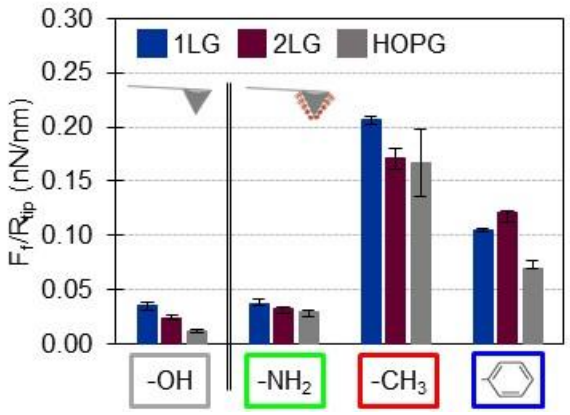

Figure 3. 4. Representative friction force (F_f) data, normalized to the tip radius of curvature (R_{tip}), at a 5 nN applied load. The bar plot compares different graphene layer thicknesses (1LG, 2LG, and HOPG) for each tip functionality (as indicated below the x-axis).

From Figure 3.4, it can be seen that the -OH, $-NH_2$, and $-CH_3$ tips exhibit the typical layer-dependence, where the F_f increases as the number of graphene layers decreases. While it appears that with the -phenyl tip the F_f of 2LG is higher than 1LG, this difference was generally found to be close to the margin of error of the measurement. Further evaluating the data presented in Figure 3.4, the relative magnitude of the F_f/R_{tip} values do not correlate directly with the relative order of increasing tip-sample adhesion for the functional groups. Notably, while the -phenyl tip showed the highest adhesion, the $-CH_3$ tip exhibits the largest frictional response. We can understand these trends when

considering the underlying mechanisms influencing the associated changes in both contact area and shear strain of the contact.

First, considering the contact area, there are two possible ways by which the contact can be altered, other than by simply the tip radius. Increasing tip-sample adhesion increases the contact area according to the JKR contact theory. Another means by which the contact area could be increased for this system is that increased tip-sample adhesion could induce more local puckering by the graphene sheet around the tip. Second, there are also two possible mechanism that could impact the shear strain of the interface. The SAM packing density influences the number of defects within the monolayer and depends on variables such as chain length and degree of substrate attachment, which in turn impacts the local shear strain based on molecular stiffness (with more densely packed films being more rigid than more defective films).[61, 159] The shear strain, however, would also vary in a concerted fashion with the extent of local graphene puckering under the tip.[46]

Measuring the load-dependent frictional behavior (Figure 3.5a) of the sliding interface allows for a more direct evaluation of frictional behavior by calculating the shear strain based on eq 3.1. Examining the resultant shear strain of the interface with respect to the graphene-molecule interaction strength and SAM chain length helps manifest the competition between the different mechanisms governing the total frictional response.

Calculating the COF (μ) as the slope of the F_f vs L data and using the JKR contact area (A), the two-term friction law (eq 3.1) was used to calculate the shear strain (τ) for each graphene-tip pair (plotted in Figure 3.5b). Considering these values with respect to chain length for each molecule and the relative work of adhesion values, the data suggests

that the shear strain is sensitive to both compression of the SAM and the possibility of increased graphene puckering induced by higher G-SAM interaction strength.

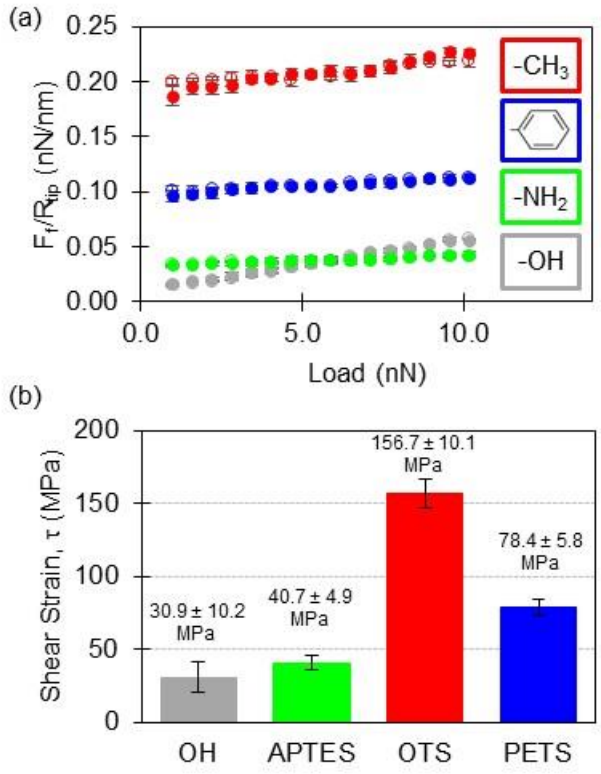

Figure 3. 5. (a) Friction force (normalized by tip radius) vs load data for each tip functionality on 1LG (filled circles = loading; unfilled circles = unloading). Note: normal loads represent the applied load without pull-off forces set to zero. (b) Calculated shear strain values at a 5 nN applied load.

The carbon chain lengths are C_2 for PETS (-phenyl), C_3 for APTES (-NH_2), and C_{18} for OTS (-CH_3). Typically, longer alkyl chains are more ordered (stabilized by vdW interactions), allowing for the formation of monolayers with fewer defects, offering reduced shear and frictional forces.[61, 159] This ordering, however, is disrupted by the

impact of nanoscopic surface curvature on substrate attachment.[60, 159] As evidence in the IR spectroscopy and TGA data, the different SAMs used here are similarly ordered and packed. Another consideration is, however, the compression of the SAM.[62] The -CH_3-graphene interface having the highest shear strain is likely due to the increased chain length allowing for greater compression compared to the shorter chain molecules.

Further, comparing the unfunctionalized -OH tip and the shorter alkyl chain of the -NH_2 tip, there is no difference in shear strain outside of the error bars, despite the increase in tip-sample work of adhesion. This supports the idea that the drastic increase in shear strain for the -CH_3 tip is due to the longer alkyl chain, not because of the higher work of adhesion. Conversely, for the -phenyl tip, it is likely the higher shear strain (relative to -OH and -NH_2) is instead due to increased graphene puckering in response to the highest work of adhesion and not due to increased shear from the carbon chain length (which is the shortest for the -phenyl SAM).

Previous friction vs load studies of graphite have shown hysteresis between the loading and unloading curves, attributed to locally delaminating the topmost layers of graphite under enhanced tip-sample adhesion.[44] Here, we did not observe any load-dependent friction hysteresis when examining the loading vs unloading data for each tip functionality/graphene layer pair. This may be a result of our measurement method for this, where the tip was briefly pulled out of contact with the surface while scanning to reset the load between the loading and unloading cycles. As can be seen in Figure 3.5a for the tip functionalities on 1LG, no hysteresis was observed in the friction measurements.

This was similar for the 2LG and HOPG cases as well, where hysteresis could potentially be seen, but it was within the error bars of the measurement.

3.4 Conclusions

The data here show that by controlling AFM probe chemistry with SAMs the graphene-tip interaction strength is tailored, with the highest G-SAM adhesion for the aromatic functional group. Tuning the strength of this interaction in turn modulates the frictional response of the sliding G-SAM interface by controlling the variables contributing to the two-term friction law. Mainly, the modulated frictional response of the G-SAM interface is a competition between graphene-molecule interaction strength and shear strain. The shear strain corresponded to the chain length of each SAM used, and caused the -CH_3/graphene contact to have the highest friction force. For the -OH, -NH_2, and -phenyl tips that all had a lower measured shear strain, the friction force increased as tip-sample adhesion increased. Understanding the mechanisms governing the nanotribological properties of the G-SAM interface helps progress the molecular-scale control of the frictional response of two-dimensional materials.

CHAPTER IV

DYNAMIC MOTION AND ENERGY DISSIPATION IN GRAPHENE ON NANOSCOPICALLY ROUGH SURFACES

4.1 Introduction

One of the unique aspects of using two-dimensional (2D) materials as solid lubricants is their propensity to deform in the out-of-plane direction during sliding. In the case of a single asperity sliding on graphene supported on nominally flat surfaces, this out-of-plane flexibility results in the friction force increasing for thinner layers.[39] Recent simulations have determined that this effect is due to an evolving quality of the frictional contact during sliding, thanks to the high flexibility of graphene.[160, 161] In terms of developing advanced lubrication schemes, it would be advantageous to minimize this increase in friction force for thinner graphene layers. Both surface chemistry and substrate roughness offer ways to control the dynamic sliding motion of graphene by manipulating the morphology of graphene and shear strain of the sliding interface.[34, 64, 162] For achieving superlubricity, the out-of-plane flexibility of graphene enabled the formation of graphene nanoscrolls around nanodiamonds, yielding a highly lubricating composite system.[24] From these studies, it is evident that the dynamic out-of-plane motion of graphene plays a critical role in the tribological properties of graphene. However, these works have largely focused on explaining the underlying physical phenomena behind how single layer graphene behaves, both in flat and nanoscopically rough interfaces.

Given the layered structure of 2D materials, it is also important to understand how, when confined on nanoscopic asperities, the out-of-plane motion, interactions, and interlayer coupling influence the tribological behavior of few layer graphene (FLG). Work by Gao *et al*[163] found that the mechanical stiffness of layers of graphene is impacted by the amount of water intercalated between layers and the degree of interlayer coupling. Regarding out-of-plane energy dissipation, Lee *et al*[164] demonstrated how the frictional response of 1-2 layer graphene was impacted by intercalated H_2O vs D_2O. This difference in friction was attributed to how H_2O vs D_2O differed in their abilities to facilitate out-of-plane phonon coupling to the supporting substrate, thus modulating the out-of-plane energy dissipation.[164]

The work here focuses on how the dynamic motion and energy dissipation in graphene impacts its frictional response and how this is influenced by surface roughness. To first gain an understanding of the out-of-plane motion and mechanical behavior of force modulated studies, single layer graphene is investigated on a flat and nanoscopically rough surfaces. Then, to explore the influence of surface roughness on the dynamic interlayer behavior of few layer graphene, force modulation studies are carried out on a FLG/nanoscopically rough interface. These studies aim to understand how nanoscopic surface roughness impacts the motion of graphene and how energy dissipation through few layer graphene modulates the frictional response.

4.2 Experimental Methods

4.2.1 Substrate and Graphene Preparation. Silica surfaces with controlled nanoscopic roughness were prepared via spincoating specific sizes of silica nanoparticles

(NPs) onto a cleaned Si(100) wafer (Virginia Semiconductor). Score cut Si(100) wafers were cleaned in base piranha solution at 85 °C for 20 min. The base piranha solution was made as a 4:1:1 (v/v/v) ratio of nanopure H_2O (18.2 MΩ cm, Barnstead), concentrated NH_4OH, and H_2O_2 (30%). Then, using the same procedure as in the work by Spear *et al*,[34] a 400 μL quantitiy of 6 wt% 50 nm diameter silica NPs was spincoated onto a given Si(100) wafer at 2000 rpm for 2 min. After spincoating NP films, the roughened substrates were annealed in a kiln at 500 °C for 5 h.

To compare the rough surfaces to nominally flat SiO_2 surfaces, Si(100) wafers were cut and cleaned in base piranha as in the procedure for preparing the NP films. Then in place of spincoating a solution of NPs onto the Si(100) surface, a 90 nm silicon dioxide (SiO_2) film was thermally oxidized in a kiln at 1050 °C for 90 min.

A water-soluble tape exfoliation method[34] was used to transfer graphene to both flat and rough substrates. Surface contamination was removed from the silica surfaces (flat SiO_2 or NP films) through UV/ozone cleaning for 10 min, rinsing with nanopure H_2O, ethanol, and drying with streaming N_2. Bulk graphite (HOPG, K-Tek Nanotechnology) was transferred to the cleaned surfaces with water-soluble tape (3M). The tape was subsequently dissolved in nanopure water heated to ~85 °C, followed by gently rinsing the samples with nanopure water. After drying the samples with streaming N_2, single and multilayer graphene regions were exposed by re-exfoliating the transferred graphite with a new piece of water-soluble tape.

4.2.2 Raman Microspectroscopy. As in Chapter III, Raman microspectroscopy was used to confirm regions of single layer graphene (1LG).[56] Single point spectra (488 nm Ar

ion laser, laser power <1.5 mW, resolution ~3 cm^{-1}) were taken with a WiTec Alpha 300R (Germany) confocal microscope. The microscope was equipped with an Acton triple grating spectrometer interfaced with an Andor Peltier cooled (-65 °C) CCD detector. The laser was focused on the sample through a Nikon high numerical aperture objective (100x, 0.9 NA) to a spot size of ~300 nm.

4.2.3 Atomic Force Microscopy (AFM) and Force-Volume (FV) Mapping. Sample imaging and force-volume (FV) mapping, as discussed in Section 2.3, were performed using an Agilent 5500 in a dry nitrogen environment (relative humidity <0.1%) with diamond probes (single crystal diamond tip attached to a silicon cantilever, Diamond AFM Probe ART D10). No discernable tip wear (tip radius of curvature, R_{tip} ca. 20 nm) occurred during the measurements, confirmed experimentally before and after each data set by the blind tip reconstruction feature of the software program Scanning Probe Image Processing (SPIP). Cantilever spring constants (ca. 0.1 N/m) were determined in situ with the Sader method,[114] and detector sensitivity was determined against a flat SiO_2 countersurface.

FV analyses were performed on single layer graphene (1LG) on both flat SiO_2 and 50 nm NPs films, denoted as 1LG/SiO_2 and 1LG/50 nm NPs, respectively. Single FD curves (1,000 data points, 1 μm z-range) were acquired in a 32 x 32 point grid over a 300 nm^2 area to generate one FV map. Both the maximum applied load (10, 20, 30, 40, and 50 nN) and the approach/retract rates (0.5, 1.0, 1.5, 2.0, 2.5, 3.0, 3.5, 4.0, 4.5, and 5.0 μm/s) of the FD curves were varied to ascertain any impact on the out-of-plane fluctuations of graphene or the adhesion. Note that within a single FV map the maximum applied load

and approach/retract rates for each individual FD curve were held constant, so that these parameters were only compared across separate FV maps.

To visualize the out-of-plane fluctuations of graphene as driven by the FD curves, equal deflection images were extracted from the FV maps using SPIP. For a given FV map, this was done by first aligning all of the FD curves within the map by their baseline (setting the out of contact region to zero deflection) and by their snap-in height (setting the snap-in point to 0 nm z-position). This curve alignment defines any applied forces as positive, and defines any indentation into the surface as "negative" distances. Then a selected FD curve extracted from the FV map was used in defining the specific applied load points at which to extract a deflection image. In this manner, a series of deflection images can be extracted from one FV map focusing on the retraction of the tip. Compiling the series of deflection images can generate a stop-motion animation of the out-of-plane graphene fluctuations.

4.2.4 Force Modulation Microscopy (FMM). Force modulation microscopy (FMM) was implemented to evaluate the relationship between energy dissipation and friction at different tip oscillation frequencies. Both the flat and rough samples were analyzed to subsequently evaluate the impact of surface roughness and strain in graphene on this relationship. The same D10 single crystal diamond tips were used as for the FV mapping measurements. Frequency sweeps (0-200 kHz at 0.5 kHz resolution, at 0.1%, 1% and 2.5% drive amplitudes) of both the free cantilever and in contact with flat SiO_2 were taken to determine the resonance frequencies (RF) of the free cantilever and the coupled tip-sample contact for the first two flexural modes. The free RF of the 1^{st} flexural mode

was ~12 kHz, and the contact RF of the 1st flexural mode was ~50 kHz. These values are consistent with a previous FMM study of a self-assembled monolayer on mica using a cantilever of similar stiffness.[90] The free RF of the 2nd flexural mode was ~70 kHz, and the contact RF of the 2nd flexural mode was ~160 kHz. For these frequency curves, the effect of drive amplitude (in terms of % of the maximum possible applied voltage for the driving signal) was assessed to determine the range of linear tip-sample contact behavior during the oscillation cycles.

4.3 Results and Discussion

4.3.1 Graphene on Flat vs Nanoscopically Rough Surfaces. The exfoliated graphene samples on the flat SiO_2 and rough (50 nm silica NP film) surfaces were located and characterized with optical images, Raman microspectroscopy, and AFM contact mode topographic imaging. Figure 4.1a shows a confocal optical image of the exfoliated region on flat SiO_2, where the darker purple contrast represents thicker few layer graphene regions. From the exfoliation process, a combination of single layer graphene (1LG), bilayer graphene (2LG), and few layer graphene (FLG) flakes are randomly deposited on the surface. Figure 4.1b similarly shows an optical image of 1LG, 2LG, and FLG regions on the 50 nm NP surface. Figures 4.1c and 4.1d show AFM contact mode topography images of the regions in the white dashed boxes in Figures 4.1a and 4.1b, respectively. The asterisks in Figures 4.1c and 4.1d represent where a single Raman spectrum was taken to confirm 1LG for each sample. The spectra are overlaid in Figure 4.1e, normalized to the *G* mode. Consistent with the work discussed in Chapter I, the *G* and *2D* Raman modes

of 1LG/50 nm NPs are shifted to lower wavenumbers (relative to 1LG/SiO_2) due to the increased lattice strain over the nanoparticle apices.[162]

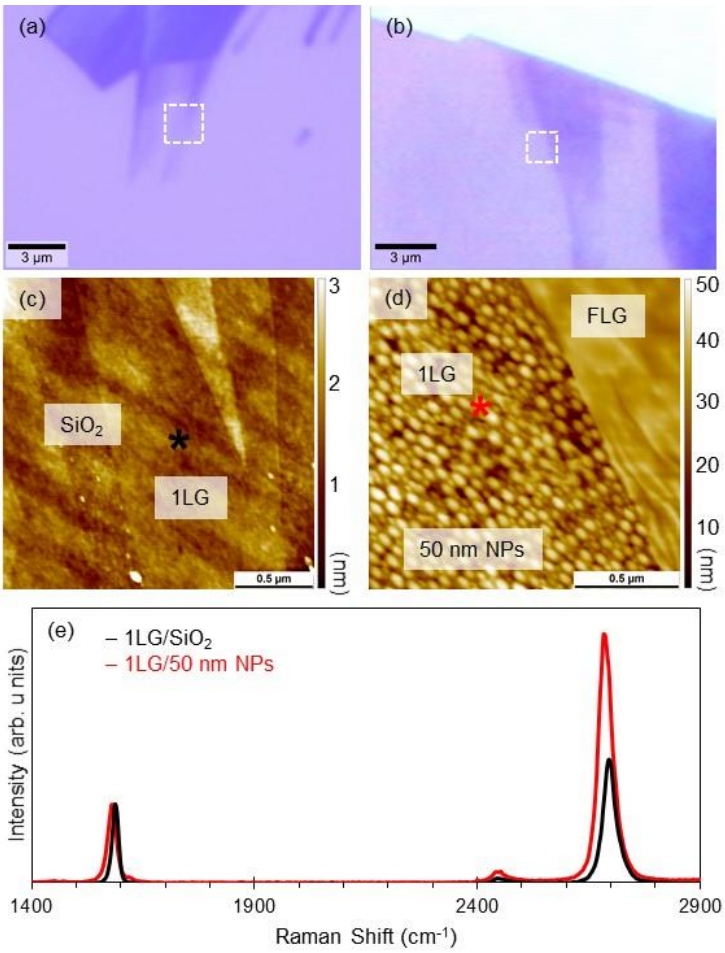

Figure 4. 1. (a) and (b) are optical confocal images of exfoliated graphene on flat SiO_2 and 50 nm NPs, respectively. The white dashed boxes in (a) and (b) highlight the areas where AFM measurements were taken. Contact mode topographic images at 1 nN load of 1LG/SiO_2 and 1LG/50 nm NPs are show in (c) and (d), respectively. The black (1LG/SiO_2) and red (1LG/50 nm NPs) asterisks in (c) and (d) show the location of the single Raman spectra taken to identify 1LG on each surface. These spectra are overlaid in (e).

4.3.2 Force-Volume Mapping: Visualizing Graphene Motion. The frictional response of graphene is sensitive to both the relative adhesion to the top or bottom contacting surfaces (discussed in Chapter III) as well as the out-of-plane deformation (discussed in Chapter I). Force-volume (FV) mapping can provide insight into how the spatial variations in adhesion and the extent of localized out-of-plane fluctuations of graphene might vary on rough surfaces. In the FV maps taken on 1LG/SiO_2 as described in Section 4.2.3, no spatial variation in adhesion (measured as the pull-off force) was observed for any parameter combination. Moreover, there was no change in the magnitude of the adhesion force regardless of the FD curve approach/retract rate or maximum applied load. This was also the case for the 1LG/50 nm NPs sample, where no shift in the magnitude of adhesion forces was observed for any combination of approach/retract rate or maximum load. This lack of dependence on FD curve rates is consistent with work by Deng *et al*, where no change in adhesion on suspended graphene membranes was observed for different rates.[45] However, spatial variations in the maximum pull-off force (adhesion) were observed for 1LG over the NP asperities. This is shown in Figure 4.2a, where variations in the adhesion can be seen that faintly resemble the underlying NP morphology. To ascertain if the spatial variations were indicative of changes in partially suspended graphene between the NP apices vs supported graphene, a histogram showing the distribution of adhesive forces is shown in Figure 4.2b. The even spread of adhesive forces suggests that there are no distinct distributions of adhesion for partially suspended vs supported graphene. The spatial variations are then likely dominated by gradual changes in the tip-sample contact area over the varied morphology.

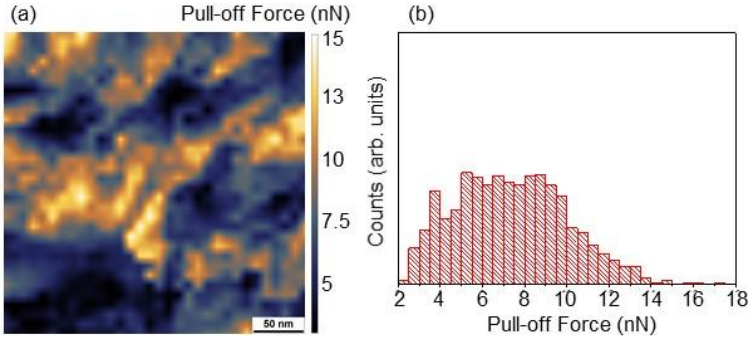

Figure 4. 2. (a) Adhesion map, measured as the pull-off force, of 1LG over 50 nm NPs (300 x 300 nm area, maximum applied load of 30 nN, approach/retract of 1 μm/s). (b) Histogram (bin size: 0.5 nN) showing the corresponding distribution of adhesion pull-off force values of the FV map taken in (a).

The FV maps were also used to evaluate the out-of-plane fluctuations of the partially suspended graphene over the 50 nm NP asperities. This was done by examining a series of equal deflection images at specified loads, as described in Section 4.2.3. The series of deflection images (displayed in a 3D view) are shown sequentially in Figure 4.3, starting at a high applied load and following the motion as the load is decreased during the FD retract curve. Comparing Figure 4.3a (large compressive load) vs Figure 4.3l (negative load, near the maximum pull-off force), the deflections appear inverted. This suggests that the regions of partially suspended graphene in Figure 4.3a in between the NP apices are then pulled upward by the tip in Figure 4.3l, while the regions of graphene supported by the NPs remain "pinned" to the NP apices. In the remaining series of images (Figure 4.3b-k), this transition from compressed to pulled graphene can be observed, including in Figure 4.3i, where at no load (0 nN), the deflection morphology appears overall smooth and level compared to the other images.

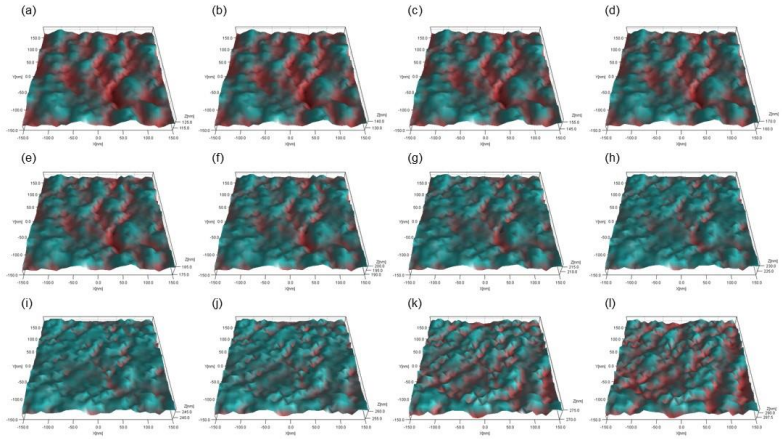

Figure 4. 3. Series of equal deflection images for a FV map taken on 1LG/50 nm NPs with a maximum applied load of 30 nN and approach/retract rate of 5 μm/s. The images in (a-l) show the deflection from the retract curves at applied loads in increments of 2 nN from 16 nN (a) to -6 nN (l).

For any parameter combination (varied approach/retract rates and maximum indentation loads), there was no observed influence on the degree of out-of-plane motion. Also, the deflection images for the flat 1LG/SiO_2 sample are not shown, as no changes in the deflection morphology were observed for any specified load point. The FV maps help conceptualize the dynamic tip-sample graphene motion, but do not measure lateral forces, as the tip is fully withdrawn from the sample in between each FD curve. Therefore the next section focuses on force modulation microscopy (FMM) as a means to evaluate the friction force while modulating the normal (out-of-plane) tip-sample force gradient.

4.3.3 Frequency Modulated Frictional Response of Graphene on Flat SiO_2. To evaluate the relationship between normal force modulation and lateral forces, force modulation microscopy (FMM) measurements were taken on the 1LG/SiO_2 sample. In FMM, the base of the cantilever is driven to oscillate at specified frequencies while in

sliding contact at a specified applied load. Drive frequencies were chosen to evaluate the frequency modulated frictional response both off and on tip-sample resonance frequencies (RF). The 1st and 2nd RF of the freely oscillating cantilever (f_f^1: 12 kHz and f_f^2: 70 kHz) and in contact with flat SiO_2 (f_c^1: 50 kHz and f_c^2: 160 kHz) are shown in Figure 4.4.

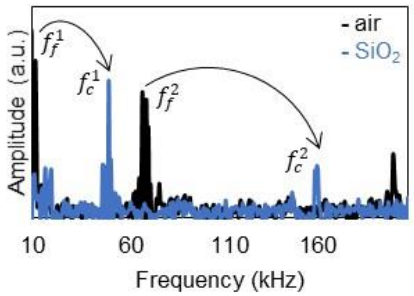

Figure 4. 4. Frequency curves taken from 0-200 kHz with 400 data points (0.5 kHz resolution). The black curve (air) shows the resonance frequencies (RF) of the 1st and 2nd flexural modes of the freely oscillating cantilever (12 kHz and 70 kHz, respectively). The blue curve (SiO_2) shows the RF of the 1st and 2nd flexural modes of the coupled tip-sample contact (taken with a 1 nN applied load on flat SiO_2).

The imaging frequencies were subsequently chosen to be 35, 50, 100, 160, and 175 kHz to assess frequencies below f_c^1, between f_c^1 and f_c^2, and above f_c^2.

The resulting friction force (F_f) images from the FMM measurements on the 1LG/SiO_2 sample (shown in Figure 4.1c) are presented in Figure 4.5, labeled according to their corresponding drive frequency. Each scan was taken at the same scan rate (1.25 ln/s) and applied load (1 nN), and each image is plotted on the same z-scale (F_f of 0-1.5 nN, shown as the color bar to the far right of the series of images).

To compare the relative magnitudes of the friction forces for each frequency, the average F_f for 1LG vs bare SiO_2 from each image in Figure 4.5 is plotted in Figure 4.6.

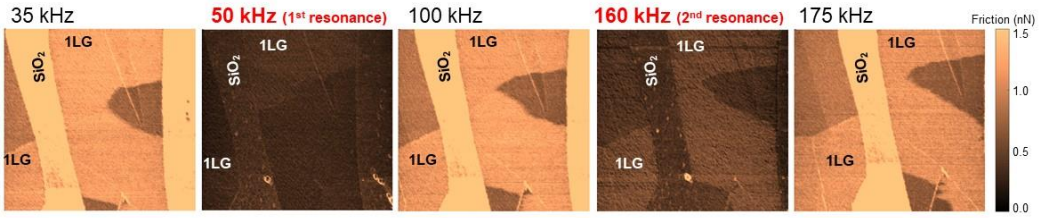

Figure 4. 5. Friction force images (2 x 2 μm) of the 1LG/SiO_2 sample for different drive frequencies (labeled above each image).

Based on the data in Figures 4.5 and 4.6, two dominate effects on the measured F_f can be seen for imaging on- vs off- the contact resonances. First, the overall magnitude of the F_f is greatly reduced for both 1LG and SiO_2 during on-resonance imaging. While the exact reason why this occurs is unclear, one possible explanation is that on-resonance there is a higher tip-sample amplitude that leads to a partial loss of tip-sample contact during the oscillation cycles. This "weakens" the tip-sample contact, resulting in a lowered measured F_f. This reasoning is based on previous FMM work that studied amplitude-induced lubricity on flat surfaces (silicon, mica, or polished glass).[165] In that study, imaging in contact mode at a constant frequency while gradually increasing the drive amplitude caused the measured F_f to lower, and ultimately vanish. The proposed mechanism was either the presence of a viscoelastic layer (since the study was done in an ambient environment, likely a water layer on the surface) or eventual partial loss of the tip-sample contact. In the study here, the drive amplitude is held constant and the drive

frequency is modulated, but imaging on-resonance induces larger tip-sample oscillation amplitudes than imaging off-resonance. Moreover, since the measurements here were carried out in a dry nitrogen environment, the likelihood of a viscoelastic water layer being present is dramatically reduced, suggesting the mechanism behind the lower F_f for imaging on-resonance is partial loss of the tip-sample contact.

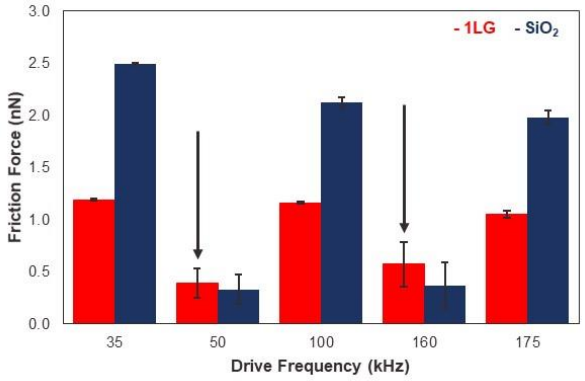

Figure 4. 6. Bar plot showing the average F_f of 1LG vs bare SiO_2 for each drive frequency. The arrows emphasize the anomalous effect where, on-resonance, the F_f of 1LG is slightly higher than the F_f of SiO_2.

The second F_f effect for imaging on- vs off- the contact resonances is that when imaging on-resonance, the measured F_f of 1LG is slightly higher than the F_f of SiO_2 (seen in the 50 and 160 kHz image contrast in Figure 4.5 and emphasized by the arrows in Figure 4.6). This an extremely unusual effect but is highly reproducible for these specific imaging conditions. The proposed reason for this F_f anomaly is based on the previously discussed possibility of partial tip-sample contact loss during the oscillation cycles. If this partial loss is occurring, the measured F_f for 1LG could be larger relative to SiO_2 because the

adhesion for 1LG (9.3 ± 0.2 nN) is higher than that of SiO_2 (8.4 ± 0.3 nN). The increased adhesion for 1LG could then slightly mitigate the loss of contact, resulting in a higher measured F_f. This is supported by testing other imaging conditions. If any parameter is changed that would cause lower tip-sample oscillation amplitudes, the F_f differences are reversed back to the usual case where the F_f of 1LG is less than that of SiO_2. The tested parameters that demonstrated this included higher applied load (15 nN vs 1 nN), lower drive amplitudes (reduced by half), or imaging slightly off-resonance (± 2 kHz).

These force modulation measurements on the flat 1LG/SiO_2 sample help identify some of the mechanical tip-sample interactions that might play a role in interpreting frequency dependent frictional responses. This provides a reference in moving forward to more complex tip-sample interactions on the nanoscopically rough surfaces.

4.3.4 Correlation of Energy Dissipation and Friction for Few Layer Graphene on a Nanoscopically Rough Surface. Nanoscopic surface roughness has a large influence on the frictional behavior of graphene.[34] Depending on the relative size of the NP asperities and the AFM tip, the degree of out-of-plane deformations of graphene can be tuned, providing morphological control over the frictional response. Nanoscopic asperities also induce localized regions of strain in the graphene lattice, centered on the top of the NP apex.[166] This localization of strain might influence the amount of energy that can be dissipated out-of-plane, providing another pathway to regulate friction. While these studies have focused on single layer graphene (1LG), the subsurface impact of nanoscopic roughness on the strain distribution and frictional behavior of few layer graphene (FLG) has yet to be explored. Thus, in this section FMM was used to evaluate how the out-of-

plane coupling in FLG is influenced by an underlying NP film, and how this coupling manifests as a correlation between energy dissipation and friction.

For the 1LG/50 nm NP sample described in Figure 4.1d, FMM measurements were carried out under the same imaging parameters as for the flat 1LG/SiO_2 sample (1 nN applied load, same drive amplitude, and same series of drive frequencies). Figure 4.7 shows the corresponding phase images. Similar to tapping mode, in FMM the phase shift between the drive signal and measured signal reflects how much energy is being dissipated for each oscillation cycle.[129-132] The regions with a brighter contrast, corresponding to a greater phase shift, generally represent regions of softer materials or lower modulus, where a greater amount of energy is being dissipated. Based on recent work by Vasic *et al*, tapping mode phase measurements demonstrated that 1LG dissipates less energy than bare SiO_2, acting as a mechanical shield.[167] Therefore it was expected that for 1LG and FLG over the NP asperities the phase shift would be less compared to the partially suspended regions between the NP apices. However, as can be seen in Figure 4.7, a more complicated result was observed. Particularly for the 1LG/50 nm NP region, the inverse of phase contrast between 35 kHz and 50 kHz, along with the varying contrasts for 100, 160, and 175 kHz, could be influenced by the NP morphology, but overall cannot be explained at this time.

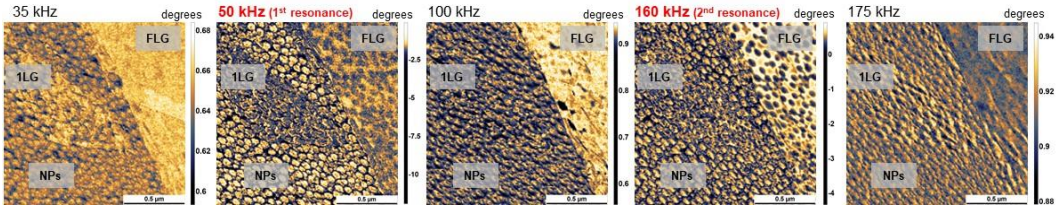

Figure 4. 7. FMM phase images for 1LG and FLG on 50 nm NPs at different drive frequencies (labeled above each image).

Focusing on the FLG/50 nm NP regions in Figure 4.7, though, appears to provide insight into different levels of subsurface contrast.[168] Recent work examining graphite flakes transferred to a textured polymer surface showed the capability of phase images from scanning on-resonance to identify subsurface features.[169] This is seen here, with the clearest subsurface NP features identified for the 2nd RF, 160 kHz. This FLG/50 nm NP region was used to establish a crude estimate regarding the conformity of the underlying FLG layers at the buried FLG/NP interface. Figure 4.8a shows the same topography image as Figure 4.1d, with an additional cross section (Figure 4.8b) to estimate the number of FLG layers. From a cross section height of ~5.8 nm, there are approximately 17 graphene layers (based on a height of 0.34 nm for a single layer[170]). For these 17 graphene layers, the 160 kHz phase image is reshown in Figure 4.8c, with the red dashed box highlighting where the 3D phase profile in Figure 4.8d was taken. Calculating a root mean square (RMS) roughness value for the buried FLG/50 nm NPs interface shown in Figure 4.8d yields a value of 0.334 degrees. To calibrate the z-scale for the subsurface features from degrees to nm, the ratio was taken of the RMS roughness of bare NPs in nm (18.94 nm, from the topography image) over the RMS roughness of bare NPs in degrees (0.473

degrees, from the phase image). This calibration provides a crude approximation that the RMS roughness of the buried FLG/NP interface is ~13.4 nm.

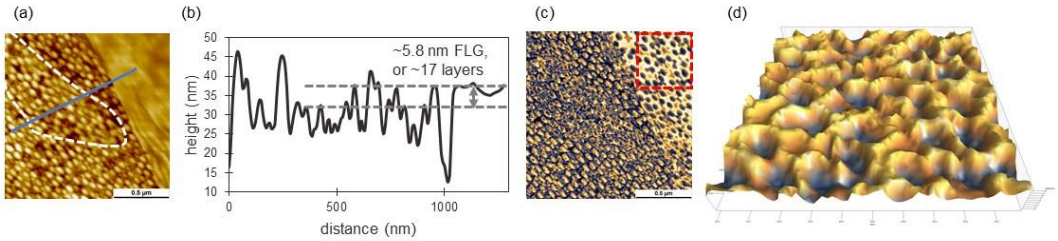

Figure 4. 8. (a) AFM topography image of single layer graphene (highlighted by the white dashed line) and few layer graphene (right portion of image) on a 50 nm NP film. The blue line shows the location for the corresponding cross section in (b). In (b), the dashed lines indicate the thickness of the few layer graphene (FLG) region (~5.8 nm, or 17 layers). (c) The FMM phase image taken with a drive frequency of 160 kHz (reshown from Figure 4.7). The dashed red box shows the zoomed region that is shown as a 3D projection in (d). (d) A 3D projection showing the "conformity" of the buried FLG/50 nm NP interface.

Comparing the roughness of this buried interface, ~13.4 nm, to that of the bare NPs, ~18.9 nm, indicates the bottom layers of the FLG region are only partially conformed to the NPs, similar to what is directly measured for 1LG/50 nm NPs. Further, compared to the RMS roughness of the top FLG surface, ~7.0 nm (measured directly from the topography image), it is likely that the morphology of the underlying NP film is gradually reduced through layers. These local changes in internal layer structure where regions of FLG directly over the NP apices vs the underlying "partially suspended" FLG layers might influence how energy is dissipated through interlayer coupling. This ultimately might be influencing the measured friction force, discussed next.

The friction force (F_f) images that were acquired simultaneously with the phase images in Figure 4.7 are shown in Figure 4.9. Similar to the FMM on the flat 1LG/SiO_2 sample, the overall F_f is reduced when imaging on-resonance. However, the F_f of 1LG always remains lower than that of the bare NPs. This difference between the flat and rough samples could be attributed to the surface roughness of the NP film influencing the tip-sample interactions.

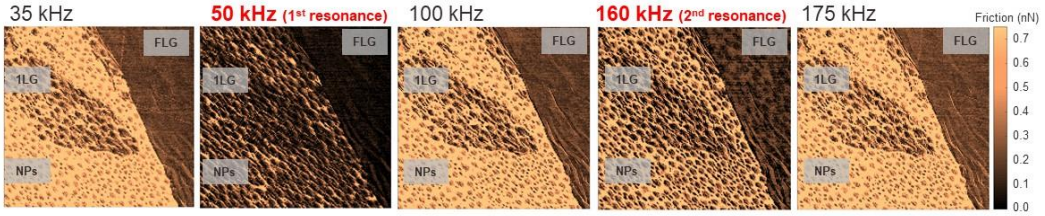

Figure 4. 9. Friction force images (1.5 x 1.5 µm) of the 1LG/50 nm NP sample for different drive frequencies (labeled above each image).

Of particular interest is the additional F_f contrast within the FLG region for a drive frequency of 160 kHz (the 2nd RF). Similar to the corresponding phase image, "subsurface" friction contrast is observed for the underlying NP film. This contrast is not seen for the other frequencies, and it is unclear why this effect is also only observed for the 2nd resonance, and not the 1st. While the contrast is dark for the 1st RF (50 kHz) in Figure 4.9 due to the lower F_f on-resonance when all of the friction images are displayed on the same F_f scale, when the FLG is inspected separately there is still no observed contrast from the underlying NP film.

One possible reason why the underlying NP film morphology is reflected in the F_f image of an otherwise uniform FLG surface is that more energy could be dissipated through out-of-plane, interlayer coupling for FLG that is partially suspended between the NPs, resulting in locally higher measured F_f. To quantify the amount of dissipated energy for a drive frequency of 160 kHz, the energy dissipation (E_{diss}) per cycle was calculated from the corresponding amplitude and phase images (eq 4.1).[171]

$$E_{diss} = \pi k_0 A_0 A \sin \varphi \tag{4.1}$$

In eq 4.1, k_0 is the spring constant of the freely oscillating cantilever, A_0 is the free amplitude, A is the measured tip-sample amplitude from imaging, and φ is the measured phase shift from imaging. Accounting for the number of oscillations per pixel (oscillation frequency of 160,000 oscillations/s at a scan speed of 1.25 lines/s with 256 pixels/line, yielding 500 oscillations/pixel) produces the E_{diss} map (converted to meV/oscillation) shown in Figure 4.10.

The FLG region in Figure 4.10 reflects the same subsurface NP contrast as discussed for the phase image (Figure 4.7) and friction image (Figure 4.9) for imaging with a drive frequency of 160 kHz. To compare the E_{diss} and F_f of the FLG/50 nm NP sample side-by-side, Figures 4.11a and 4.11b show 500 x 500 nm inspection boxes of the upper right region of FLG for E_{diss} and F_f, respectively. Figure 4.11c then shows a histogram of the distribution of E_{diss} values for the FLG region shown in Figure 4.11a. Similarly, Figure 4.11d shows a histogram of the distribution of F_f values for the FLG region shown in Figure 4.11b. To help guide the eye in comparing the two images in Figures 4.11a and 4.11b, the dashed white circle highlights the same region of FLG

supported directly over a NP apex, while the dashed blue circle highlights the same region of FLG partially "suspended" between NP apices. The distributions in Figures 4.11c and 4.11d are also labeled according to the local FLG subsurface structure, with Gaussian fits for the separate E_{diss} or F_f regimes.

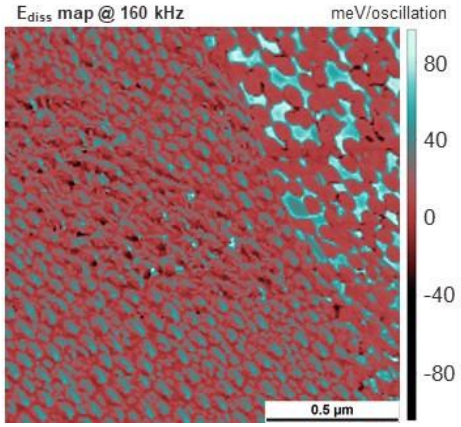

Figure 4. 10. Energy dissipation (E_{diss}) map for the 1LG/50 nm NP sample (including the FLG region) at a drive frequency of 160 kHz. The E_{diss}/oscillation is calculated based on eq 4.1 and additionally accounting for the number of oscillations per pixel.

As discussed previously, there is a potential correlation between the out-of-plane E_{diss} and measured F_f based on local internal variations induced by the subsurface NP morphology. Considering the localized regions of strain induced by the NP film for the buried FLG layers,[166] the lowest F_f is measured where the bottom layers of graphene are strained over the NP apices. This also corresponds to the regions of lowest E_{diss}, where the layers are "pinned," limiting the out-of-plane coupling.

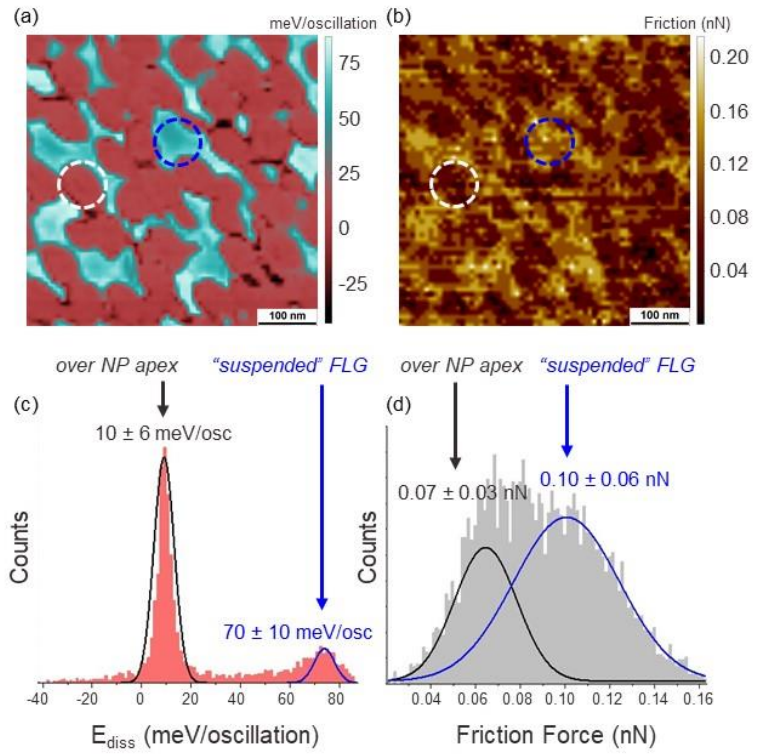

Figure 4. 11. (a) 500 x 500 nm inspection box of the E_{diss} map at 160 kHz from Figure 4.10, centered on the upper right FLG/50 nm NP region. (b) 500 x 500 nm inspection of the F_f image at 160 kHz from Figure 4.9, centered on the upper right FLG/50 nm NP region. (c) Histogram showing the distribution of E_{diss} values from (a). (d) Histogram showing the distribution of F_f values from (b). The dashed white circles in (a) and (b) highlight a region of FLG directly over a NP apex, corresponding to the distributions denoted by the black arrows in (c) and (d). The dashed blue circles in (a) and (b) highlight a region of FLG "suspended" between NP apices, corresponding to the distributions denoted by the blue arrows in (c) and (d).

Conversely, the regions of "suspended" FLG between NP apices have the least amount of strain, greatest E_{diss}, and highest F_f. This is consistent with previously established relationships between energy dissipation and friction, where greater energy dissipation at the sliding interface leads to greater friction forces.[35, 164] Another possible explanation, however, could be that the FLG regions that are partially suspended are compressed more

during the tip oscillation cycles than the regions supported by the NP apices, causing a locally larger contact area, thus higher F_f.[169]

4.4 Conclusions

This work was aimed at understanding the details of out-of-plane graphene motion, and the relationship between normal force modulation and lateral friction force for graphene on nanoscopically rough surfaces. Equal deflection images from FV mapping helped conceptualize the out-of-plane fluctuations of graphene partially suspended between nanoscopic asperities. FMM on flat 1LG/SiO_2 found that the frequency dependence of the F_f was largely dominated by changes in the mechanical interactions of the tip-sample contact. Moving to FMM on the 1LG/50 nm NP sample, the mechanical effects observed for the flat sample seemed to be largely impacted by the surface roughness. When focusing on the FLG/50 nm NP region, where interlayer, out-of-plane coupling is possible through the multiple layers, "subsurface" friction effects were seen. From the phase imaging on the 2nd RF, the buried FLG/NP interface appeared to be partially conformed, producing regions of FLG that are "pinned" and more strained over the NP apices vs suspended between the NP apices. This could be dictating the local extent of dissipated energy, thus influencing the friction force. An alternate cause of the varying F_f over the relatively flat FLG surface could be that the layers are compressed more during the oscillations when between NP apices. To fully understand these effects and more thoroughly investigate the underlying mechanisms, a FLG region on flat SiO_2 should be measured. These studies help provide an initial understanding of how nanoscopic surface

roughness impacts the dynamic motion of graphene and how out-of-plane energy dissipation through multiple layers of graphene is correlated to the frictional response.

CHAPTER V

PERIODIC COVALENT IMMOBILIZATION OF GRAPHENE

5.1 Introduction

Boundary lubrication schemes must meet a variety of demands, including the ability to withstand the high contact pressures and shear forces associated with nanoscopic asperities.[7, 8] The durability[16, 25] of graphene renders it a desirable material to use in such mechanically formidable boundary sliding conditions. A limiting challenge, however, with the performance of graphene as a lubricant has been its extreme sensitivity to its interactions with the top and bottom contacting interfaces.[162] While such substrate-dependent properties pose hurdles to overcome in the broad implementation of graphene as a solid lubricant, they simultaneously open pathways towards using graphene in the design of highly tailored, lubricated interfaces.

As discussed in Chapters I, III, and IV, the chemistry of the sliding interface and the mechanical flexibility of graphene impact the tribological response of graphene as a boundary lubricant.[64, 162] By first understanding how self-assembled monolayers (SAMs) and graphene interact in tribological contacts,[34, 64] the focus can then shift towards using SAMs to design molecularly modified interfaces that manipulate the frictional response of graphene in desired ways. One route is to implement SAMs that are able to chemically bind graphene[172, 173] to the supporting surface to suppress the out-of-plane deformations that typically increase the friction force against the sliding counterface.[39] In a system with graphene covalently immobilized to the substrate, it will also be critical to consider any

secondary effects on the electronic properties.[174-177] The covalent binding of graphene and induced electronic variations can alter the sliding energy landscape of the graphene sheet, further impacting the frictional response.[178-183]

To study the impact of covalently immobilizing graphene on its mechanical and electronic properties, particle lithography was used to fabricate a mixed monolayer of an inert methyl-terminated background and spatially patterned pores of a reactive azide-terminated SAM.[172, 173, 184, 185] This patterned system was designed to take advantage of a built-in reference (the methyl-terminated background) to study changes in the physical properties of graphene after a thermally driven reaction. The surface morphology and frictional response of graphene was examined using atomic force microscopy and friction force microscopy before and after thermally reacting graphene with the surface-linking azide. Moreover, as the electronic properties and plasmonic response of graphene are intimately connected,[134, 137, 138, 141] scattering-type scanning nearfield optical microscopy (s-SNOM) measurements were taken to study the localized effects of periodic covalent immobilization on the propagating surface plasmon.

5.2 Experimental Methods

5.2.1 Preparation of Patterned Graphene/Pores. To prepare a patterned self-assembled monolayer (SAM) surface, particle lithography was used to template an inert background of octadecyltrichlorosilane (OTS, Gelest).[184, 185] This is shown schematically in Figures 5.1a-d, where first a 90 nm SiO_2/Si(100) substrate is prepared via thermal oxidation[64] (Figure 5.1a). A 10 µL suspension of 500 nm diameter silica spheres (4 w/v% in nanopure water, resuspended after centrifuging the as-purchased solution from NIST at

3400 rpm for 5 min, repeated 8 times) was then dropcasted onto the 90 nm SiO_2 substrate under 63 ± 2% relative humidity and allowed to dry for 3 hr, forming a monolayer of hexagonal close packed silica spheres (Figure 5.1b).

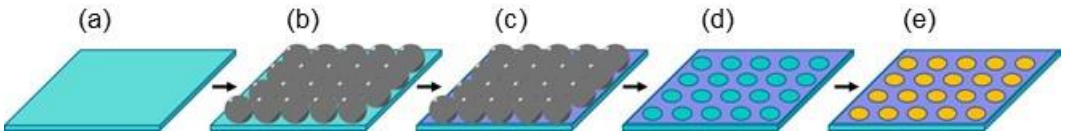

Figure 5. 1. Schematic of the preparation of the patterned mixed SAM substrates: (a) 90 nm SiO_2/Si(100) substrate, (b) silica sphere (500 nm) template, (c) OTS SAM formation around the silica spheres, (d) open OTS pores after silica sphere removal, and (e) backfilled pores with PFPA.

An OTS monolayer was then formed around the silica spheres by immersing the substrate in a 0.5 mM OTS solution (solvent: toluene) for 2 hr (Figure 5.1c). The silica spheres were then removed from the substrate by sonication in a fresh toluene, and two consecutive ethanol washes for 1 hr each. This exposed a hexagonal close packed pattern of open pores (open to the 90 nm SiO_2 substrate) within the OTS template (Figure 5.1d). Further functionalization of the open pores could then be carried out to create a patterned mixed monolayer. Here, the pores were backfilled with N-(3-trimethoxysilylpropyl)-4-azido-2,3,5,6-tetrafluorobenzamide (PFPA, Toronto Research Chemicals, Inc.) by immersing the patterned OTS substrate in a 1 mM PFPA solution (solvent: toluene) for 4 hr (Figure 5.1e). The azide-terminated SAM was chosen for its ability to react with graphene.[172, 173] Graphene was then deposited over both open pore and PFPA filled pore samples via

mechanical exfoliation.[144] To drive the graphene/PFPA reaction, the graphene-PFPA filled pore samples were heated at 140 °C for 40 min.[173]

Physical characterization of the dimensions of the fabricated open and PFPA filled OTS pores was done with contact mode imaging in an Agilent 5500 (Figure 5.2). Single crystal diamond probes (ART D10) were used, with nominal tip radius (R_{tip}) of ~20 nm and nominal spring constant of ~0.1 N/m (determined through blind tip reconstruction and the Sader method,[114] respectively). Measurements were taken in a dry nitrogen environment (relative humidity <0.1%) at a 1 nN applied load. The open OTS pores had a depth of 2.4 ± 0.4 nm and diameter of 116.4 ± 19.3 nm, while the PFPA filled pores had a depth of 1.8 ± 0.2 nm, diameter of 128.8 ± 14.0 nm. The change in pore depth after addition of the PFPA is consistent with the expected length of the molecule of ~1 nm (calculated from bond lengths) while there was no change in diameter outside of one standard deviation.

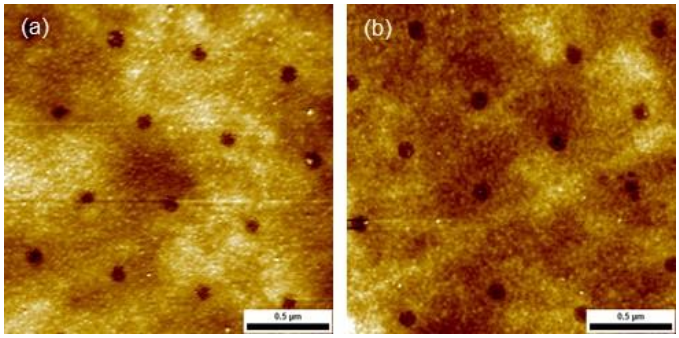

Figure 5. 2. Contact mode AFM topography images (2 x 2 µm at 1 nN applied load) taken with the Agilent 5500 of (a) an open OTS pore template, and (b) an OTS pore template backfilled with PFPA. Courtesy of Maelani Negrito.

5.2.2 Friction Force Microscopy (FFM) of Patterned Graphene/Pores. The impact of covalently pinning graphene on the mechanical properties of graphene was measured with friction force microscopy (FFM). The experimental set-up was the same as described in Section 5.2.1 for the physical characterization of the pore structures. Briefly, FFM measurements were taken on an Agilent 5500 in a dry nitrogen environment using diamond probes (ART D10) and an applied load of 1 nN (R_{tip} ~30 nm and spring constant ~0.1 N/m, determined via the blind tip reconstruction and the Sader method).[114]

5.2.3 Scattering-Type Scanning Nearfield Optical Microscopy (s-SNOM) of Patterned Graphene/Pores. To assess the impact of periodically covalently binding graphene on the surface plasmon polariton (SPP) of the graphene sheet, scattering-type scanning nearfield optical microscopy (s-SNOM) was employed. Data was collected using a nanoIR2-s System from Anasys Instruments in an ambient environment (23 °C and 50% relative humidity) at the Materials Characterization Facility (MCF) at Texas A&M University. Atomic force microscopy (AFM) tapping mode images were simultaneously collected with nearfield (NF) amplitude images (as the absolute value of the NF signal). Platinum-coated silicon AFM tips were used with a nominal tip radius of ~50 nm and resonance frequency of ~270 kHz. A CO_2 laser (λ: 10.5 μm, or 925 cm^{-1}) was used as the farfield source, focused through a numerical aperture of 0.3. Changes in the amplitude of the scattered nearfield signal were imaged at the third harmonic using a double demodulation process to separate the background signal from the scattered NF signal. A liquid nitrogen cooled MCT (HgCdTe) detector was used. Data analysis was done in the programs Analysis Studio v3.12 and Scanning Probe Image Processing (SPIP).

5.3 Results and Discussion

5.3.1 Graphene/Pore Characterization. The fabricated graphene/pore samples are complex composite surfaces that further undergo a heating process to drive a surface-binding chemical reaction. Therefore, it is important to first gain an understanding of the surface morphology and structural characteristics of the samples before studying changes in the mechanical and optoelectronic properties induced in graphene through localized covalent binding. For this purpose, in addition to the physical characterization of the pore templates in Figure 5.2, AFM structural analysis was done for graphene exfoliated over open and filled pores, both before and after heating.

The graphene/open pore and graphene/PFPA pore samples were imaged in tapping mode in the nanoIRs-2 to examine the regions where s-SNOM measurements were taken (Figure 5.3). Figures 5.3a and 5.3b show the graphene/open pore sample before and after heating, respectively, while Figures 5.3c and 5.3d show the graphene/PFPA pore sample before and after heating, respectively. A simplified schematic of a reacted graphene/PFPA pore surrounded by the OTS template (as would be the case for the sample in Figure 5.3d) is shown in Figure 5.3e. In all of the tapping mode images, a peculiar feature is that the pores not covered by graphene, either open or PFPA filled, appear as small protrusions. One possible explanation is that in the ambient tapping mode imaging conditions, a contrast in tip-sample interactions over the hydrophilic pores relative to the hydrophobic OTS matrix causes the exposed pores to appear to have a larger height. Another aspect of the tapping mode images to comment on is that both samples after heating appear "smoother" in morphology. While the same Pt tip was used for all imaging, it is unclear

at this time if the subtle differences in morphological appearance are strictly an effect of the heating or are also an effect of tip changes.

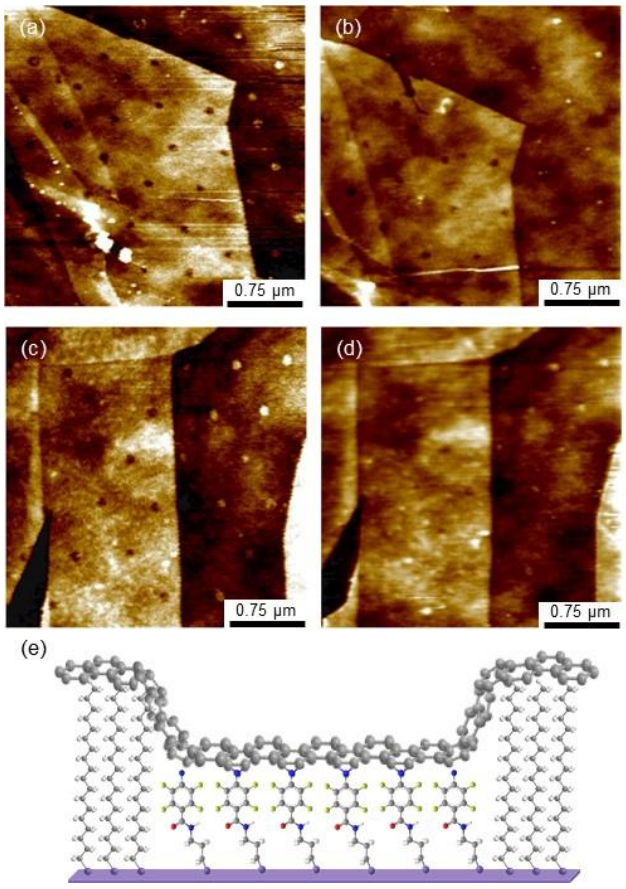

Figure 5. 3. Tapping mode AFM topography images (3 x 3 µm) of the graphene/pore samples taken with the nanoIRs-2. (a) and (b) Show graphene exfoliated over open OTS pores before and after heating, respectively, as a control of the effect of heating on the graphene/OTS pore morphology. (c) and (d) Show graphene exfoliated over PFPA filled pores before and after heating, respectively, to drive the graphene/PFPA reaction. A schematic of graphene covalently bound to a PFPA filled pore is shown in (e).

To supplement the tapping mode imaging that was carried out in the nanoIRs-2, contact mode imaging in the Agilent 5500 was also used to characterize the graphene/open

pore and graphene/PFPA pore samples. Note, however, that the contact mode imaging to measure morphological and F_f changes (Section 5.3.2) for before/after heating were taken on different samples than those presented in Figure 5.3 and used for nearfield measurements (Section 5.3.3). Future work will address taking contact mode measurements (morphology, friction, and adhesion) and nearfield measurements on the same set of graphene/open and graphene/PFPA pore samples. For the work here, it is still useful to assess the morphological changes on these separate samples to examine any physical changes that occur when the graphene/PFPA pores are reacted. Specifically, considering the dimensions of the graphene/PFPA pores before heating, the measured depth was 1.4 ± 0.3 nm and the measured diameter was 109.4 ± 20.9 nm. After heating, the graphene/PFPA pores were slightly shallower and wider, with a depth of 1.2 ± 0.2 nm and diameter of 121.1 ± 22.6 nm. This effect of the graphene/PFPA pores becoming shallower and wider could be because as the graphene is covalently bound to the pores, the surrounding OTS molecules are compressed to accommodate the physical pinning of the graphene sheet. While the images in Figures 5.3c and 5.3d have lower spatial resolution (the Pt tips used in the nano-IRs2 are ~2x's the radius of the D10 tips used in the Agilent 5500), the decreased visibility of the graphene/PFPA pores after heating (as compared to the still visible graphene/OTS pores after heating) supports this possibility.

5.3.2 Impact of Immobilizing Graphene on the Frictional Response. Beyond any potential morphological changes, covalent pinning of graphene to the supporting substrate is expected to also modify its mechanical response in sliding contact.[183, 186] Friction force microscopy (FFM) measurements were therefore carried out to evaluate the extent to

which immobilizing the bottom face of graphene to the substrate impacted the friction force (F_f) measured during sliding against the top face of graphene. Figure 5.4 shows the topography and corresponding F_f images of a graphene/PFPA pore sample before and after heating. Again, note that this sample is not the same graphene/PFPA pore sample used for the nearfield measurements (Figure 5.3 and Section 5.3.3). Future work will resolve this.

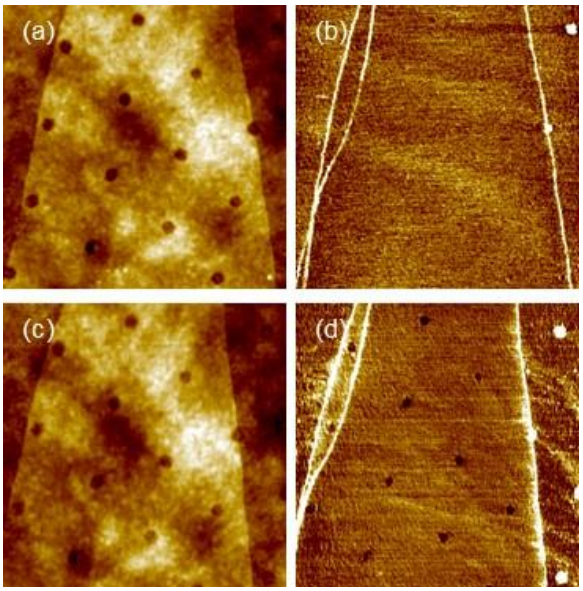

Figure 5. 4. (a) Contact mode AFM topography image and corresponding F_f image (b) of a graphene/PFPA pore sample before heating. (c) Contact mode AFM topography image and corresponding F_f image (d) of the same graphene/PFPA pore region after heating to drive the graphene-PFPA reaction. Courtesy of Maelani Negrito.

Qualitatively comparing the F_f images in Figures 5.4b and 5.4d it is apparent that using heat to drive the graphene-PFPA reaction, thus mechanically pinning graphene, locally lowers the F_f measured over the bound graphene/PFPA pores. To quantify these changes, the friction forces of each measurement (before vs after heating) were normalized

to the tip radius as well as the exposed OTS matrix, under the assumption that the heating process did not alter the OTS SAM. This normalized F_f of the graphene/OTS composite surface was slightly lower than the exposed OTS matrix both before and after heating, at ~0.9. There was no observed F_f change over the graphene/PFPA pore region before heating (noted by their lack of visibility in Figure 5.4b). After thermally driving the reaction, the graphene/PFPA pores had a normalized F_f of ~0.6. This preliminary evidence demonstrates that covalently immobilizing graphene reduces the F_f by a factor of ~1.5.

The assumed mechanism driving this decreased frictional response is that the covalent immobilization suppresses the out-of-plane deformations of graphene. However, while the data here shows that covalently binding graphene lowers the F_f relative to graphene supported on a non-reacted PFPA SAM, it does not address how the bound graphene-PFPA composite surface compares to graphene directly supported by bare silica. It is likely that the immobilization of graphene suppresses the out-of-plane "puckering" of graphene in front of the sliding AFM tip, but it remains uncertain if there are any additional effects of shear deformation from the underlying PFPA film. Future studies will measure the F_f of graphene over open pores (before and after heating) to account for these undetermined effects.

5.3.3 s-SNOM Analysis of Graphene/Pore Composites. The F_f studies discussed in Section 5.3.2 demonstrate how covalently immobilizing graphene to the supporting substrate alters its mechanical properties. Specifically, the covalent pinning is assumed to reduce the F_f of the sliding interface by suppressing the out-of-plane deformations of graphene. This molecular-scale control of friction fits within the context of other studies

demonstrating how covalently functionalizing graphene influences the frictional response. However, in these studies, frictional control was achieved via altering the mechanical properties (flexural stiffness) and physical corrugations of the graphene lattice.[178, 179, 181] It has also been discussed how the covalent functionalization of graphene modulates the geometry and charge redistribution in graphene. These altered electronic properties shift the sliding energy landscape, thus controlling the friction force.[182]

For the covalent functionalization of graphene with PFPA, previous works showed that a level graphene plane is maintained because of the PFPA-graphene binding mechanism. PFPA binds to two adjacent carbon atoms in graphene, preventing physical corrugations (similar to an epoxide binding to graphene).[182, 187] While a level sliding energy landscape is preserved, there are still changes in the electronic structure of graphene with an induced 0.16-0.29 eV bandgap.[175, 176] In the patterned graphene/pore system here, these electronic changes in graphene should be localized to the PFPA pores. As any modifications to graphene's electronic behavior should impact the propagation of its surface plasmons, s-SNOM measurements (as described in Section 5.2.3) were carried out to observe any subsequent local changes in the plasmonic scattering amplitude.

To focus on the impact of locally binding graphene to PFPA, Figure 5.5 shows the post-heating topography and nearfield (NF) images of a graphene/open pore sample as a control and a graphene/PFPA pore sample. In the NF images in Figures 5.5b and 5.5e, several characteristic features for the plasmonic response of graphene can be seen. Most notable is the fringe pattern at the edge of the graphene flakes, caused by the interference of propagating surface plasmon waves (λ_p) reflected at the edges.[137] This fringe pattern is

shown in the cross sections in Figures 5.5c and 5.5f. The periodicity of the fringe pattern[137] is detected as $\lambda_p/2$ and measured here as the lateral distance between the two edge-most peaks. This fringe wavelength measurement is shown schematically in Figure 5.6, along with several additional NF image features.

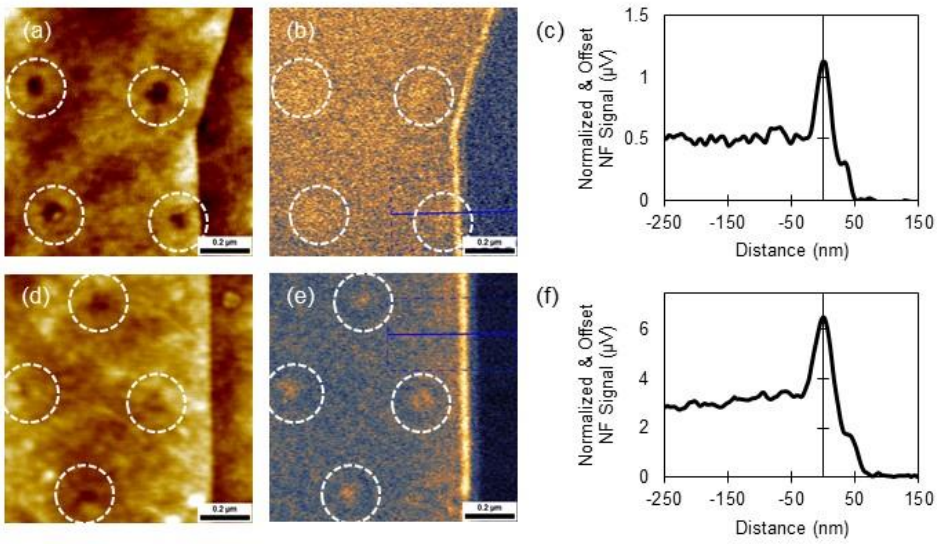

Figure 5. 5. (a) A 1 x 1 μm tapping mode topography image of heated graphene/open pores, collected simultaneously with the nearfield (NF) image in (b). The white dashed circles in (a) and (b) highlight where pores are visible in topography but do not have any observable influence on the NF signal. The blue solid/dashed lines in (b) show the location of a 75-line average cross section, shown in (c), that was used to measure the fringe wavelength and amplitude. (d-f) shows a similar series of a topography image, NF image, and averaged cross section of heated graphene/PFPA pores. Note that in (e) the covalently bound graphene acts as a scattering center, locally increasing the NF signal.

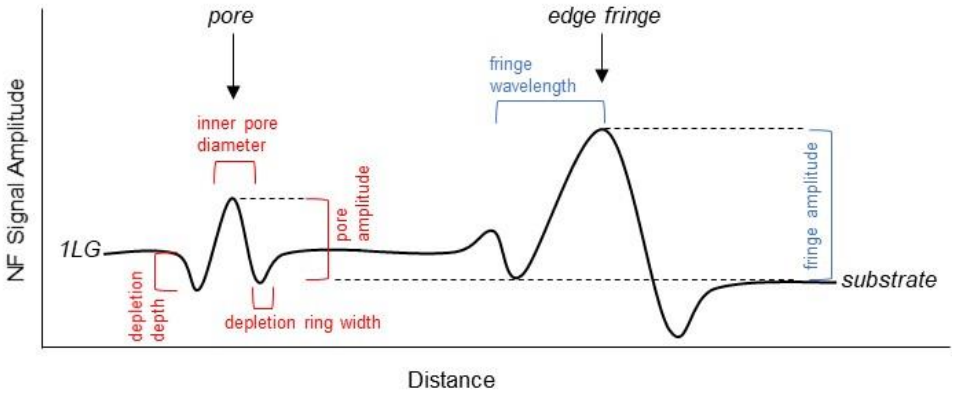

Figure 5. 6. Diagram of the parameters of interest from the graphene NF image features.

Additional features in the NF images in Figures 5.5b and 5.5e (and shown schematically in Figure 5.6) include the fringe amplitude, and several parameters pertaining to the reacted graphene/PFPA pores (discussed later). Both the fringe wavelength and amplitude can be controlled by a gate voltage, or in other words, the degree of carrier density. Fringe wavelength and amplitude were shown to both increase with increasing carrier density.[137] More specifically, the same study noted that the fringe wavelength directly correlates with hole density.[137] For the heated graphene/open pore and graphene/PFPA pore samples here, the measured experimental values of fringe wavelength and amplitude are summarized in Table 5.1. An additional comparison is made to graphene on bare silica (experimentally measured under the same conditions as the graphene/pore samples, images not shown). Note that all images are first normalized to the exposed substrate, then offset so that the normalized signal for the substrate is zero.

Table 5. 1. Summary of the fringe wavelengths and amplitudes for the graphene/pore samples and a graphene/SiO_2 control, measured according to the diagram in Figure 5.6.

Sample	Fringe Wavelength (nm)	Fringe Amplitude (μV)
Heated Open Pores	75	1.0
Heated PFPA Pores	63	6.5
Graphene/SiO_2	75	3.0

The differences in fringe wavelength and amplitude in the plasmonic response of graphene can be interpreted based on the different chemical interactions with the various supporting substrates. For the graphene/open pore sample, the OTS SAM physically separates graphene from the substrate, effectively limiting the doping from the supporting silica[177] and reducing the amplitude relative to the graphene/SiO_2 sample. For the graphene/PFPA pore sample, the increased fringe amplitude (despite still being largely supported on the OTS matrix) could reflect more widespread doping from the PFPA pores beyond the locally bound regions. As evidenced by the increased scattering over the pores in Figure 5.5e, graphene is doped when covalently bound to PFPA (discussed in more detail later).[174-176, 187] Based on the work by Fei *et al*[137] it is expected that the measured fringe wavelength would follow the same trend as the amplitude. However, comparing the values in Table 5.1, the graphene/open pore sample and graphene/SiO_2 sample have the same measured wavelength (~75 nm) and the graphene/PFPA pore sample has a smaller wavelength of ~63 nm.

It should be emphasized that this interpretation of the data is currently only speculative, based on the cited studies. For example, the lateral resolution limit of the data still needs to be established. It could be that differences in fringe wavelength of +/- 15 nm are not significant. A comparison of the fringe amplitudes could also be limited by optimizations in experimental set-up. In general, with s-SNOM measurements it is challenging to draw definitive conclusions without additional insight from modeling, and many of the studies aimed at understanding the plasmonic properties of graphene rely on the integration of experiment and theory.[134, 137, 138, 141, 188-191] Future work will therefore include additional control samples to bolster the experimental results and modeling to supplement the proposed mechanisms governing the behavior of these patterned samples.

Next, focusing on the pores, first note that the graphene/open pores that are visible in the topography image (Figure 5.5a) have no observable changes in the NF scattering (Figure 5.5b). In contrast, the reacted graphene/PFPA pores (Figure 5.5d) have a distinct, localized increase in the NF scattering (Figure 5.5e). To characterize the observed changes in the propagating plasmon, Figure 5.7 labels each graphene/PFPA pore (I-IV) and shows two representative cross sections. In Figures 5.7a and 5.7b, the focus is on a pore (I) that is away from the edge of the graphene flake. Figures 5.7c and 5.7d in turn highlight a pore (III) that is close to the edge. These two pores were chosen for comparison to evaluate if there is any convolution of the localized pore scattering with the edge fringes. Further pore features (outlined in Figure 5.6) are summarized in Table 5.2.

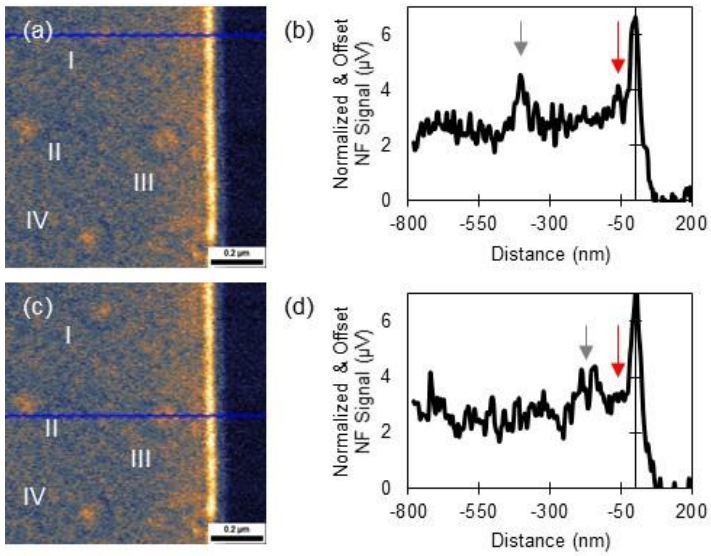

Figure 5. 7. Nearfield (NF) image and cross sections of reacted graphene/PFPA pores. In (a) the four visible, reacted graphene/PFPA pores are labeled I-IV. The solid and dashed blue lines in (a) show the area where the averaged five-line cross section in (b) was taken through pore I. (c) shows the same labeled pores as (a), with a second averaged five-line cross section was taken through pore III, and plotted in (d).

Table 5. 2. Summary of the characteristic reacted graphene/PFPA pore parameters: pore amplitude (Amp.), depletion depth (Dep. Depth), inner pore diameter (Diam.), and depletion ring width (Dep. Ring Width). These parameters were measured according to the diagram in Figure 5.6. The pore labeling (I-IV) is shown in Figure 5.7.

Pore	Amp. (μV)	Dep. Depth (μV)	Diam. (nm)	Dep. Ring Width (nm)
I	4.6	0.6	102.0	46.0
II	4.7	0.7	97.8	38.8
III	4.6	0.7	88.3	48.5
IV	4.5	0.6	73.0	40.0
Average	4.6 ± 0.1	0.7 ± 0.1	90.3 ± 12.9	43.3 ± 4.7

In general, the reacted graphene/PFPA pores have consistent NF scattering characteristics with respect to the local changes in amplitude, diameter, and the surrounding depletion ring. The depletion rings surrounding the pores provide further evidence that the local binding is causing a localized increase in carrier density.[137] If the graphene/PFPA pores are causing charge puddling,[177] it would be expected that in response there would be a decrease in carrier density in the surrounding region. With the pores acting as a scattering center for the propagating plasmon, it is also possible that these effects could interfere with the fringe pattern as the plasmons are reflected at the edge of the flake. The cross sections comparing pores I and III in Figures 5.7b and 5.7d show that the second edge-most fringe is suppressed in the vicinity of pore III as the depletion ring extends towards the edge of the flake. Although, as discussed earlier, without supporting modeling it is difficult to say with certainty what underlying physical properties or mechanisms are causing any of the measured changes in the NF scattering. What is currently apparent is that this set of s-SNOM measurements provides evidence that binding graphene to PFPA in a defined pattern locally alters the electronic properties.

5.4 Conclusions and Future Directions

The work here shows that periodically covalently immobilizing graphene controls both its mechanical properties and electronic properties/plasmonic response. With an OTS matrix as a built-in reference, FFM measurements found that the localized covalent binding of graphene to the supporting substrate lowered the F_f of the sliding interface. This progresses the understanding of the molecular control of friction and how controlling the out-of-plane deformations of graphene can help lead towards interfaces with optimal

tribological performances. Measuring the nearfield scattering amplitude with s-SNOM further revealed that the reacted graphene/PFPA pore platform locally modulated the propagating surface plasmon of graphene. Since the plasmonic response is impacted by the electronic properties of graphene, this data also indicates that the electronic properties of graphene were spatially controlled.

Given the close relationship of tuned mechanical and electronic properties of covalently immobilized graphene, future directions[192] will aim to address how plasmon-phonon coupling can be exploited to use light to control friction. The general scheme will be to use light to launch plasmons in graphene that in turn couple to the substrate phonons. As friction at a sliding interface is dependent on the degree of energy dissipation via mechanical coupling to phonon modes, the coupled plasmon-phonon modes will similarly modulate interfacial friction.[180, 193, 194] Thus this platform serves to not only drive developments in molecularly controlled frictional properties of 2D materials, but also transform technologies by bridging the fields of optics and tribology.

CHAPTER VI

SUMMARY AND OUTLOOK

6.1 Summary

This dissertation has explored the tribological behavior of graphene in a series of controlled and diverse sliding conditions. The impact of tailored adhesion, modulated out-of-plane forces, and localized pinning on the frictional response of graphene was discussed in detail. The framework surrounding these studies was provided in Chapter I, with a review of nanotribological studies of graphene. The literature that is focused on understanding the fundamental nanotribological behavior of graphene has observed a variety of phenomena for supported and suspended graphene, in both humid and dry conditions. The out-of-plane deformation of graphene, its surface bound morphology, and the chemical properties of the confining interface all greatly impact how graphene responds as a solid boundary lubricant. To access deeper levels of understanding of the underlying mechanisms governing the tribological behavior of graphene, additional AFM methods that target specific physical phenomena are required. Chapter II discussed the basic principles of several of these AFM modes, including friction force microscopy, force-distance curves and force-volume mapping, force modulation microscopy, and scattering-type scanning nearfield optical microscopy.

Moving forward from the foundations of Chapters I and II, Chapter III demonstrated that the graphene-tip interaction strength is tailored by using self-assembled monolayers (SAMs) to control the AFM probe chemistry. In turn, this modulated the

frictional behavior of the sliding graphene-SAM interface. The origin of the observed behavior centered around manipulating competing factors of the two-term friction law, where the shear strain was dominated by SAM chain length and the interaction strength was controlled by the specific chemical functionality of the SAM.

As emphasized in Chapter I, a closely related factor influencing the tribological properties of graphene is its out-of-plane deformations. While, for the work in Chapter III, it is difficult to isolate if the controlled tip-graphene interaction strength is additionally modifying the degree of the so-called "puckering," the possibility can not be fully ignored. To investigate the out-of-plane behavior of graphene during lateral sliding in a simpler interface (namely, without SAMs), Chapter IV explored dynamic measurements of graphene on flat and rough surfaces. In dynamic force modulated studies, the frequency dependence of the frictional response of a flat graphene/SiO_2 surface was dominated by the physical behavior of the tip-sample interaction. For few layer graphene (FLG) on a rough surface, regions of the buried FLG interface were "pinned" by the nanoscopic asperities, limiting the extent of out-of-plane interlayer coupling and minimizing energy dissipation. The variations in the degree of freedom for these regions caused localized "subsurface" friction effects that correlated with the amount of dissipated energy, as calculated from the corresponding amplitude and phase response.

To control the out-of-plane fluctuations discussed in Chapters I and IV, the ability of SAMs to tune interfacial interactions (as discussed in Chapter III) can be further used to covalently bind graphene to the supporting surface. Chapter V therefore aimed to understand how periodically immobilizing graphene to the supporting substrate impacted

its frictional response. Preliminary results found that covalently pinning graphene to the supporting surface reduced the friction force of graphene measured on the sliding top face. An additional interesting aspect for future studies of this graphene/SAM platform is that s-SNOM measurements revealed that the periodic binding of graphene also locally impacted its electronic properties. Potential coupling between this altered plasmonic response and substrate phonons should be explored as a means to understand how light can alter friction.

6.2 Outlook

The scope of the work summarized in Section 6.1 pushes forward molecular-scale control of the frictional response of graphene and the level of understanding of how both surface chemistry and nanoscopic substrate roughness impact the dynamic sliding response of graphene. Future work should focus on extending the aims of these studies to broader systems, further expanding the "tool-kit" for 2D material boundary lubrication. For example, the range of surface chemistries explored could be broadened to explore how different non-covalent and covalent interactions control additional effects such as van der Waals screening[47] and what is the subsequent impact on the frictional behavior of graphene. Additionally, future studies could address how functionalization of both the top and bottom contacting surfaces can be used to fine-tune the friction force of graphene through a desired range of responses targeted for specific applications. These platforms of controlled interfaces and AFM studies – surface chemistry, substrate roughness, and force modulation – can also be extended to the extremely diverse family of 2D materials.

In Chapter I, initial friction force studies of MoS_2 found that its tribological behavior was, while largely similar to that of graphene, not identical. For the library of 2D materials, how differences in the atomic structures, chemistries, and mechanical properties dictate their performance in sliding contact remains yet to be fully explored. Ongoing research in the development of 2D materials (MXenes, borophene, 2D exfoliated MOFs, stacked vdW heterostructures, etc.) routinely finds unique properties (catalytic capabilities, electronic and magnetic properties, etc.).[195-198] By further evaluating their tribological behavior, one can envision "multi-functional" lubricants. 2D materials could serve not only as boundary lubricants or mechanically protective surface coatings, but, for example, also as insulators or semi-conductors on an as needed design basis.

Another critical aspect of tribology, especially in the boundary lubrication regime, is mechano-and tribochemistry. Mechano- and tribochemistry describe mechanically driven chemical reactions as a function of applied force/strain, or during sliding. Tribochemistry can either enhance lubrication schemes by driving the formation and growth of antiwear films,[95] or effectively serve as the origin of wear and degradation that ultimately leads to mechanical failure. The systems of 2D materials on chemically reactive surfaces or nanoscopic asperities (as described in Chapters V and IV, respectively) are ideal for further mechano- and tribochemical studies. Understanding strain/force-driven and spatially controlled chemical reactions for a variety of 2D lubricants will improve the capability to design interfaces with optimal tribological performance.

Finally, Chapter V laid the groundwork for developing methods that utilize incident light to control the frictional response. By taking advantage of coupling between

surface plasmons and substrate phonon modes incident radiation could either increase or decrease energy dissipation at a sliding interface, subsequently increasing or decreasing friction with the "switch" of a light.[192] Integrating light-controlled friction responses opens the door for transformative technologies, from the design of haptic devices to answering high impact questions such as "can photons stop a car?" Moreover, designer boundary lubricant schemes such as these are poised to serve a critical role in reducing the energy usage, economic costs, and greenhouse gas emissions associated with friction and wear.

REFERENCES

1. Jost, P.H., *Lubrication (Tribology), Education and Research; A Report on the Present Position and Industry's Needs*. 1966, Great Britain Department of Education and Science: H. M. Stationery Off. 79.
2. Holmberg, K. and Erdemir, A., Influence of Tribology on Global Energy Consumption, Costs and Emissions. *Friction*, **2017**, *5*, 263-284.
3. Carpick, R.W., Jackson, A., Sawyer, W.G., Argibay, N., Lee, P., Pachon, A., and Gresham, R.M., The Tribology Opportunities Study: Can Tribology Save a Quad? *Tribology & Lubrication Technology*, **2016**, *72*, 44-45.
4. Pinkus, O. and Wilcock, D.F., *Strategy for Energy Conservation through Tribology*. 1977, New York: American Society of Mechanical Engineerings.
5. *Energy Flow Charts - Estimated U.S. Energy Consumption in 2015*. Journal, **2015**.
6. Maboudian, R. and Carraro, C., Surface Chemistry and Tribology of MEMS. *Annu. Rev. Phys. Chem.*, **2004**, *55*, 35-54.
7. Ewers, B.W. and Batteas, J.D., Utilizing Atomistic Simulations To Map Pressure Distributions and Contact Areas in Molecular Adlayers within Nanoscale Surface-Asperity Junctions: A Demonstration with Octadecylsilane-Functionalized Silica Interfaces. *Langmuir*, **2014**, *30*, 11897-11905.
8. Kim, S.H., Asay, D.B., and Dugger, M.T., Nanotribology and MEMS. *Nanotoday*, **2007**, *2*, 22-29.

9. Kalin, M., Velkavrh, I., Vižintin, J., and Ožbolt, L., Review of Boundary Lubrication Mechanisms of DLC Coatings Used in Mechanical Applications. *Meccanica*, **2008**, *43*, 623-637.

10. Ewers, B.W. and Batteas, J.D., The Role of Substrate Interactions in the Modification of Surface Forces by Self-Assembled Monolayers. *RSC Adv.*, **2014**, *4*, 16803.

11. Somers, A., Howlett, P., MacFarlane, D., and Forsyth, M., A Review of Ionic Liquid Lubricants. *Lubricants*, **2013**, *1*, 3-21.

12. Wornyoh, E.Y.A., Jasti, V.K., and Fred Higgs, C., A Review of Dry Particulate Lubrication: Powder and Granular Materials. *J. Tribol.*, **2007**, *129*, 438-449.

13. Novoselov, K.S., Graphene: Materials in the Flatland (Nobel Lecture). *Angew. Chem.*, **2011**, *50*, 6986-7002.

14. Zhang, X., Qiao, X.F., Shi, W., Wu, J.B., Jiang, D.S., and Tan, P.H., Phonon and Raman scattering of two-dimensional transition metal dichalcogenides from monolayer, multilayer to bulk material. *Chem Soc Rev*, **2015**, *44*, 2757-85.

15. Lee, C., Wei, X., Kysar, J.W., and Hone, J., Measurement of the Elastic Properties and Intrinsic Strength of Monolayer Graphene. *Science*, **2008**, *321*, 385-388.

16. Berman, D., Deshmukh, S.A., Sankaranarayanan, S.K.R.S., Erdemir, A., and Sumant, A.V., Extraordinary Macroscale Wear Resistance of One Atom Thick Graphene Layer. *Adv. Funct. Mater.*, **2014**, *24*, 6640-6646.

17. Lin, L.-Y., Kim, D.-E., Kim, W.-K., and Jun, S.-C., Friction and Wear Characteristics of Multi-Layer Graphene Films Investigated by Atomic Force Microscopy. *Surface and Coatings Technology*, **2011**, *205*, 4864-4869.

18. Zhu, M.H. and Zhou, Z.R., An Investigation of Molybdenum Disulfide Bonded Solid Lubricant Coatings in Fretting Conditions. *Surface and Coatings Technology*, **2001**, *141*, 240-245.

19. Cho, D.H., Wang, L., Kim, J.S., Lee, G.H., Kim, E.S., Lee, S., Lee, S.Y., Hone, J., and Lee, C., Effect of Surface Morphology on Friction of Graphene on Various Substrates. *Nanoscale*, **2013**, *5*, 3063-3069.

20. Li, H., Contryman, A.W., Qian, X., Ardakani, S.M., Gong, Y., Wang, X., Weisse, J.M., Lee, C.H., Zhao, J., Ajayan, P.M., Li, J., Manoharan, H.C., and Zheng, X., Optoelectronic Crystal of Artificial Atoms in Strain-Textured Molybdenum Disulphide. *Nat. Commun.*, **2015**, *6*, 7381.

21. Li, Q., Liu, X.Z., Kim, S.P., Shenoy, V.B., Sheehan, P.E., Robinson, J.T., and Carpick, R.W., Fluorination of Graphene Enhances Friction Due to Increased Corrugation. *Nano Lett.*, **2014**, *14*, 5212-5217.

22. Fessler, G., Eren, B., Gysin, U., Glatzel, T., and Meyer, E., Friction Force Microscopy Studies on SiO2 Supported Pristine and Hydrogenated Graphene. *Appl. Phys. Lett.*, **2014**, *104*, 041910.

23. Felts, J.R., Oyer, A.J., Hernandez, S.C., Whitener, K.E., Jr., Robinson, J.T., Walton, S.G., and Sheehan, P.E., Direct Mechanochemical Cleavage of Functional Groups from Graphene. *Nat. Commun.*, **2015**, *6*, 6467.

24. Berman, D., Deshmukh, S.A., Sankaranarayanan, S.K.R.S., Erdemir, A., and Sumant, A.V., Macroscale Superlubricity Enabled by Graphene Nanoscroll Formation. *Science*, **2015**, *348*, 1118-1122.

25. Berman, D., Erdemir, A., and Sumant, A.V., Reduced Wear and Friction Enabled by Graphene Layers on Sliding Steel Surfaces in Dry Nitrogen. *Carbon*, **2013**, *59*, 167-175.

26. Ye, Z., Egberts, P., Han, G.H., Johnson, A.T., Carpick, R.W., and Martini, A., Load-Dependent Friction Hysteresis on Graphene. *ACS Nano*, **2016**, *10*, 5161-5168.

27. Egberts, P., Ye, Z., Liu, X.Z., Dong, Y., Martini, A., and Carpick, R.W., Environmental Dependence of Atomic-Scale Friction at Graphite Surface Steps. *Phys. Rev. B*, **2013**, *88*, 035409.

28. Luan, B. and Zhou, R., Wettability and friction of water on a MoS2 nanosheet. *Applied Physics Letters*, **2016**, *108*, 131601.

29. Spear, J.C., Ewers, B.W., and Batteas, J.D., 2D-Nanomaterials for Controlling Friction and Wear at Interfaces. *Nano Today*, **2015**, *10*, 301-314.

30. Berman, D., Erdemir, A., and Sumant, A.V., Graphene: A New Emerging Lubricant. *Materials Today*, **2014**, *17*, 31-42.

31. Guo, W., Yin, J., Qiu, H., Guo, Y., Wu, H., and Xue, M., Friction of Low-Dimensional Nanomaterial Systems. *Friction*, **2014**, *2*, 209-225.

32. Penkov, O., Kim, H.J., Kim, H.J., and Kim, D.E., Tribology of Graphene: A Review. *Int. J. of Precision Eng and Manufacturing*, **2014**, *15*, 577-585.

33. Szlufarska, I., Chandross, M., and Carpick, R.W., Recent Advances in Single-Asperity Nanotribology. *J. Phys. D: Appl. Phys.*, **2008**, *41*, 123001.

34. Spear, J.C., Custer, J.P., and Batteas, J.D., The Influence of Nanoscale Roughness and Substrate Chemistry on the Frictional Properties of Single and Few Layer Graphene. *Nanoscale*, **2015**, *7*, 10021-10029.

35. Park, J.Y. and Salmeron, M., Fundamental Aspects of Energy Dissipation in Friction. *Chem. Rev.*, **2014**, *114*, 677-711.

36. Filleter, T., McChesney, J.L., Bostwick, A., Rotenberg, E., Emtsev, K.V., Seyller, T., Horn, K., and Bennewitz, R., Friction and Dissipation in Epitaxial Graphene Films. *Phys. Rev. Lett.*, **2009**, *102*, 086102.

37. Lee, H., Lee, N., Seo, Y., Eom, J., and Lee, S., Comparison of Frictional Forces on Graphene and Graphite. *Nanotechnology*, **2009**, *20*, 325701.

38. Lee, C., Wei, X., Li, Q., Carpick, R., Kysar, J.W., and Hone, J., Elastic and Frictional Properties of Graphene. *physica status solidi (b)*, **2009**, *246*, 2562-2567.

39. Lee, C., Li, Q., Kalb, W., Liu, X.Z., Berger, H., Carpick, R.W., and Hone, J., Frictional Characteristics of Atomically Thin Sheets. *Science*, **2010**, *328*, 76-80.

40. Choi, J.S., Kim, J.S., Byun, I.S., Lee, D.H., Lee, M.J., Park, B.H., Lee, C., Yoon, D., Cheong, H., Lee, K.H., Son, Y.W., Park, J.Y., and Salmeron, M., Friction Anisotropy-Driven Domain Imaging on Exfoliated Monolayer Graphene. *Science*, **2011**, *333*, 607-610.

41. Gallagher, P., Lee, M., Amet, F., Maksymovych, P., Wang, J., Wang, S., Lu, X., Zhang, G., Watanabe, K., Taniguchi, T., and Goldhaber-Gordon, D., Switchable

Friction Enabled by Nanoscale Self-Assembly on Graphene. *Nat. Commun.*, **2016**, *7*, 10745.

42. Egberts, P., Han, G.H., Liu, X.Z., Johnson, A.T.C., and Carpick, R.W., Frictional Behavior of Atomically Thin Sheets: Hexagonal-Shaped Graphene Islands Grown on Copper by Chemcal Vapor Deposition. *ACS Nano*, **2014**, *8*, 5010-5021.

43. Liu, X.-Z., Li, Q., Egberts, P., and Carpick, R.W., Nanoscale Adhesive Properties of Graphene: The Effect of Sliding History. *Adv. Mater. Interfaces*, **2014**, *1*, 1300053.

44. Deng, Z., Smolyanitsky, A., Li, Q., Feng, X.Q., and Cannara, R.J., Adhesion-Dependent Negative Friction Coefficient on Chemically Modified Graphite at the Nanoscale. *Nat. Mater.*, **2012**, *11*, 1032-1037.

45. Deng, Z., Klimov, N.N., Solares, S.D., Li, T., Xu, H., and Cannara, R.J., Nanoscale Interfacial Friction and Adhesion on Supported versus Suspended Monolayer and Multilayer Graphene. *Langmuir*, **2013**, *29*, 235-243.

46. Paolicelli, G., Tripathi, M., Corradini, V., Candini, A., and Valeri, S., Nanoscale Frictional Behavior of Graphene on SiO(2) and Ni(111) Substrates. *Nanotechnology*, **2015**, *26*, 055703.

47. Tsoi, S., Dev, P., Friedman, A.L., Stine, R., Robinson, J.T., Reinecke, T.L., and Sheehan, P.E., van der Waals Screening by Single-Layer Graphene and Molybdenum Disulfide. *ACS Nano*, **2014**, *8*, 12410-12417.

48. Tripathi, M., Awaja, F., Paolicelli, G., Bartali, R., Iacob, E., Valeri, S., Ryu, S., Signetti, S., Speranza, G., and Pugno, N.M., Tribological Characteristics of Few-

Layer Graphene Over Ni Grain and Interface Boundaries. *Nanoscale*, **2016**, *8*, 6646-6658.

49. Xu, C., Jones, R.L., and Batteas, J.D., Dynamic Variations in Adhesion of Self-Assembled Monolayers on Nanoasperities Probed by Atomic Force Microscopy. *Scanning*, **2008**, *30*, 106-117.

50. Li, T. and Zhang, Z., Snap-Through Instability of Graphene on Substrates. *Nanoscale Res. Lett.*, **2009**, *5*, 169-173.

51. Wagner, T.J.W. and Vella, D., The Sensitivity of Graphene "Snap-Through" to Substrate Geometry. *Appl. Phys. Lett.*, **2012**, *100*, 233111.

52. Scharfenberg, S., Mansukhani, N., Chialvo, C., Weaver, R.L., and Mason, N., Observation of a Snap-Through Instability in Graphene. *Appl. Phys. Lett.*, **2012**, *100*, 021910.

53. Ye, Z., Balkanci, A., Martini, A., and Baykara, M.Z., Effect of Roughness on the Layer-Dependent Friction of Few-Layer Graphene. *Phys. Rev. B*, **2017**, *96*, 115401.

54. Zabel, J., Nair, R.R., Ott, A., Georgiou, T., Geim, A.K., Novoselov, K.S., and Casiraghi, C., Raman Spectroscopy of Graphene and Bilayer Under Biaxial Strain: Bubbles and Balloons. *Nano Lett.*, **2011**, *12*, 617-621.

55. Ding, F., Ji, H., Chen, Y., Herklotz, A., Dorr, K., Mei, Y., Rastelli, A., and Schmidt, O.G., Stretchable Graphene: A Close Look at Fundamental Parameters through Biaxial Straining. *Nano Lett.*, **2010**, *10*, 3453-3458.

56. Ferrari, A.C. and Basko, D.M., Raman Spectroscopy as a Versatile Tool for Studying the Properties of Graphene. *Nat. Nanotechnol.*, **2013**, *8*, 235-246.

57. Ni, Z.H., Yu, T., Lu, Y.H., Wang, Y.Y., Feng, Y.P., and Shen, Z.X., Uniaxial Strain on Graphene: Raman Spectroscopy Study and Band-Gap Opening. *ACS Nano*, **2008**, *2*, 2301-2305.

58. Das, A., Pisana, S., Chakraborty, B., Piscanec, S., Saha, S.K., Waghmare, U.V., Novoselov, K.S., Krishnamurthy, H.R., Geim, A.K., Ferrari, A.C., and Sood, A.K., Monitoring Dopants by Raman Scattering in an Electrochemically Top-Gated Graphene Transistor. *Nat. Nanotechnol.*, **2008**, *3*, 210-215.

59. Onclin, S., Ravoo, B.J., and Reinhoudt, D.N., Engineering Silicon Oxide Surfaces Using Self-Assembled Monolayers. *Angew. Chem.*, **2005**, *44*, 6282-6304.

60. Ewers, B.W. and Batteas, J.D., Molecular Dynamics Simulations of Alkylsilane Monolayers on Silica Nanoasperities: Impact of Surface Curvature on Monolayer Structure and Pathways for Energy Dissipation in Tribological Contacts. *J. Phys. Chem. C*, **2012**, *116*, 25165-25177.

61. Cheng, H. and Hu, Y., Influence of Chain Ordering on Frictional Properties of Self-Assembled Monolayers (SAMs) in Nano-Lubrication. *Adv. Colloid Interface Sci.*, **2012**, *171-172*, 53-65.

62. Jones, R.L., Pearsall, N.C., and Batteas, J.D., Disorder in Alkylsilane Monolayers Assembled on Surfaces with Nanoscopic Curvature. *J. Phys. Chem. C*, **2009**, *113*, 4507-4514.

63. Aswal, D.K., Lenfant, S., Guerin, D., Yakhmi, J.V., and Vuillaume, D., Self Assembled Monolayers on Silicon for Molecular Electronics. *Anal. Chim. Acta*, **2006**, *568*, 84-108.

64. Elinski, M.B., Menard, B.D., Liu, Z., and Batteas, J.D., Adhesion and Friction at Graphene/Self-Assembled Monolayer Interfaces Investigated by Atomic Force Microscopy. *J. Phys. Chem. C*, **2017**, *121*, 5635-5641.

65. Castro Neto, A.H., Guinea, F., Peres, N.M.R., Novoselov, K.S., and Geim, A.K., The Electronic Properties of Graphene. *Rev. Mod. Phys.*, **2009**, *81*, 109-162.

66. Mak, K.F., Lee, C., Hone, J., Shan, J., and Heinz, T.F., Atomically Thin MoS(2): A New Direct-Gap Semiconductor. *Phys. Rev. Lett.*, **2010**, *105*, 136805.

67. Conley, H.J., Wang, B., Ziegler, J.I., Haglund, R.F., Jr., Pantelides, S.T., and Bolotin, K.I., Bandgap Engineering of Strained Monolayer and Bilayer MoS2. *Nano Lett.*, **2013**, *13*, 3626-3630.

68. Huang, H.D., Tu, J.P., Zou, T.Z., Zhang, L.L., and He, D.N., Friction and Wear Properties of IF–MoS2 as Additive in Paraffin Oil. *Tribol. Lett.*, **2005**, *20*, 247-250.

69. Castellanos-Gomez, A., Poot, M., Steele, G.A., van der Zant, H.S., Agrait, N., and Rubio-Bollinger, G., Elastic Properties of Freely Suspended MoS2 Nanosheets. *Adv. Mater.*, **2012**, *24*, 772-775.

70. Jiang, J.W., Qi, Z., Park, H.S., and Rabczuk, T., Elastic Bending Modulus of Single-Layer Molybdenum Disulfide (MoS2): Finite Thickness Effect. *Nanotechnology*, **2013**, *24*, 435705.

71. Peng, Q. and De, S., Outstanding Mechanical Properties of Monolayer MoS2 and its Application in Elastic Energy Storage. *Phys. Chem. Chem. Phys.*, **2013**, *15*, 19427-19437.

72. Lu, Q., Arroyo, M., and Huang, R., Elastic Bending Modulus of Monolayer Graphene. *J. Phys. D: Appl. Phys.*, **2009**, *42*, 102002.

73. Jiang, J.-W., Graphene versus MoS2: A Short Review. *Frontiers of Physics*, **2015**, *10*, 287-302.

74. Kadantsev, E.S. and Hawrylak, P., Electronic Structure of a Single MoS2 Monolayer. *Solid State Communications*, **2012**, *152*, 909-913.

75. Lee, J.U., Yoon, D., and Cheong, H., Estimation of Young's Modulus of Graphene by Raman Spectroscopy. *Nano Lett.*, **2012**, *12*, 4444-4448.

76. Beams, R., Cancado, L.G., Jorio, A., Vamivakas, A.N., and Novotny, L., Tip-Enhanced Raman Mapping of Local Strain in Graphene. *Nanotechnology*, **2015**, *26*, 175702.

77. Elibol, K., Bayer, B.C., Hummel, S., Kotakoski, J., Argentero, G., and Meyer, J.C., Visualising the Strain Distribution in Suspended Two-Dimensional Materials Under Local Deformation. *Sci. Rep.*, **2016**, *6*, 28485.

78. Wu, Q., Wu, Y., Hao, Y., Geng, J., Charlton, M., Chen, S., Ren, Y., Ji, H., Li, H., Boukhvalov, D.W., Piner, R.D., Bielawski, C.W., and Ruoff, R.S., Selective Surface Functionalization at Regions of High Local Curvature in Graphene. *Chem. Commun.*, **2013**, *49*, 677-679.

79. Zhu, L., Zhang, T., Sun, Z., Li, J., Chen, G., and Yang, S.A., Thermal Conductivity of Biaxial-Strained MoS2: Sensitive Strain Dependence and Size Dependent Reduction Rate. *Nanotechnology*, **2015**, *26*, 465707.

80. Li, H., Tsai, C., Koh, A.L., Cai, L., Contryman, A.W., Fragapane, A.H., Zhao, J., Han, H.S., Manoharan, H.C., Abild-Pedersen, F., Norskov, J.K., and Zheng, X., Activating and Optimizing MoS2 Basal Planes for Hydrogen Evolution through the Formation of Strained Sulphur Vacancies. *Nat. Mater.*, **2016**, *15*, 48-53.

81. He, K., Poole, C., Mak, K.F., and Shan, J., Experimental Demonstration of Continuous Electronic Structure Tuning via Strain in Atomically Thin MoS2. *Nano Lett.*, **2013**, *13*, 2931-2936.

82. Hartmann, U., *An Elementary Introduction to Atomic Force Microsocpy and Related Methods*. Vol. D-66041. 1997, Institute of Experimental Physics, University of Saarbrucken: Saarbrucken, Germany.

83. Eaton, P. and West, P., *Atomic Force Microscopy*. 2010, Oxford University Press, New York: Oxford University Press Inc. 247.

84. Agilent, 5500 SPM User's Guide. *Agilent Technologies, Inc.*, **2008**, *N9410-90001, Rev. B*, 1-232.

85. Avouris, P., Bhushan, B., Bimberg, D., von Klitzing, K., Sakaki, H., and Wiesendanger, R., *Scanning Probe Microscopy in Nanoscience and Nanotechnology 2*, ed. B. Bhushan. 2011, London, New York: Springer. 816.

86. Bhushan, B., *Nanotribology and Nanomechanics, An Introduction*. 2 ed, ed. B. Bhushan. 2008, Heidelberg, Germany: Springer. 1516.

87. Carpick, R.W. and Salmeron, M., Scratching the Surface: Fundamental Investigations of Tribology with Atomic Force Microscopy. *Chem. Rev.*, **1997**, *97*, 1163-1194.

88. Drelich, J. and Mittal, K.L., *Atomic Force Microscopy in Adhesion Studies*. 2005, Leiden, The Netherlands: Koninklijke Brill NV.

89. Butt, H.J.C., B. and Kappl, M., Force Measurements with the Atomic Force Microscope: Technique, Interpretation, and Applications. *Surface Science Reports*, **2005**, *59*, 1-152.

90. Jourdan, J.S., Cruchon-Dupeyrat, S.J., Huan, Y., Kuo, P.K., and Liu, G.Y., Imaging Nanoscopic Elasticity of Thin Film Materials by Atomic Force Microsocpy: Effects of Force Modulation Frequency and Amplitude. *Langmuir*, **1999**, *15*, 6495-6504.

91. Rasmussen, A. and Deckert, V., New Dimension in Nano-Imaging: Breaking Through the Diffraction Limit with Scanning Near-Field Optical Microscopy. *Anal. Bioanal. Chem.*, **2005**, *381*, 165-172.

92. Keilmann, F., Scattering-Type Near-Field Optical Microscopy. *Journal of Electron Microscopy*, **2004**, *53*, 187-192.

93. Brogly, M., Fahs, A., and Bistac, S., in *Scanning Probe Microscopy in Nanoscience and Nanotechnology 2*, B. Bhushan, Editor. 2011, Springer: Columbus, OH.

94. Kim, H.J., Yoo, S.S., and Kim, D.e., Nano-Scale Wear: A Review. *Int. J. of Precision Eng and Manufacturing*, **2012**, *13*, 1709-1718.

95. Gosvami, N.N., Bares, J.A., Mangolini, F., Konicek, A.R., Yablon, D.G., and Carpick, R.W., Mechanisms of Antiwear Tribofilm Growth Revealed in situ by Single-Asperity Sliding Contacts. *Science*, **2015**, *348*, 102-106.

96. Wang, H. and Gee, M.L., AFM Lateral Force Calibration for an Integrated Probe Using a Calibration Grating. *Ultramicroscopy*, **2014**, *136*, 193-200.

97. Ogletree, D.F., Carpick, R.W., and Salmeron, M., Calibration of Frictional Forces in Atomic Force Microscopy. *Rev. Sci. Instrum.*, **1996**, *67*, 3298-3306.

98. Feiler, A., Attard, P., and Larson, I., Calibration of the Torsional Spring Constant and the Lateral Photodiode Response of Frictional Force Microscopes. *Rev. Sci. Instrum.*, **2000**, *71*, 2746-2750.

99. Liu, E., Blanpain, B., and Celis, J.P., Calibration Procedures for Frictional Measurements with a Lateral Force Microscope. *Wear*, **1996**, *192*, 141-150.

100. Asay, D.B., Hsiao, E., and Kim, S.H., Corrected Direct Force Balance Method for Atomic Force Microscopy Lateral Force Calibration. *Rev. Sci. Instrum.*, **2009**, *80*, 066101.

101. Liu, W., Bonin, K., and Guthold, M., Easy and Direct Method for Calibrating Atomic Force Microscopy Lateral Force Measurements. *Rev. Sci. Instrum.*, **2007**, *78*, 063707.

102. Choi, D., Hwang, W., and Yoon, E., Improved Lateral Force Calibration Based on the Angle Conversion Factor in Atomic Force Microscopy. *J. Microsc.*, **2007**, *228*, 190-199.

103. Varenberg, M., Etsion, I., and Halperin, G., An Improved Wedge Calibration Method for Lateral Force in Atomic Force Microscopy. *Rev. Sci. Instrum.*, **2003**, *74*, 3362-3367.

104. Cannara, R.J., Eglin, M., and Carpick, R.W., Lateral Force Calibration in Atomic Force Microscopy: A New Lateral Force Calibration Method and General Guidelines for Optimization. *Rev. Sci. Instrum.*, **2006**, *77*, 053701.

105. Wagner, K., Cheng, P., and Vezenov, D., Noncontact Method for Calibration of Lateral Forces in Scanning Force Microscopy. *Langmuir*, **2011**, *27*, 4635-44.

106. Mullin, N. and Hobbs, J.K., A Non-Contact, Thermal Noise Based Method for the Calibration of Lateral Deflection Sensitivity in Atomic Force Microscopy. *Rev. Sci. Instrum.*, **2014**, *85*, 113703.

107. Green, C.P., Lioe, H., Cleveland, J.P., Proksch, R., Mulvaney, P., and Sader, J.E., Normal and Torsional Spring Constants of Atomic Force Microscope Cantilevers. *Rev. Sci. Instrum.*, **2004**, *75*, 1988-1996.

108. Sul, O. and Yang, E.-H., Step-Edge Calibration of Torsional Sensitivity for Lateral Force Microscopy. *Meas. Sci. Technol.*, **2009**, *20*, 115104.

109. Palacio, M.L.B. and Bhushan, B., Normal and Lateral Force Calibration Techniques for AFM Cantilevers. *Crit. Rev. Solid State Mater. Sci.*, **2010**, *35*, 73-104.

110. Munz, M., Force Calibration in Lateral Force Microscopy: A Review of the Experimental Methods. *J. Phys. D: Appl. Phys.*, **2010**, *43*, 063001.

111. Schwarz, U.D., Köster, P., and Wiesendanger, R., Quantitative Analysis of Lateral Force Microscopy Experiments. *Rev. Sci. Instrum.*, **1996**, *67*, 2560-2567.

112. Cain, R.G., Reitsma, M.G., Biggs, S., and Page, N.W., Quantitative Comparison of Three Calibration Techniques for the Lateral Force Microscope. *Rev. Sci. Instrum.*, **2001**, *72*, 3304-3312.

113. Barkley, S.S., Deng, Z., Gates, R.S., Reitsma, M.G., and Cannara, R.J., Quantitative Comparison of Two Independent Lateral Force Calibration Techniques for the Atomic Force Microscope. *Rev. Sci. Instrum.*, **2012**, *83*, 023707.

114. Sader, J.E., Chon, J.W.M., and Mulvaney, P., Calibration of Rectangular Atomic Force Microscope Cantilevers. *Rev. Sci. Instrum.*, **1999**, *70*, 3967-3969.

115. Batteas, J.D. and Stark, R.E., *Surface and Interfacial Studies of Plant Biopolymers by SPM and NMR*, in *Molecular Interfacial Phenomena of Polymers and Biopolymers*, P. Chen, Editor. 2005, Woodhead Publishing Ltd.: Cambridge, U.K. p. 580-608.

116. Grierson, D.S., Flater, E.E., and Carpick, R.W., Accounting for the JKR-DMT Transition in Adhesion and Friction Measurements with Atomic Force Microscopy. *J. Adhesion Sci. Technol.*, **2005**, *19*, 291-311.

117. Johnson, K.L., *Contact Mechanics*. 1987, Cambridge: Cambridge University Press.

118. Derjaguin, B.V., Muller, V.M., and Toporov, Y.P., Effect of Contact Deformations on the Adhesion of Particles. *J. Colloid Interface Sci.*, **1975**, *53*, 314-326.

119. Johnson, K.L., Kendall, K., and Roberts, A.D., Surface Energy and the Contact of Elastic Solids. *Proc. R. Soc. Lond. A.*, **1971**, *324*, 301-313.

120. Carpick, R.W., Ogletree, D.F., and Salmeron, M., A General Equation for Fitting Contact Area and Friction vs Load Measurements. *J. Colloid Interface Sci.*, **1999**, *211*, 395-400.

121. Stan, G., Nanoscale Mechanical Property Measurements in AFM Modes with Direct Force Control: Part II - Force Control in Contact-Resonance Atomic Force Microscopy. *Bruker Nano Surfaces Division*, **2014**, *Webinar Slides*.

122. Asylum, Contact Resonance Viscoelastic Mapping Mode. *Asylum Research, Oxford Instruments*, **2013**, *Data Sheet 43*.

123. Killgore, J.P. and Hurley, D.C., Low-Force AFM Nanomechanics with Higher-Eigenmode Contact Resonance Spectroscopy. *Nanotechnology*, **2012**, *23*, 055702.

124. Tu, Q., Kim, H.S., Oweida, T.J., Parlak, Z., Yingling, Y.G., and Zauscher, S., Interfacial Mechanical Properties of Graphene on Self-Assembled Monolayers: Experiments and Simulations. *ACS Appl. Mater. Interfaces.*, **2017**, *9*, 10203-10213.

125. Tu, Q., Lange, B., Parlak, Z., Lopes, J.M.J., Blum, V., and Zauscher, S., Quantitative Subsurface Atomic Structure Fingerprint for 2D Materials and Heterostructures by First-Principles-Calibrated Contact-Resonance Atomic Force Microscopy. *ACS Nano*, **2016**, *10*, 6491-6500.

126. Killgore, J.P., Yablon, D.G., Tsou, A.H., Gannepalli, A., Yuya, P.A., Turner, J.A., Proksch, R., and Hurley, D.C., Viscoelastic Property Mapping with Contact Resonance Force Microscopy. *Langmuir*, **2011**, *27*, 13983-13987.

127. Kolosov, O.V., Kay, N.D., Robinson, B.J., Rosamond, M., Zeze, D.A., Falko, V., and F., D., Mapping Nanomechanical Phenomena in Graphene Nanostructures Using Force Modulation and Ultrasonic Force Microscopy. *NSTI-Nanotech*, **2012**, *1*, 282-285.

128. Yablon, D.G., Gannepalli, A., Proksch, R., Killgore, J., Hurley, D.C., Grabowski, J., and Tsou, A.H., Quantitative Viscoelastic Mapping of Polyolefin Blends with Contact Resonance Atomic Force Microscopy. *Macromolecules*, **2012**, *45*, 4363-4370.

129. Cleveland, J.P., Anczykowski, B., Schmid, A.E., and Elings, V.B., Energy Dissipation in Tapping-Mode Atomic Force Microscopy. *Appl. Phys. Lett.*, **1998**, *72*, 2613-2615.

130. Martinez, N.F. and Garcia, R., Measuring Phase Shifts and Energy Dissipation with Amplitude Modulation Atomic Force Microscopy. *Nanotechnology*, **2006**, *17*, S167-S172.

131. Tamayo, J. and Garcia, R., Relationship Between Phase Shift and Energy Dissipation in Tapping-Mode Scanning Force Microscopy. *Appl. Phys. Lett.*, **1998**, *73*, 2926-2928.

132. Paulo, A.S. and Garcia, R., Tip-Surface Forces, Amplitude, and Energy Dissipation in Amplitude-Modulation (Tapping Mode) Force Microscopy. *Phys. Rev. B*, **2001**, *64*, 193411.

133. Dazzi, A. and Prater, C.B., AFM-IR: Technology and Applications in Nanoscale Infrared Spectroscopy and Chemical Imaging. *Chem. Rev.*, **2017**, *117*, 5146-5173.

134. Jablan, M., Soljacic, M., and Buljan, H., Plasmons in Graphene: Fundamental Properties and Potential Applications. *Proc. of the IEEE,* **2013**, *101*, 1689-1704.

135. Anasys, nanoIR2-s System User's Manual. *Anasys Instruments Inc.*, **2016**, *00-0026-03*, 1-52.

136. Anasys, nanoIR2-s Technical Brochure - The Only Nanoscale IR Spectroscopy and Imaging Platform with Both AFM-IR and s-SNOM. *Anasys Instruments Inc.*, **2016**.

137. Fei, Z., Rodin, A.S., Andreev, G.O., Bao, W., McLeod, A.S., Wagner, M., Zhang, L.M., Zhao, Z., Thiemens, M., Dominguez, G., Fogler, M.M., Neto, A.H.C., Lau, C.N., Keilmann, F., and Basov, D.N., Gate-Tuning of Graphene Plasmons Reveased by Infrared Nano-Imaging. *Nature*, **2012**, *487*, 82-85.

138. Chen, J., Badioli, M., Alonso-Gonzalez, P., Thongrattanasiri, S., Hutch, F., Osmond, J., Spasenovic, M., Centeno, A., Pesquera, A., Godignon, P., Elorza, A.Z., Camara, N., de Abajo, F.J.G., Hillenbrand, R., and Koppens, F.H.L., Optical Nano-Imaging of Gate-Tunable Graphene Plasmons. *Nature*, **2012**, *487*, 77-81.

139. Maghelli, N., Labardi, M., Patane, S., Irrera, F., and Allegrini, M., Optical Near-Field Harmonic Demodulation in Apertuless Microscopy. *J. Microsc.*, **2001**, *202*, 84-93.

140. Lumen. *Energy in Electromagnetic Waves*. 2018 cited 2018 4/20/2018; Available from: courses.lumenlearning.com/physics/chapter/24-4-energy-in-electromagnetic-waves.

141. de Abajo, F.J.G., Graphene Plasmonics: Challenges and Opportunities. *ACS Photonics*, **2014**, *1*, 135-152.

142. Tsukruk, V.V. and Bliznyuk, V.N., Adhesive and Friction Forces between Chemically Modified Silicon and Silicon Nitride Surfaces. *Langmuir*, **1998**, *14*, 446-455.

143. Gao, J., Luedtke, W.D., Gourdon, D., Ruths, M., Israelachvili, J.N., and Landman, U., Frictional Forces and Amontons' Law: From the Molecular to the Macroscopic Scale. *J. Phys. Chem. B*, **2004**, *108*, 3410-3425.

144. Novoselov, K.S., Geim, A.K., Morozov, S.V., Jiang, D., Zhang, Y., Dubonos, S.V., Grigorieva, I.V., and Firsov, A.A., Electric Field Effect in Atomically Thin Carbon Films. *Science*, **2004**, *306*, 666-6669.

145. Majewski, P.J., Fuchs, T.M., and Prakash, S., Synthesis and Properties of Silane-Based Self-Assembled-Monolayers onto Silica Particles. *Mater. Forum*, **2005**, *29*, 489-493.

146. Patrone, L., Gadenne, V., and Desbief, S., Single and Binary Self-Assembled Monolayers of Phenyl- and Pentafluorophenyl-Based Silane Species, and Their

Phase Separation with Octadecyltrichlorosilane. *Langmuir*, **2010**, *26*, 17111-17118.

147. Batteas, J.D., Quan, X., and Weldon, M.K., Adhesion and Wear of Colloidal Silica Probed by Force Microscopy. *Tribol. Lett.*, **1999**, *7*, 121-128.

148. Kim, J., Seidler, P., Wan, L.S., and Fill, C., Formation, Structure, and Reactivity of Amino-Terminated Organic Films on Silicon Substrates. *J. Colloid Interface Sci.*, **2009**, *329*, 114-119.

149. Howarter, J.A. and Youngblood, J.P., Optimization of Silica Silanization by 3-Aminopropyltriethoxysilane. *Langmuir*, **2006**, *22*, 11142-11147.

150. Israelachvili, J.N., in *Intermolecular and Surface Forces (Third Edition)*. 2011, Academic Press: San Diego. p. 71-132.

151. Munz, M., Giusca, C.E., Myers-Ward, R.L., Gaskill, D.K., and Kazakova, O., Thickness-Dependent Hydrophobicity of Epitaxial Graphene. *ACS Nano*, **2015**, *9*, 8401-8411.

152. Bunch, J.S. and Dunn, M.L., Adhesion Mechanics of Graphene Membranes. *Solid State Commun.*, **2012**, *152*, 1359-1364.

153. Paek, E. and Hwang, G.S., A Computational Analysis of Graphene Adhesion on Amorphous Silica. *J. Appl. Phys.*, **2013**, *113*, 164901.

154. Gao, W., Xiao, P., Henkelman, G., Liechti, K.M., and Huang, R., Interfacial Adhesion between Graphene and Silicon Dioxide by Density Functional Theory with van der Waals Corrections. *J. Phys. D: Appl. Phys.*, **2014**, *47*, 255301.

155. Li, P., You, Z., and Cui, T., Adhesion Energy of Few Layer Graphene Characterized by Atomic Force Microscope. *Sens. Actuators, A*, **2014**, *217*, 56-61.

156. Zacharia, R., Ulbricht, H., and Hertel, T., Interlayer Cohesive Energy of Graphite from Thermal Desorption of Polyaromatic Hydrocarbons. *Phys. Rev. B*, **2004**, *69*, 155406.

157. Munusamy, E. and Wheeler, S.E., Endohedral and Exohedral Complexes of Substituted Benzenes with Carbon Nanotubes and Graphene. *J. Chem. Phys.*, **2013**, *139*, 094703.

158. Hsu, S.M. and Ying, Z.C., in *Nanotribology: Critical Assessment and Research Needs*. 2003, Springer US: Boston, MA.

159. Flater, E.E., Ashurst, W.R., and Carpick, R.W., Nanotribology of Octadecyltrichlorosilane Monolayers and Silicon: Self-Mated versus Unmated Interfces and Local Packing Density Effects. *Langmuir*, **2007**, *23*, 9242-9252.

160. De Wijn, A.S., Flexible Graphene Strengthens Friction. *Nature*, **2016**, *539*, 502-503.

161. Li, S., Li, Q., Carpick, R.W., Gumbsch, P., Liu, X.Z., Ding, X., Sun, J., and Li, J., The Evolving Quality of Frictional Contact with Graphene. *Nature*, **2016**, *539*, 541-546.

162. Elinski, M.B., Liu, Z., Spear, J.C., and Batteas, J.D., 2D or not 2D? The Impact of Nanoscale Roughness and Substrate Interactions on the Tribological Properties of Graphene and MoS2. *J. Phys. D: Appl. Phys.*, **2017**, *50*, 103003.

163. Gao, Y., Kim, S., Zhou, S., Chiu, H.C., Nelias, D., Berger, C., de Heer, W., Polloni, L., Sordan, R., Bongiorno, A., and Riedo, E., Elastic Coupling Between Layers in Two-Dimensional Materials. *Nat. Mater.*, **2015**, *14*, 714-721.

164. Lee, H., Ko, J.H., Song, H.C., Salmeron, M., Kim, Y.H., and Park, J.Y., Isotope- and Thickness-Dependent Friction of Water Layers Intercalated Between Graphene and Mica. *Tribol. Lett.*, **2018**, *66*, 36.

165. Dinelli, F., Biswas, S.K., Briggs, G.A.D., and Kolosov, O.V., Ultrasound Induced Lubricity in Microscopic Contact. *Appl. Phys. Lett.*, **1997**, *71*, 1177-1179.

166. Zhang, Y., Heiranian, M., Janicek, B., Budrikis, Z., Zapperi, S., Huang, P.Y., Johnson, H.T., Aluru, N.R., Lyding, J.W., and Mason, N., Strain Modulation of Graphene by Nanoscale Substrate Curvatures: A Molecular View. *Nano Lett.*, **2018**, *18*, 2098-2104.

167. Vasic, B., Matkovic, A., and Gajic, R., Phase Imaging and Nanosclae Energy Dissipation of Supported Graphene Using Amplitude Modulation Atomic Force Microscopy. *Nanotechnology*, **2017**, *28*, 465708.

168. Yamanaka, K., Ogiso, H., and Kolosov, O.V., Ultrasonic Force Microscopy for Nanometer Resolution Subsurface Imaging. *Appl. Phys. Lett.*, **1994**, *64*, 178-180.

169. Dinelli, F., Pingue, P., Kay, N.D., and Kolosov, O.V., Subsurface Imaging of Two-Dimensional Materials at the Nanoscale. *Nanotechnology*, **2017**, *28*, 085706.

170. Ni, Z.H., Wang, H.M., Kasim, J., Fan, H.M., Yu, T., Wu, Y.H., Feng, Y.P., and Shen, Z.X., Graphene Thickness Determination Using Reflection and Contrast Spectroscopy. *Nano Lett.*, **2007**, *7*, 2758-2763.

171. Ozer, H.O., O'Brien, S.J., Norris, A., Sader, J.E., and Pethica, J.B., Dissipation Imaging with Low Amplitude Off-Resonance Atomic Force Microscopy. *Jpn. J. Appl. Phys.*, **2005**, *44*, 5325-5327.

172. Liu, L.H. and Yan, M., Functionalization of Pristine Graphene with Perfluorophenyl Azides. *J. Mater. Chem.*, **2011**, *21*, 3273-3276.

173. Liu, L.H. and Yan, M., Simple Method for the Covalent Immobilization of Graphene. *Nano Lett.*, **2009**, *9*, 3375-3378.

174. Liu, H. and Zhu, D., Chemical Doping of Graphene. *J. Mater. Chem.*, **2011**, *21*, 3335-3345.

175. Plachinda, P., Evans, D., and Solanki, R., Electrical Conductivity of PFPA Functionalized Graphene. *Solid-State Electronics*, **2013**, *79*, 262-267.

176. Suggs, K., Reuven, D., and Wang, X.Q., Electronic Properties of Cycloaddition-Functionalized Graphene. *J. Phys. Chem. C*, **2011**, *115*, 3313-3317.

177. Wang, Q.H., Jin, Z., Kim, K.K., Hilmer, A.J., Paulus, G.L.C., Shih, C.J., Ham, M.H., Sanchez-Yamagishi, J.D., Watanabe, K., Taniguchi, T., Kong, J., Jarillo-Herrero, P., and Strano, M.S., Understanding and Controlling the Substrate Effect on Graphene Electron-Transfer Chemistry via Reactivity Imprint Lithography. *Nature Chemistry*, **2012**, *4*, 724-732.

178. Dong, Y., Wu, X., and Martini, A., Atomic Roughness Enhanced Friction on Hydrogenated Graphene. *Nanotechnology*, **2013**, *24*, 375701.

179. Li, Q., Liu, X.Z., Kim, S.P., Shenoy, V.B., Sheehan, P.E., Robinson, J.T., and carpick, r.W., Fluorination of Graphene Enhances Friciton Due to Increased Corrugation. *Nano Lett.*, **2014**, *14*, 5212-5217.

180. Buldum, A., Leitner, D.M., and Ciraci, S., Model for Phononic Energy Dissipation in Friction. *Phys. Rev. B*, **1999**, *59*, 16042-16046.

181. Ko, J.H., Kwon, S., Byun, I.S., Choi, J.S., Park, B.H., Kim, Y.H., and Park, J.Y., Nanotribological Properties of Fluorinated, Hydrogenated, and Oxidized Graphenes. *Tribol. Lett.*, **2013**, *50*, 137-144.

182. Guo, Y., Qiu, J., and Guo, W., Reduction of Interfacial Friction in Commensurate Graphene/h-BN Heterostructures by Surface Functionalization. *Nanoscale*, **2016**, *8*, 575-580.

183. Ou, J., Wang, J., Liu, S., Mu, B., Ren, J., Wang, H., and Yang, S., Tribology Study of Reduced Graphene Oxide Sheets on Silicon Substrate Synthesized via Covalent Assembly. *Langmuir*, **2010**, *26*, 15830-15836.

184. Bae, C., Shin, H., Moon, J., and Sun, M.M., Contact Area Lithography (CAL): A New Approach to Direct Formation of Nanometric Chemical Patterns. *Chem. Mater.*, **2006**, *18*, 1085-1088.

185. Saner, C.K., Lusker, K.L., LeJeune, Z.M., Serem, W.K., and Garno, J.C., Self-Assembly of Octadecyltrichlorosilane: Surface Structures Formed Using Different Protocols of Particle Lithography. *Beilstein J. Nanotechnol.*, **2012**, *3*, 114-122.

186. Spear, J.C. and Batteas, J.D., Understanding and Controlling the Tribological Properties of Graphene on Rough Surfaces. *Department of Chemistry, Texas A&M University*, **2015**, *Dissertation*.

187. Chua, C.K. and Pumera, M., Covalent Chemistry on Graphene. *Chem. Soc. Rev.*, **2013**, *42*, 3222-3233.

188. Yu, R., Cox, J.D., Saavedra, J.R.M., Javier, F., and de Abajo, F.J.G., Analytical Modeling of Graphene Plasmons. *ACS Photonics*, **2017**, *4*, 3106-3114.

189. Slipchenko, T.M., Nesterov, M.L., Hillenbrand, R., Nikitin, A.Y., and Martin-Moreno, L., Graphene Plasmon Reflection by Corrugations. *ACS Photonics*, **2017**, *4*, 3081-3088.

190. Hu, F., Luan, Y., Fei, Z., Palubski, I.Z., Goldflam, M.D., Dai, S., Wu, J.S., Post, K.W., Janssen, G.C.A.M., Fogler, M.M., and Basov, D.N., Imaging the Localized Plasmon Resonance Modes in Graphene Nanoribbons. *Nano Lett.*, **2017**, *17*, 5423-5428.

191. Gerber, J.A., Berweger, S., O'Callahan, B.T., and Raschke, M.B., Phase-Resolved Surface Plasmon Interferometry of Graphene. *Phys. Rev. Lett.*, **2014**, *113*, 055502.

192. Negrito, M. and Batteas, J.D., Correlation of Electronic Structure to the Frictional and Optical Response of Covalently Immobilized Graphene. *Department of Chemistry, Texas A&M University*, **2018**, *Preliminary Research Proposal*.

193. Gao, W., Shu, J., Qiu, C., and Xu, Q., Excitation of Plasmonic Waves in Graphene by Guided-Mode Resonances. *ACS Nano*, **2012**, *6*, 7806-7813.

194. Barcelos, I.D., Cadore, A.R., Campos, L.C., Malachia, A., Watanabe, K., Taniguchi, T., Maia, F.C., Freitas, R., and Deneke, C., Graphene/h-BN Plasmon-Phonon Coupling and Plasmon Delocalization Observed by Infrared Nano-Spectroscopy. *Nanoscale*, **2015**, *7*, 11620-11625.

195. Novoselov, K.S., Mishchenko, A., Carvalho, A., and Castro Neto, A.H., 2D Materials and van der Waals Heterostructures. *Science*, **2016**, *353*, 9439.

196. Gao, G., O'Mullane, A.P., and Du, A., 2D MXenes: A New Family of Promising Catalysts for the Hydrogen Evolution Reaction. *ACS Catalysis*, **2016**, *7*, 494-500.

197. Ding, Y., Chen, Y.P., Zhang, X., Chen, L., Dong, Z., Jiang, H.L., Xu, H., and Zhou, H.C., Controlled Intercalation and Chemical Exfoliation of Layered Metal-Organic Frameworks Using a Chemically Labile Intercalating Agent. *J. Am. Chem. Soc.*, **2017**, *139*, 9136-9139.

198. Meng, F., Chen, X., Sun, S., and He, J., Electronic and Magnetic Properties of Pristine and Hydrogenated Borophene Nanoribbons. *Physica E: Low-Dimensional Systems and Nanostructures*, **2017**, *91*, 106-112.